

A Galactic Self-Portrait: Density Structure and Integrated Properties of the Milky Way Disk

JULIE IMIG ,^{1,2} JON A. HOLTZMAN ,² GAIL ZASOWSKI ,³ JIANHUI LIAN ,⁴ NICHOLAS F. BOARDMAN ,⁵ ALEXANDER STONE-MARTINEZ ,² J. TED MACKERETH ,⁶ MOIRE K. M. PRESCOTT ,² RACHAEL L. BEATON ,^{1,7,8} TIMOTHY C. BEERS ,⁹ DMITRY BIZYAEV ,^{10,11} MICHAEL R. BLANTON ,¹² KATIA CUNHA ,¹³ JOSÉ G. FERNÁNDEZ-TRINCADO ,¹⁴ CATHERINE E. FIELDER ,^{15,16} STEN HASSELQUIST ,¹ CHRISTIAN R. HAYES ,¹⁷ MISHA HAYWOOD ,¹⁸ HENRIK JÖNSSON ,¹⁹ RICHARD R. LANE ,²⁰ STEVEN R. MAJEWSKI ,²¹ SZabolcs MÉSZÁROS ,^{22,23,24} IVAN MINCHEV ,²⁵ DAVID L. NIDEVER ,²⁶ CHRISTIAN NITSCHELM ,²⁷ AND JENNIFER SOBECK ,²⁸

¹Space Telescope Science Institute, 3700 San Martin Drive, Baltimore, MD 21218, USA

²Department of Astronomy, New Mexico State University, P.O.Box 30001, MSC 4500, Las Cruces, NM, 88003, USA

³Department of Physics and Astronomy, University of Utah, 115 S. 1400 E., Salt Lake City, UT 84112, USA

⁴South-Western Institute for Astronomy Research, Yunnan University, Kunming, Yunnan 650091, People's Republic of China

⁵School of Physics and Astronomy, University of St Andrews, North Haugh, St Andrews KY16 9SS, UK

⁶Department of Astronomy and Astrophysics, University of Toronto, 50 St. George Street, Toronto, ON, M5S 3H4, Canada

⁷Department of Astrophysical Sciences, Princeton University, Princeton, NJ 08544, USA

⁸The Observatories of the Carnegie Institution for Science, 813 Santa Barbara St., Pasadena, CA 91101

⁹Department of Physics and Astronomy and JINA Center for the Evolution of the Elements (JINA-CEE), University of Notre Dame, Notre Dame, IN 46556 USA

¹⁰Apache Point Observatory and New Mexico State University, P.O. Box 59, Sunspot, NM, 88349-0059, USA

¹¹Sternberg Astronomical Institute, Moscow State University, Moscow

¹²Center for Cosmology and Particle Physics, Department of Physics, 726 Broadway, Room 1005, New York University, New York, NY 10003, USA

¹³Steward Observatory, University of Arizona, Tucson, AZ 85721, USA

¹⁴Instituto de Astronomía, Universidad Católica del Norte, Av. Angamos 0610, Antofagasta, Chile

¹⁵Steward Observatory, University of Arizona, Tucson, AZ, 85721, USA

¹⁶Department of Physics and Astronomy, University of Pittsburgh, Pittsburgh, PA 15260, USA

¹⁷NRC Herzberg Astronomy and Astrophysics Research Centre, 5071 West Saanich Road, Victoria, B.C., Canada, V9E 2E7

¹⁸GEPI, Observatoire de Paris, PSL Research University, CNRS, Sorbonne Paris Cité, 5 place Jules Janssen, 92190 Meudon, France

¹⁹Materials Science and Applied Mathematics, Malmö University, SE-205 06 Malmö, Sweden

²⁰Centro de Investigación en Astronomía, Universidad Bernardo O'Higgins, Avenida Viel 1497, Santiago, Chile

²¹Department of Astronomy, University of Virginia, Charlottesville, VA 22904, USA

²²ELTE Eötvös Loránd University, Gothard Astrophysical Observatory, 9700 Szombathely, Szent Imre H. st. 112, Hungary

²³MTA-ELTE Lendület "Momentum" Milky Way Research Group, Hungary

²⁴MTA-ELTE Exoplanet Research Group, Szombathely, Szent Imre h. u. 112., H-9700, Hungary

²⁵Leibniz-Institut für Astrophysik Potsdam (AIP), An der Sternwarte 16, D-14482 Potsdam, Germany

²⁶Department of Physics, Montana State University, P.O. Box 173840, Bozeman, MT 59717, USA

²⁷Centro de Astronomía (CITEVA), Universidad de Antofagasta, Avenida Angamos 601, Antofagasta 1270300, Chile

²⁸Department of Astronomy, University of Washington, Box 351580, Seattle, WA 98195, USA

ABSTRACT

The star formation history and evolution of the Milky Way disk is imprinted in the ages, positions, and chemical compositions of individual stars. In this study, we derive the intrinsic density distribution of different stellar populations using the final data release of the Apache Point Observatory Galactic Evolution Experiment (APOGEE) survey. Positions, chemical abundances, and ages for 203,197 red giant branch stars across the entire disk ($0 \leq R \leq 20$ kpc) are used to sort the stellar disk into sub-populations of metallicity ($\Delta[M/H] = 0.1$ dex), age ($\Delta \log(\text{age}) = 0.1$ dex), and α -element abundances ($[\alpha/M]$). We fit the present-day structural parameters and surface mass density distribution of each

stellar sub-population after correcting for the survey selection function. We find that the low- α disk is characterized by longer scale lengths and shorter scale heights, and is best fit by a broken exponential radial profile for each population, with the break radius decreasing with metallicity. The sharpness of the break decreases with stellar age, suggesting that a time-dependent process like stellar radial migration may contribute to the broadening. The high- α disk is characterized by shorter scale lengths and larger scale heights, and is generally well-approximated by a single exponential radial profile that is more strongly flared vertically than the low- α populations. The low- α populations make up 85% of the disk mass at the solar circle and 65% when integrated across the whole Galaxy. We measure the average mass-weighted scale length to be $R_d = 2.37 \pm 0.2$ kpc when summed over all stellar populations. These results are applied to produce new estimates of the integrated properties of the Milky Way from early times to the present day. The Milky Way’s present-day color of $(g - r) = 0.72 \pm 0.02$ is consistent with the classification of a red spiral galaxy, although it has only been in the “green valley” region of the galaxy color-mass diagram for the last ~ 3 Gyr. The star formation history shows that while there is significant age overlap between the two α sequences, the high- α population formed early ($t \gtrsim 10$ Gyr ago) during a fast starburst, while the low- α disk formed stars more continuously over time.

Keywords: Milky Way Galaxy (1054) — Milky Way Evolution (1052) — Milky Way mass (1058) — galaxy evolution (594) — stellar populations (1622) — Galaxy stellar content (621)

Draft Version May 14, 2025
Submitted to ApJ MM/DD/YYYY

1. INTRODUCTION

The present-day kinematic and chemical structure of the Milky Way’s stellar disk reflects the star formation history and evolution of our Galaxy. For this reason, observational Galactic archaeology remains a cornerstone of galactic astronomy, placing key constraints on models of the formation and evolution of disk galaxies. The advent of large stellar spectroscopic surveys allows for the positions, stellar parameters, chemical compositions, and ages of hundreds of thousands of individual stars to be precisely measured in projects like APOGEE (Majewski et al. 2017), Gaia (Gaia Collaboration et al. 2018, 2021), Gaia-ESO (Gilmore et al. 2022), LAMOST (Luo et al. 2015), GALAH (Buder et al. 2018), and RAVE (Steinmetz et al. 2020). At the same time, large samples of other galaxies have revealed various fundamental relations across the galaxy population as a whole, accessible through spatially-resolved integral field unit (IFU) surveys like MaNGA (Bundy et al. 2015), CALIFA (Sánchez et al. 2016), and SAMI (Croom et al. 2021).

Translating between the realms of Galactic and extragalactic astronomy, however, remains a challenge. While impressive sample sizes of other galaxies can be used to explore broad trends and relations within the galaxy population, we only have the one Milky Way, making it difficult to place within an extragalactic context. Our inside perspective of the Milky Way is both a benefit

and a hindrance; the entire evolutionary history of the Milky Way can be accessed but it can not be directly compared to other galaxies.

One of the largest obstacles for comparing Galactic and extragalactic observations is the selection function of astronomical surveys. Observational limitations severely influence what stars can be observed and where in the Galaxy. Despite the large numbers of stars observed in a survey, the sample is not representative of the entire Milky Way unless these selection biases are first corrected. The selection function, while important, is nontrivial to calculate leading many studies to ignore it entirely. The selection function depends on the targeting strategies and instrumentation specifications unique to each survey, requires some assumptions based on stellar evolution theory, and quantitative understanding of the complex distribution of dust in the Milky Way.

Once the survey selection function is accounted for, the effective sampling of the Milky Way expands from the limited solar vicinity into a representation of the entire Galaxy. These types of analyses are useful for measuring the Milky Way’s structural parameters, including the disk scale length and scale height (e.g., Bovy et al. 2012b; Mackereth et al. 2017; Wang et al. 2018; Yu et al. 2021; Lian et al. 2022), and for estimating the total stellar mass of the different galactic components (e.g., Bovy & Rix 2013; Mackereth & Bovy 2020; Horta et al. 2020).

Density profile decompositions of the Milky Way disk near the Solar neighborhood led to the discovery of two geometric components; the “thin disk” and the “thick disk”, which are characterized by a difference in exponential scale height as the name implies (e.g., Yoshii

1982; Gilmore & Reid 1983; Robin et al. 2003; Jurić et al. 2008). The two disks also differ in their dynamical signatures, with stars belonging to the thin disk generally having faster rotational velocities and less heated vertical orbits than thick disk members (e.g., Soubiran et al. 2003; Jurić et al. 2008; Kordopatis et al. 2013; Robin et al. 2017; Mackereth et al. 2019; Robin et al. 2022). Furthermore, the two disks have different chemical compositions; thin disk stars are generally younger, more metal-rich, and depleted in α -element¹ abundances compared to thick disk members (e.g., Fuhrmann 1998; Bensby et al. 2005; Reddy et al. 2006; Lee et al. 2011; Bovy et al. 2012b, 2016b; Nidever et al. 2014; Hayden et al. 2015; Mackereth et al. 2017; Vincenzo et al. 2021; Katz et al. 2021). The origin of this structural, kinematical, and chemical bimodality in the disk remains unclear, and there is some debate on whether the two disks should be classified as different galactic components at all (e.g., Bensby et al. 2007; Bovy et al. 2012a; Kawata & Chiappini 2016; Hayden et al. 2017; Anders et al. 2018). Nevertheless, due to these differences the two disk components are often considered independently of one another as two distinct components when fitting for the structural parameters of the Milky Way.

The vertical density profile of the Milky Way disk is also exponential. Near the solar neighborhood, the scale height of the thin disk is usually measured around 0.3 - 0.4 kpc, and the thick disk has a larger scale height around 0.75 - 1.3 kpc (e.g., Gilmore & Reid 1983; Bovy et al. 2016b; Mackereth et al. 2017; Lian et al. 2022). This quantity does seem to have a radial dependence, with the scale height of some populations increasing with radius in a flared disk. There is some debate on which populations flare most strongly, with some studies finding the strongest flaring among the low- α thin disk populations (e.g., Bovy et al. 2016b; Mackereth et al. 2017; Robin et al. 2022) and others finding the strongest flaring in the high- α thick disk populations (e.g., Yu et al. 2021; Lian et al. 2022). This discrepancy has different implications for the formation history of the Milky Way, as some models predict that a flared thick disk arises under any realistic disk formation scenario (Minchev et al. 2015), while others suggest that a strongly flared thick disk is often associated with more violent merger histories (García de la Cruz et al. 2020).

Despite these advances in understanding the structural form of the Milky Way's stellar disk(s), these measurements are inherently different quantities than those

observed in other disk galaxies. The Milky Way's structural parameters are measured through star counts, or its mass, while the structural parameters of other galaxies can only be measured through their light profiles (Fathi et al. 2010; Lange et al. 2015). This difference could explain the apparent discrepancies between the Milky Way and some of its peers, such as its scale length being too small for its mass (e.g., Boardman et al. 2020).

In this paper, we explore the physical structure of the Milky Way disk and how its properties compare in integrated light. Section 2 introduces the data used in this analysis from the APOGEE survey. Section 3 summarizes the density structure fitting methodology we use, originally developed in previous literature (e.g., Bovy et al. 2012a; Rix & Bovy 2013; Bovy et al. 2016b; Mackereth et al. 2017). Section 4 presents the best-fit structural parameters of each stellar population from the density fitting. These results are applied in section 5 to estimate some integrated properties of the Milky Way, including (g-r) colors and total star formation history. Section 6 discusses the implications of our results, and we conclude in Section 7.

2. DATA

2.1. APOGEE

The Apache Point Observatory Galactic Evolution Experiment (APOGEE; Majewski et al. 2017) is a high-resolution ($R \sim 22,500$) near-infrared ($1.51 - 1.70 \mu\text{m}$) spectroscopic survey containing observations of 657,135 unique stars released as part of the SDSS-IV survey (Blanton et al. 2017). The spectra were obtained using the APOGEE spectrograph (Wilson et al. 2019) mounted on the 2.5m Sloan Foundation telescope (Gunn et al. 2006) at Apache Point Observatory to observe the Northern Hemisphere (APOGEE-N). The survey was later expanded to include the southern hemisphere (APOGEE-S) using a second APOGEE spectrograph on the 2.5 m Irénée du Pont telescope (Bowen & Vaughan 1973) at Las Campanas Observatory to observe the Southern Hemisphere (APOGEE-S). The targeting strategies for previous data releases of the APOGEE survey are described in Zasowski et al. (2013, 2017), and for the final data release in Beaton et al. (2021) (for APOGEE-N) and Santana et al. (2021) (for APOGEE-S). The final version of the APOGEE catalog was published in December 2021 as part of the 17th data release of the Sloan Digital Sky Survey (DR17; Abdurro'uf et al.

¹ α -elements are elements with an atomic number multiple of 4 (the mass of a Helium nucleus, an α -particle), e.g., O, Mg, S, Ca

2022) and is available publicly online through the SDSS Science Archive Server and Catalog Archive Server².

The APOGEE data reduction pipeline is described in Nidever et al. (2015). Stellar parameters and chemical abundances in APOGEE were derived within the APOGEE Stellar Parameters and Chemical Abundances Pipeline (ASPCAP; Holtzman et al. 2015; García Pérez et al. 2016; Holtzman et al. 2018; Jönsson et al. 2020, J.A. Holtzman et al. in prep.). ASPCAP derives stellar atmospheric parameters, radial velocities, and as many as 20 individual elemental abundances for each APOGEE spectrum by comparing each to a multi-dimensional grid of theoretical model spectra (Mészáros et al. 2012; Zamora et al. 2015) and corresponding line lists (Shetrone et al. 2015; Smith et al. 2021), employing a χ^2 minimization routine with the code FERRE (Alende Prieto et al. 2006) to derive the best-fit parameters for each spectrum. We highlight that several elements were updated in DR17 to include non-LTE effects in the stellar atmosphere (Osorio et al. 2020). ASPCAP reports typical precision in overall metallicity measurements within 0.01 dex (Jönsson et al. 2018). In this study, we adopt the calibrated values for surface gravity ($\log g$), metallicity ([M/H]), and α -element abundances ([α /M]) from ASPCAP.

2.2. Age and distance estimates

In addition to the chemical abundances from ASPCAP, we adopt stellar age and distance estimates from the `distmass` value added catalog (Stone-Martinez et al. 2024).³

The `distmass` distances were derived through a neural network that was trained to estimate a star's luminosity based on its ASPCAP parameters, using Gaia distances and star cluster distances to provide the training labels. Distance estimates from the `distmass` catalog are typically precise within 10%. These distances, along with the right ascension (RA) and declination (DEC) were used to derive Galactocentric positions for each star, with the reference location of the Sun defined to be $R_\odot = 8.3$ kpc with a height of $z_\odot = 0.027$ kpc above the plane (Bland-Hawthorn & Gerhard 2016).

The stellar ages were similarly derived using a second neural network, working under the assumption that for evolved red giant stars, the chemical abundances of carbon and nitrogen provide information on the stel-

lar mass due to the mass-dependence of stellar mixing (e.g., Iben 1965; Salaris & Cassisi 2005; Shetrone et al. 2019). The neural network was trained on the ASPCAP parameters ($\log g$, [M/H], [C/Fe], [N/Fe]) of stars with known asteroseismic masses from the APOGEE-Kepler overlap survey (APOKASC; Pinsonneault et al. 2018, Pinsonneault et al. 2023 in prep.); then it predicts the masses for all giant stars from DR17. Knowing the masses for evolved stars, ages can be derived through stellar evolution theory that predicts a star's location on an isochrone. In the `distmass` catalog, isochrones from Choi et al. (2016) were adopted to make this conversion from derived mass to stellar age. These isochrones cover a range of ages ($5.0 \leq \log_{10}(\text{age [yr]}) \leq 10.3$), metallicities ($-2.0 \leq [Z/H] \leq 0.5$), and masses ($0.1 \leq M/M_\odot \leq 300$). The stellar age estimates in `distmass` report a typical uncertainty of $\pm 0.15 \log_{10}(\text{age [yr]})$.

Stone-Martinez et al. (2024) evaluate the `distmass` ages and their uncertainties by comparing to previous literature and find good agreement. Compared with a sample of stellar cluster members and their independent age estimates from main sequence turnoff fitting, Stone-Martinez et al. (2024) reports that the `distmass` ages are accurate within $\pm 1\sigma = 0.16$ in $\log_{10}(\text{age})$ across 12 different star clusters with ages $9.2 \leq \log_{10}(\text{age}) \leq 9.7$. Compared to a larger sample of field stars from the `astroNN` catalog (Leung & Bovy 2018; Mackereth et al. 2019), the `distmass` ages show a typical spread of $\pm 1\sigma = 0.11$ in $\log_{10}(\text{age})$. Both of these comparisons are consistent within the reported `distmass` age uncertainties.

For the remainder of this paper, we adopt the `distmass` results trained on the uncorrected “SS” ages from APOKASC 3 (Pinsonneault et al. 2023 in prep.), corresponding to the column named “AGE_UNCOR_SS” in the `distmass` catalog. We refer the reader to Stone-Martinez et al. (2024) and Imig et al. (2023) (their Appendix A) for a more detailed discussion on the various caveats associated with this stellar age catalog.

2.3. Sample Refinement

A number of data and quality cuts were applied to the APOGEE data to refine our sample prior to the fitting. First, we restrict the sample to the “main survey targets”, which are stars that were targeted randomly within the selection criteria and removes duplicates, using the EXTRATARG == 0 flag in the APOGEE `allStar` catalog. The motivation for this cut, and more details on the APOGEE targeting strategies, selection function, and how it influences our methodology are discussed further in Section 3.2. In short, this cut is necessary to scale from the stars that APOGEE observed to the true dis-

² Data Access Instructions: https://www.sdss.org/dr17/irspec/specro_data/

³ `distmass` VAC: https://www.sdss4.org/dr17/data_access/value-added-catalogs/?vac_id=distmass:-distances,-masses,-and-ages-for-apogee-dr17

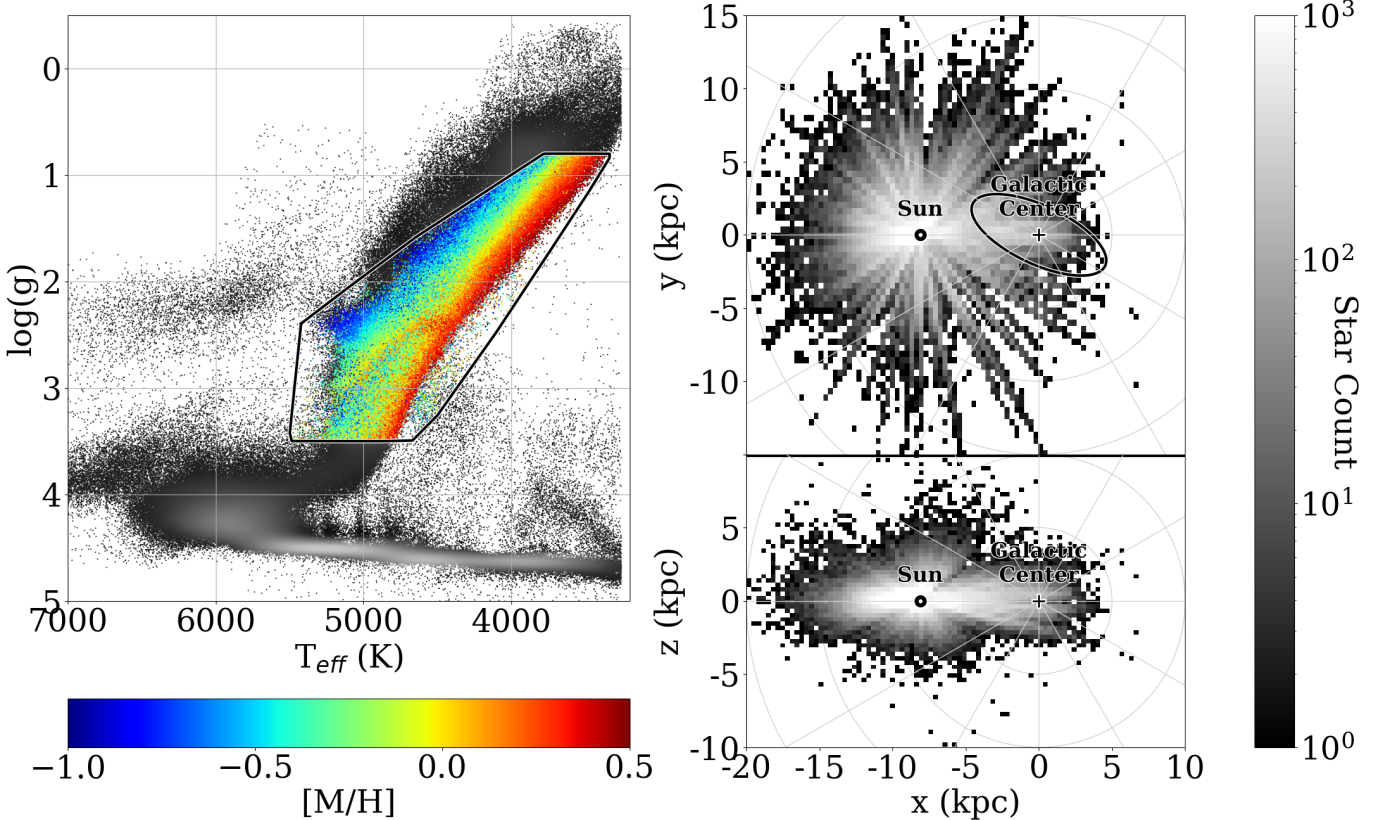


Figure 1. Summary of our red giant branch stellar sample from APOGEE. **Left:** The T_{eff} - $\log g$ distribution of our sample (with point color corresponding to metallicity) compared to the entire APOGEE catalog (in grayscale, density on the diagram). **Right:** The spatial distribution of our RGB sample, displayed as a face-on view of the Galactic disk (top), and an edge-on view (bottom). The plus (+) marks the location of the Galactic Center, the large circle (○) is the Sun. The ellipsoid is the approximate location of the Galactic bar.

Catalog	Parameter	Range	Notes
allStar	$\log g$	$0.8 < \log g < 3.5$	restrict sample to red giant stars
allStar	Targeting Bits	EXTRATARG= 0	main survey targets; no duplicates
allStar	ASPCAP Bits	ASPCAPFLAG ≠ 23	removes STAR_BAD stars with bad ASPCAP parameters
distmass	DISTMASS Bits	BITMASK ≠ 2	age estimates reliable; within training set range

Table 1. Summary of the various quality refinements made to our sample described in Section 2.3.

tribution of stars in the Galaxy; the selection function allows for this correction, but only for stars that were targeted randomly.

Next, we restrict the sample to red giant stars between the limits $0.8 \leq \log g \leq 3.5$. Red giant stars are luminous, allowing the sample to probe far distances in the Galaxy. The stellar parameters in APOGEE are known to have systematic uncertainties that vary with $\log g$ and T_{eff} (e.g., Jönsson et al. 2018; Eilers et al. 2022), the effects of which can be mitigated by limiting the sample to a small range in $\log g$. The average signal-to-noise ratio of our sample is $S/N = 222.18$.

We also remove any stars with unreliable ASPCAP stellar parameters using the STAR_BAD ASPCAP bit. This flag is triggered when the derived parameters for a star are designated a bad fit by its high χ^2 value, when the derived temperature does not match the star's observed color, when any individual stellar parameter measurement is flagged as bad, or when the derived parameters lie on an edge of the synthetic spectral grid and are unphysical.

We make an additional cut for the stellar age estimates using the distmass quality flag bit 2, indicating that a star's atmospheric parameters are within the region covered by the training set, meaning the neural

network is not allowed to extrapolate and the stellar age estimates are reliable (Stone-Martinez et al. 2024). This cut is partially redundant with the previous $\log g$ restriction, as the availability of asteroseismic data used to train the neural network is limited to $\log g \geq 0.8$ and age estimates are only available for giant stars due to the assumptions used in converting from stellar mass to age. Notably, this also removes all stars with metallicity $[M/H] \leq -0.7$, imposed by the parameter range covered by the training set. Metal-poor stars are expected to have extra mixing effects (Shetrone et al. 2019; Roberts et al. 2024, e.g.) that were not learned by the neural network because there are no metal-poor stars in the training set.

However, metal-poor ($[M/H] \leq -0.7$) stars make up a decent fraction of the high- α population (roughly 10%), and therefore we do not want to exclude them from our sample. For the high- α , metal-poor stars, we therefore assign an age estimate under the assumption that they follow the same age distribution as the rest of the high- α stars in the sample. This assumption is motivated by the predictions of chemical evolution models (e.g., Chiappini et al. 1997; Kobayashi et al. 2006) as well as previous age-resolved observational studies of the Milky Way (e.g., Haywood et al. 2013; Feuillet et al. 2018; Lian et al. 2022) which generally agree that high- α stars are uniformly old independent of their metallicity. We adopt an assumed age estimate for these stars by sampling all high- α stars in the $-0.4 < [M/H] < -0.7$ range and use their ages from `distmass` to determine the target age distribution. The metal-poor ($[M/H] \leq -0.7$) stars are then assigned an assumed age by re-sampling them to follow the target age distribution.

A summary of the sample restrictions implemented in this paper is presented in Table 1. A Kiel diagram and the spatial distribution of our sample after these refinements is shown in Figure 1. The final number of stars in our sample is 203,197.

2.4. Population Binning

To explore the history and evolution of the Milky Way, we further split our sample into **mono-age**, **mono-abundance** stellar **populations** (referred to here as “MAAPs”) by groups of similar age, metallicity ($[M/H]$), and α -element abundances ($[\alpha/M]$) to approximate simple stellar populations.

We define two bins in α -element abundances, separated in the $[\alpha/M]$ - $[M/H]$ plane with the equation from Patil et al. (2023) (their eq. 24):

$$[\alpha/M] = 0.1754 * [M/H]^3 + 0.1119 * [M/H]^2 - 0.1253 * [M/H] + 0.1353 - 0.05 \quad (1)$$

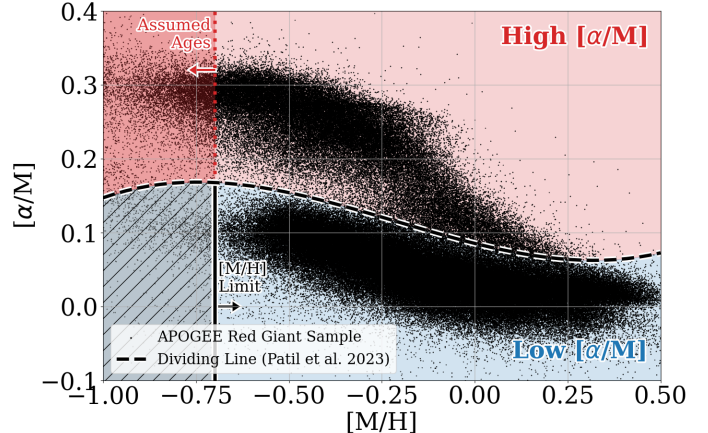


Figure 2. The metallicity ($[M/H]$) and alpha-element abundance ($[\alpha/M]$) distribution covered by our sample, showing the designated separation between low- α and high- α samples defined in Equation 1. The vertical line at $[M/H] = -0.7$ dex marks the lower metallicity limit of the `distmass` stellar age estimates.

This equation was derived using statistical techniques to separate the two populations in copula space, using a coordinate transformation to extract statistical structure from data. We added a small -0.05 dex offset (noted in italics) to account for abundance differences because Patil et al. (2023) used $[\text{Mg}/\text{Fe}]$ instead of $[\alpha/\text{M}]$.

This separation is shown in Figure 2. The two bins are hereafter referred to as the low- α and high- α populations.

In metallicity, we split the sample into 15 equal-sized bins ranging between $-1.0 \leq [M/H] \leq 0.5$ with spacing of $\Delta [M/H] = 0.1$ dex. This is significantly larger than the typical ASPCAP uncertainty in $[M/H]$, which is generally on the order of 0.01 dex.

In stellar age, we define 12 bins between $9.0 \leq \log_{10}(\text{age [yr]}) \leq 10.2$ (corresponding to $1.0 \leq \text{age} \leq 15.8$ Gyr) with spacing of $\Delta \log_{10}(\text{age}) = 0.1$. The age bins are handled in log space because it is more representative of the expected uncertainties associated with the stellar age estimates, which are typically around $\log_{10}(\text{age}) = 0.15$. The age bin size is larger than the age uncertainties, so there will be some expected overlap between bins and the results may be artificially broadened in this direction. The youngest age bin goes only down to 1.0 Gyr, as there are not enough young stars in our red giant sample to extend the range lower. In Zasowski et al. (*in prep*), younger MAAPs are generated and shown not to significantly change the main conclusions of this work.

The number of stars from our sample in each resulting mono-age mono-abundance stellar population is shown in Figure 3. For the remainder of this paper, each bin is

considered a single stellar population and worked with independently of the rest unless otherwise specified.

3. METHOD

In the methodology developed by Bovy et al. (2012b); Bovy & Rix (2013); Rix & Bovy (2013); Bovy et al. (2016a,b), the probability that any given star was observed in an astronomical survey is directly proportional to the overall density of the Galaxy at the star’s location, after accounting for the survey selection function which includes the distribution of dust. Using this technique, the density structure and stellar mass contribution can be recovered for various components of the Galaxy (e.g., Bovy et al. 2012b; Rix & Bovy 2013; Bovy et al. 2016a,b; Mackereth et al. 2017; Mackereth & Bovy 2020; Yu et al. 2021; Lian et al. 2022), revealing the history and evolution of the Milky Way through the present-day distribution of its stellar populations.

In this study, we follow this approach and fit for the density distribution of each stellar population bin defined in Section 2.4 independently. This allows us to explore how the structural parameters of the Milky Way vary with stellar age, metallicity, and α -element abundance. In this section, we provide an overview of the methodology in Section 3.1, describe the APOGEE selection function in 3.2, present our density models and corresponding parameters in 3.3, and summarize the practical computational application of this procedure in 3.4.

3.1. Density Fitting Methodology

In a randomly-selected sample of stars, the probability that any given star was observed is proportional to the overall stellar number density of the Galaxy at the star’s location. Therefore, the number counts of stars observed in a stellar survey like APOGEE can be used to fit a density model with generic parameters θ to recover the underlying density distribution for each sub-population of stars.

Bovy et al. (2012b); Rix & Bovy (2013); Bovy et al. (2016a,b); Mackereth et al. (2017) have developed a methodology to determine the underlying density profile of a population of stars based on this probability. The rate at which stars have been observed in a stellar survey like APOGEE, as a function of position, color, and metallicity, is well-modeled by an inhomogeneous Poisson point process. The remainder of this section restates the methodology from these studies, which we adopt to fit the density parameters of the stellar populations in this paper. The expected rate of observation in number

counts $\lambda(O|\theta)$ for a given stellar number density model ν_* with parameters θ is expressed as:

$$\begin{aligned} \lambda(O|\theta) = & \nu_*(X, Y, Z \mid \theta) \times |J(X, Y, Z; l, b, D)| \\ & \times \rho(H, [J - K_S]_0, [\text{Fe}/\text{H}] \mid X, Y, Z) \\ & \times S(l, b, H) \end{aligned} \quad (2)$$

where $\nu_*(X, Y, Z \mid \theta)$ is the number density of stars (with units of stars kpc^{-3}) in Galactocentric rectangular coordinate. This is the quantity we wish to match to the observed number counts in APOGEE. The exact form of the density model we adopt is presented later in Section 3.3, but we continue this discussion with a generalized density model with arbitrary parameters θ . The second term, $|J(X, Y, Z; l, b, D)|$ is the Jacobian transformation from rectangular Galactocentric coordinates (X, Y, Z) to the observable Galactic latitude, longitude, and distance coordinates (l, b, D) . The third term, $\rho(H, [J - K_S]_0, [\text{Fe}/\text{H}] \mid X, Y, Z)$ is the assumed density of stars in magnitude, color, and metallicity space from stellar evolution theory. Finally, $S(l, b, H)$ is the survey selection function, the fraction of the total underlying population of stars that was observed by APOGEE for each magnitude, color, and metallicity bin. The selection function includes the effects of dust extinction, and is discussed in more detail in Section 3.2.

Finding the density model that best matches the observed data becomes a maximum-likelihood problem matching the rate function to the observed number counts. For each population of stars, the likelihood $\mathcal{L}(\theta)$ that an underlying density model with parameters θ produced the observed number counts is written as:

$$\ln \mathcal{L}(\theta) = \sum_i \left[\ln \nu_*(X_i, Y_i, Z_i \mid \theta) - \ln \int dO d\lambda(O|\theta) \right] \quad (3)$$

where $\nu_*(X_i, Y_i, Z_i \mid \theta)$ is evaluated at the position of each observed star i and summed over all observations. The second term, $\int dO d\lambda(O|\theta)$, is the “effective volume” of the survey, or the predicted total number of stars that APOGEE would have observed in a galaxy with density model parameters θ , given the survey selection function and the effects of dust. This term is necessary to regularize the likelihood $\mathcal{L}(\theta)$; without it, the density model with the highest likelihood would always be the model with the highest overall density. The effective volume is an intrinsic property of the survey for each given density model, and is independent of the observed number counts. For a pencil-beam style survey like APOGEE, which observed stars along targeted

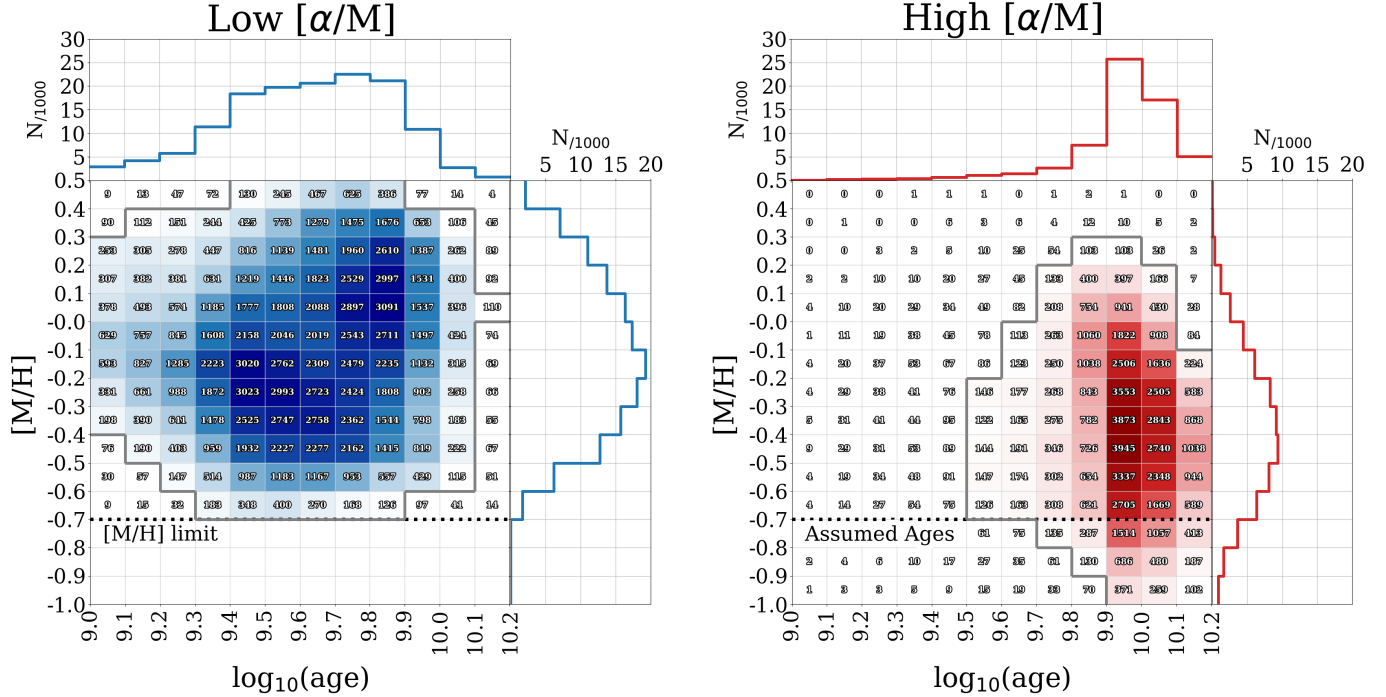


Figure 3. The number of stars in our sample for each stellar population bin, separated by the low- α (blue; left) and high- α (red; right) samples and different bins in stellar age (x-axis) and metallicity (y-axis). The number of stars in each population is printed in the corresponding bin and represented by color intensity. The dark gray outline highlights bins with more than 100 stars, which is the limit for our parameter fitting. Flattened histograms of each axis are shown above (age distribution) and to the right (metallicity distribution) for each panel.

lines-of-sight (or “fields”), the effective volume can be expressed as:

$$\int dO d\lambda(O|\theta) = \sum_{\text{fields}} \Omega_f \int dD D^2 \nu_*([X, Y, Z](D, \text{field})|\theta) \quad (4)$$

$$\times \mathfrak{S}(\text{field}, D)$$

where Ω_f is the solid angle covered by each APOGEE field. The number density $\nu_*([X, Y, Z](D, \text{field})|\theta)$ is the density model evaluated along the line-of-sight (distance D) for a given field, the integral of which gives the total number of stars expected in the field for that set of θ . Finally, that number is multiplied by the effective survey selection function $\mathfrak{S}(\text{field}, D)$, the fraction of stars out of the total number present that would actually be observed, accounting for survey observation strategies and the presence of dust. This important term is non-trivial to calculate and explained in more detail in Section 3.2.

For practical application in this study, we derive the best-fit parameters θ for each stellar population bin using a Markov-Chain Monte Carlo (MCMC) sampling of the likelihood function (equation 3), described more in Section 3.4.

3.2. APOGEE Selection Function

A selection function is broadly defined as the fraction of stars (or more generalized “targets”) observed by an astronomical survey out of the total intrinsic number of targets existing, often presented as a function of spatial position. There are two main complications to account for in the calculation of the selection function for APOGEE: the targeting strategies of the survey, and the presence of interstellar dust in the Galaxy which obscure potential observations. The targeting strategies of the survey produce what will hereafter be referred to as the *raw selection function*, the fraction of stars observed in APOGEE as a function of Galactic location (l, b) (or field in APOGEE), apparent magnitude H , and $(J - K)_0$ color. The quantity needed to calculate the effective volume in Equation 4 is called the *effective selection function*, which is the fraction of stars observed as a function of Galactic location (l, b) (field), and distance along the line-of-sight. The raw selection function is essentially a 2D sky projection, whereas the effective selection function is a 3D Galactic map. The calculation of the effective selection function requires the raw selection function, a three-dimensional dust map, and some assumption of the expected distribution of stars from stellar evolution theory (i.e., from a set of isochrones).

To evaluate the raw selection function of APOGEE, the targeting procedures of APOGEE must be well understood. Full details on the targeting strategies and motivations can be found in [Zasowski et al. \(2013, 2017\)](#) for previous data releases of APOGEE, [Beaton et al. \(2021\)](#) for the final data release from the northern hemisphere (APOGEE-N), and [Santana et al. \(2021\)](#) for the southern hemisphere (APOGEE-S). A brief overview of APOGEE’s targeting procedure, as relevant to this study, is described here.

Any application of the raw selection function inherently assumes stars were randomly targeted, which is only true for the “main survey sample” in APOGEE. Other observations which include ancillary program targets observed for a specific science purpose (e.g., satellite or dwarf galaxy targets, star cluster member candidates, *Kepler* Objects of Interest) were removed from our sample previously with the cuts described in Section 2.3. Main-survey APOGEE targets are randomly selected from the 2MASS catalog ([Skrutskie et al. 2006](#)), separated into different lines-of-sight across the sky (referred to as fields) and in bins of apparent magnitude H , and dereddened $(J - K)_0$ color.

The magnitude bins are referred to as *cohorts* in APOGEE. Each field can have up to 3 cohorts, referred to as the short, medium, and long cohort, usually corresponding to the brightest (short) to faintest (long) groups of stars respectively, which need different amounts of telescope time for adequate signal-to-noise. The exact H -band magnitude limits that define a cohort can vary on a field-to-field basis.

After binning by magnitude, the sample is further split into bins of dereddened $(J - K)_0$ color to select targets for APOGEE. Each field can have up to 2 bins in color space, which vary between fields depending on which Galactic component (disk, halo, or bulge) is sampled by the direction of the field. In APOGEE-1 (observations from 2014 and prior), a single color limit of $(J - K)_0 \geq 0.5$ was used for fields that targeted the Galactic disk (defined by latitude $|b| \leq 25^\circ$). In APOGEE-2, two different limits of $0.5 \leq (J - K)_0 \leq 0.8$ and $(J - K)_0 \geq 0.8$ were imposed for the disk to increase the number of distant stars sampled. In both iterations of the survey, fields in the direction of the Galactic halo (latitude $|b| \geq 25^\circ$) were selected with a bluer color limit of $(J - K)_0 \geq 0.3$. Halo-defined fields frequently include foreground disk stars which are included in this study. Bulge fields towards the center of the galaxy have a single color limit of $(J - K)_0 \geq 0.5$. For every APOGEE field, in each of these bins in color-magnitude space, targets were randomly selected from a list of all possible sources in the 2MASS catalog ([Skrutskie et al. 2006](#)).

We evaluate the raw selection function for each field in the same color-magnitude bins as used for targeting. The formulation of the raw selection function $S(\text{field}, k)$ is straightforward, as the ratio of number of observed stars N_{APOGEE} to the number of all possible targets N_{2MASS} :

$$S(\text{field}, k) = \frac{N_{\text{APOGEE}}}{N_{\text{2MASS}}} \quad (5)$$

where k is a color-magnitude bin defined by the targeting strategies on a field-by-field basis, N_{APOGEE} is the number of stars for which APOGEE spectra were obtained, and N_{2MASS} is the total number of possible targets from the 2MASS photometry catalog, assumed to be complete within the APOGEE magnitude limits. We calculate this fraction for every field, color, and magnitude combination using the publicly available `apogee`⁴ Python module, originally developed in [Bovy et al. \(2016a\)](#) and adapted for DR17 in this work.

The APOGEE raw selection function is used as one ingredient in the effective selection function, which transforms the selection fraction in color-magnitude bins into a selection fraction purely based on position in the Galaxy (field location and distance). For each field, the effective selection function is evaluated at many distances along the line-of-sight, and assumed to be constant across the solid angle area covered by the field. The effective selection function is evaluated by summing across all targeting color-magnitude bins as:

$$\mathfrak{S}(\text{field}, D) = \sum_k S(\text{field}, k) \int \frac{\Omega_k(M_H)}{\Omega_f} dM_H \quad (6)$$

where $S(\text{field}, k)$ is the raw selection function described previously. M_H is the expected distribution of absolute magnitudes for a stellar population at distance D , estimated from stellar evolution theory using a set of isochrones. In this work, we use a set of the PARSEC isochrones ([Bressan et al. 2012; Chen et al. 2014](#)), using appropriate age and metallicity selections for each stellar population bin we wish to fit and adopting a Kroupa initial mass function ([Kroupa 2002](#)). The metallicity and age range of the isochrones is the same as our stellar population bins, with a metallicity range of $-0.7 \leq [M/H] \leq 0.5$ and an age range of $9.0 \leq \log(\text{age}) \leq 10.2$ in step size of $\Delta[M/H] = \Delta \log(\text{age}) = 0.1$. Finally, dust is accounted for in the last term, $\frac{\Omega_k}{\Omega_f}$, which is the area percentage on the plate that a star would be observable given the distribution of dust in that part of the

⁴ <https://github.com/jobovy/apogee>

Galaxy. Ω_f is the total solid angle covered by the field, and Ω_k is the observable area of the field not obscured by dust for a given distance, defined in more detail as:

$$\begin{aligned}\Omega_k(M_H) &= \Omega(H_{\min} < m_H < H_{\max}) \\ m_H &= M_H + \mu(D) + A(l, b, D)\end{aligned}\quad (7)$$

where $H_{\min, \max}$ denotes the apparent magnitude limits for each APOGEE cohort and color bin k from targeting. The distribution of apparent magnitude m_H is calculated from absolute magnitudes M_H of the stellar population from the isochrones, combined with the distance modulus $\mu(D)$ and the extinction value $A_H(l, b, D)$ retrieved from a dust map.

Putting this into plain words, the $\frac{\Omega_k}{\Omega_f}$ term of the effective selection function tests where a hypothetical star (or a distribution of isochrone points) would be observable within APOGEE by moving it along line-of-sight through the dust map. If the star is too close to the Sun, its apparent magnitude would be brighter than the APOGEE targeting limit ($m_H < H_{\min}$) and it would not have been selected for observation. If the star is too far away or obscured by dust, it would also not be observable ($m_H < H_{\max}$), as the magnitude or color would once again fall outside APOGEE’s targeting range. Because the dust maps are typically resolved within the area of an APOGEE field (solid angle Ω_f), this “test” results in a fraction of observability (i.e., the star could have been observed if it was on this 50% of the plate) instead of the binary used in this simplified example (i.e., the hypothetical star either was or was not observed).

This “observability test” is repeated for the full distribution of isochrone points and summed over the integral in equation 6. This integral is deceptively complex, as each isochrone point has to be weighted by its contribution to the stellar population. This includes the choice of an assumed initial mass function (IMF), for which we elect to use the two-part power law Kroupa IMF (Kroupa 2002). The integration over the full population goes as:

$$\int \frac{\Omega_k(M_H)}{\Omega_f} dM_H = \sum_i \frac{\Omega_k(M_H)}{\Omega_f} * \xi(m_i) \quad (8)$$

where the sum over i corresponds to each isochrone point. The initial mass function comes in $\xi(m_i)$, which is the number of expected observations of each star per unit stellar population mass, evaluated for the stellar mass of each isochrone point. Practically, this quantity is provided by the difference between two consecutive values in the INT_IMF column in the PARSEC isochrones that we use (Bressan et al. 2012; Chen et al. 2014). This sum weights each isochrone point by its contribution to

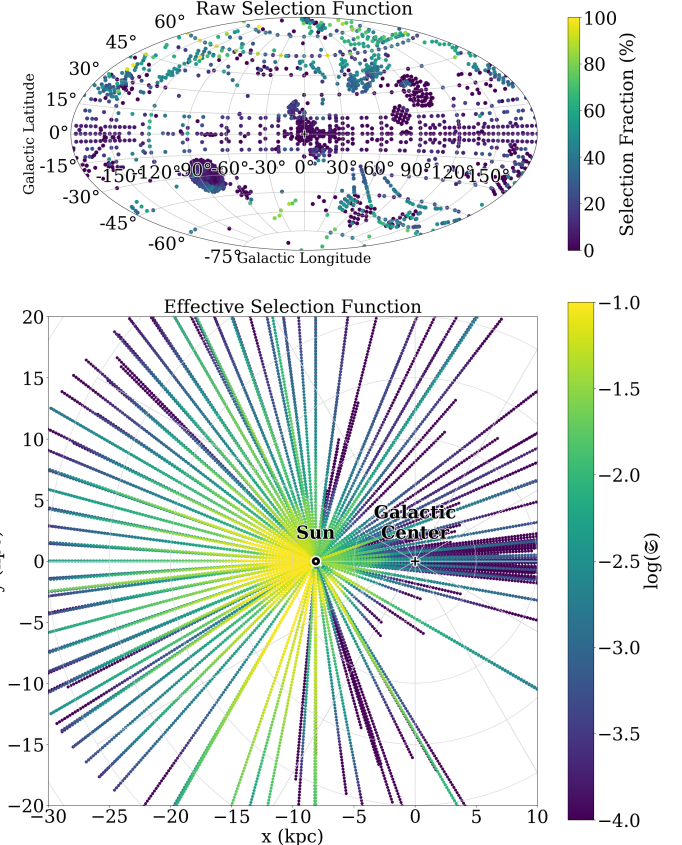


Figure 4. The APOGEE selection functions. **Top:** The raw Selection Function, reflecting the targeting strategies of APOGEE, displayed as the selection fraction (color) based on the APOGEE field position on the sky. **Bottom:** The Effective Selection Function, reflecting APOGEE’s sampling of the intrinsic distribution of stars in the Milky Way, shown for within 10 deg of disk midplane.

the IMF: lower mass stars are more numerous, so they will contribute more to the effective selection function than their high-mass siblings.

The dust map for determining extinction values $A_H(l, b, D)$ is another important choice to make when computing the effective selection function. No single 3D extinction map covers the whole sky, therefore a combination of several maps is necessary to sample the entire Galaxy. We use a combination of three dust maps (Drimmel et al. 2003; Marshall et al. 2006; Green et al. 2019) distributed as the “Combined 2019” map in the `mwdust`⁵ package, first described in Bovy et al. (2016a). For readers interested in how the choice of dust map or the uncertainties in the extinction values may influence the selection function, we point to Bovy et al. (2016a) (their Section 4.2 and Figure 6). Typical uncertainties

⁵ <https://github.com/jobovy/mwdust>

for the effective selection function due to the choice of dust map are on the order of $\sim 10^{-3}$.

The final effective selection fraction $\mathfrak{S}(\text{field}, D)$ gives the ratio of observed stars to the intrinsic number of stars in the Milky Way, as a function of APOGEE field and distance along each line-of-sight.

Both selection functions are shown in Figure 4. The raw selection function is shown in the top panel. Observation fields close to the disk plane generally have a lower raw selection fraction simply because there are more stars in the disk. The effective selection function is shown in the bottom panel. The effective selection fraction is mainly correlated with distance, where stars closer to the Sun generally have a higher selection fraction than those farthest away, with significant variation due to the inhomogeneous distribution of dust. For example, lines-of-sight towards the Galactic center have lower effective selection fractions due to the higher concentration of dust.

3.3. Stellar Density Profiles

In the previous sections, the density fitting methodology was formulated as a maximum likelihood problem using a generic density profile $\nu_*(X, Y, Z)$ with arbitrary parameters θ . In this section, we describe the exact form of the density profiles adopted to fit each population of the Milky Way, and describe the relevant structural parameters.

We formulate the total stellar number density of the disk ν_* as the product of the radial profile $\Sigma(R)$, the vertical density profile $\xi(R, Z)$, and a normalization factor ν_\odot :

$$\nu_*(R, \phi, Z) = \nu_\odot \Sigma(R) \xi(R, Z) \quad (9)$$

The normalization factor ν_\odot is defined as the stellar number density at R_\odot and is the overall amplitude of the density profile. The likelihood equation (equation 3) is independent to this parameter, as it drops out of the equation because it is included in both the model and the effective volume terms in equation 3. Instead, this value can be derived using the observed star counts in APOGEE for each stellar population bin corrected for the selection function, following the approach from Bovy et al. (2012a, their Appendix A) and Mackereth et al. (2017, their Section 3.3):

$$\nu_\odot = \frac{N_{\text{APOGEE}}}{\int dO d\lambda(O|\theta)} \quad (10)$$

where N_{APOGEE} is the number of stars in our sample for a given stellar population bin and $\int dO d\lambda(O|\theta)$ is the effective volume as described in Equation 4. The effective volume is the integral of the selection function

over the survey volume for a given density model, and is dependent on the other parameters θ .

This profile assumes azimuthal symmetry in the disk depending only on Galactocentric radius R and height above the plane Z , and contains no terms for the spiral arms, bar, or bulge.

When applicable, all parameters are scaled to the value at the Solar neighborhood (R_\odot), the natural center of the observations and where we have the most data. As before, we define the solar position as $R_\odot = 8.3$ kpc and $Z_\odot = 27$ pc (Bland-Hawthorn & Gerhard 2016).

For the radial profile $\Sigma(R)$, an exponential form is commonly adopted for disk galaxies (e.g., Freeman 1970; Gilmore & Reid 1983; Robin et al. 2003; Pohlen & Trujillo 2006). Previous studies on the Milky Way have found that for many stellar populations (particularly the low- α stars in relatively narrow age bins), a broken exponential profile is a better fit to the data (e.g., Bovy et al. 2012b, 2016b; Mackereth et al. 2017; Lian et al. 2022). Here, we adopt a broken exponential profile for the radial distribution:

$$\ln \Sigma(R) \propto \begin{cases} -h_{R,\text{in}}^{-1}(R - R_\odot) - C & \text{where } R \leq R_{\text{break}} \\ -h_{R,\text{out}}^{-1}(R - R_\odot) & \text{where } R > R_{\text{break}} \end{cases} \quad (11)$$

where $h_{R,\text{in}}$ is the scale length of the inner disk, $h_{R,\text{out}}$ is the scale length of the outer disk, and R_{break} is the radius at which the break occurs. C is a normalization factor to ensure that the profile is continuous at the break radius, such that $C = (h_{R,\text{out}}^{-1} - h_{R,\text{in}}^{-1}) * (R_{\text{break}} - R_\odot)$. This profile does not exclude the possibility of a single exponential profile being the best fit, which would be the case if $h_{R,\text{in}} = h_{R,\text{out}}$.

The vertical profile is modeled as a single exponential in Z , but allowed to vary with radius R , accounting for a “flared” population that has a larger scale height at large radii than near the center of the disk, as observed previously in the Milky Way for different populations (e.g., Bovy et al. 2012b, 2016b; Mackereth et al. 2017; Lian et al. 2022; Robin et al. 2022).

While some studies (Bovy et al. 2012b, 2016b; Mackereth et al. 2017) have used an exponentially flaring profile (such that the scale height varies exponentially with radius characterized by its own scale length), more recent studies have shown that a profile which flares *linearly* with radius better approximates the vertical distribution of stars in the Milky Way (Yu et al. 2021; Lian et al. 2022). The corresponding linear flaring term,

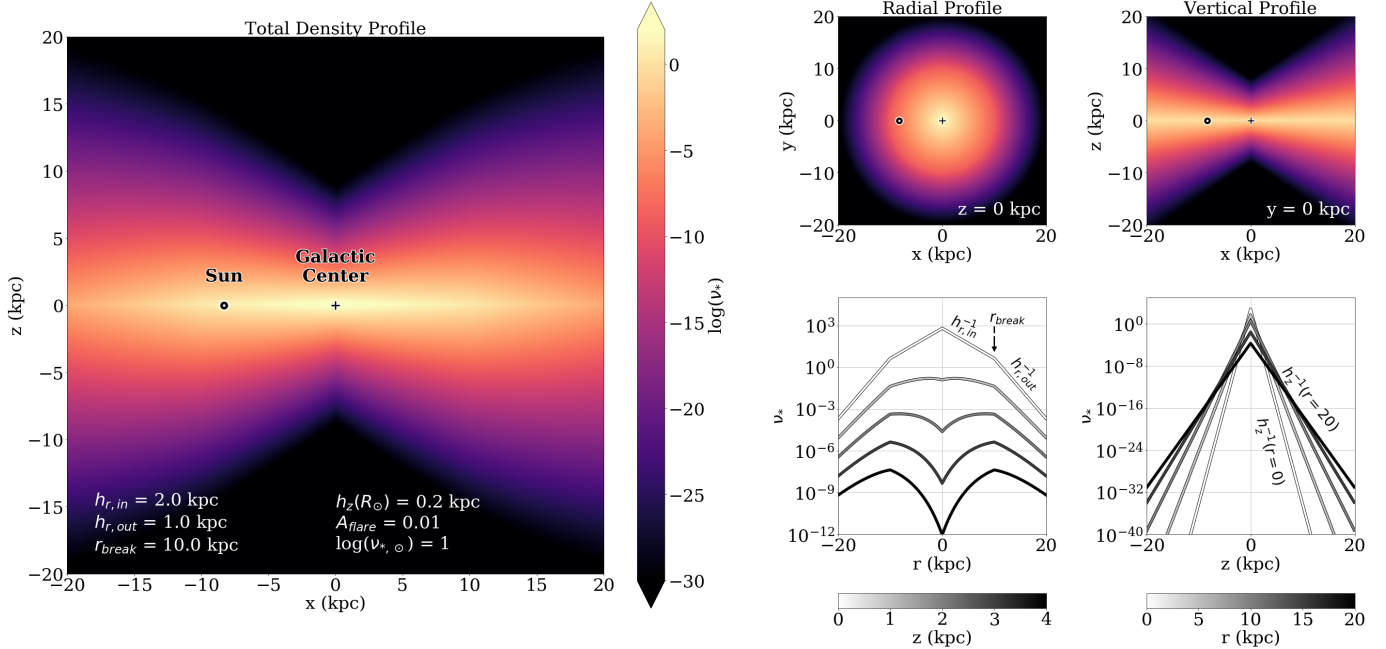


Figure 5. A visual example of the stellar number density model described in Section 3.3, which we use to fit each of the stellar populations in the sample. **Large Left Panel:** the total number density profile (Equation 9) in the edge-on view $x - z$ plane. The total number density profile is the product of the radial profile (Equation 11) and vertical profile (Equation 12). **Middle-Top:** The radial density profile is modeled as a broken exponential (Equation 11), shown here face-on in the $x - y$ plane. **Middle-Bottom:** The total radial density profile (same as left panel) shown in different slices of height above the plane z . **Top-Right:** The vertical profile, a single exponential with radial flaring (Equation 12), in the $x - z$ plane. **Bottom-Right:** The total vertical density profile (same as left panel) shown at different radii. The flaring term causes the scale height to increase with radius.

A_{flare} , is the slope of the scale height varying with radius and represents the strength of the flaring.

$$\begin{aligned} \ln \xi(R, Z) &\propto -h_Z(R)^{-1}|Z| \\ h_Z(R) &= h_{Z\odot} + A_{\text{flare}}(R - R_\odot) \end{aligned} \quad (12)$$

where $h_{Z\odot}$ is the scale height of the disk at R_\odot and A_{flare} is the slope of the flaring varying with radius.

To summarize, a total of six free parameters characterize our density model, summarized in Table 2; three parameters for the radial profile ($h_{r,\text{in}}$, $h_{r,\text{out}}$, and r_{break}), two parameters for the vertical profile ($h_{Z\odot}$ and A_{flare}), and one scaling parameter (ν_\odot) as the number density at the Sun. Figure 5 provides a visualization for an example model with arbitrary (but reasonable) parameters.

3.4. Practical Application & MCMC

As outlined in Section 3.1, deriving the structural parameters of each stellar population becomes a maximum likelihood problem, with Equation 3 predicting the likelihood $\mathcal{L}(\theta)$ that a model with parameters θ would produce the observations.

We sample the likelihood function using a Markov-Chain Monte Carlo (MCMC) algorithm to derive the

best-fit structural parameters for each stellar population. We implement this optimization using the Python `emcee` module, setting up the six-parameter problem using 100 walkers and 1,000 steps (after an initial burn-in period of 500 steps), totaling 100,000 iterations considered for each stellar population fit. If the results have not converged after 1,000 steps, the chain is allowed to continue for another 1,000 steps until it does.

We restrict the region of parameter space the MCMC chain is allowed to sample using the priors noted in Table 2. The priors are flat, with the likelihood function automatically returning $\ln \mathcal{L}(\theta) = -\infty$ if the parameter falls outside the designated range. These priors were chosen motivated by results from previous studies, but are generous enough to allow the model to sample a wide range of physically possible values. The starting guess for each parameter is selected randomly within the range of the priors.

Computationally, both the radial density profile (equation 11) and the vertical density profile (equation 12) are treated as equalities in the model, which is equivalent to setting the scaling of each such that $\Sigma(R_\odot) = 1$ and $\xi(R_\odot, 0) = 1$ at the Sun. They are scaled to a true number density together in the combined profile (equa-

Parameter	Units	Description	Priors	Eq.
ν_\odot	$N \text{ kpc}^{-3}$	scaled amplitude, the stellar number density at R_\odot	None (calculated from star counts)	9, 10
$h_{R,\text{in}}$	kpc	scale length of inner disk	$-5 \leq h_{R,\text{in}}^{-1} \leq 5$	11
$h_{R,\text{out}}$	kpc	scale length of outer disk	$0 \leq h_{R,\text{out}}^{-1} \leq 5$	11
R_{break}	kpc	radius of the break in the exponential	$0 \leq R_{\text{break}} \leq 30.0$	11
$h_{Z\odot}$	kpc	scale height of the disk at the solar radius	$0 \leq h_{Z\odot} \leq 2.5$	12
A_{flare}	none	disk flaring term; slope of variation in h_Z with radius	$0 \leq A_{\text{flare}} \leq 0.1; h_Z(R=0) \geq 0$	12

Table 2. Summary of the six parameters characterizing the density profile.

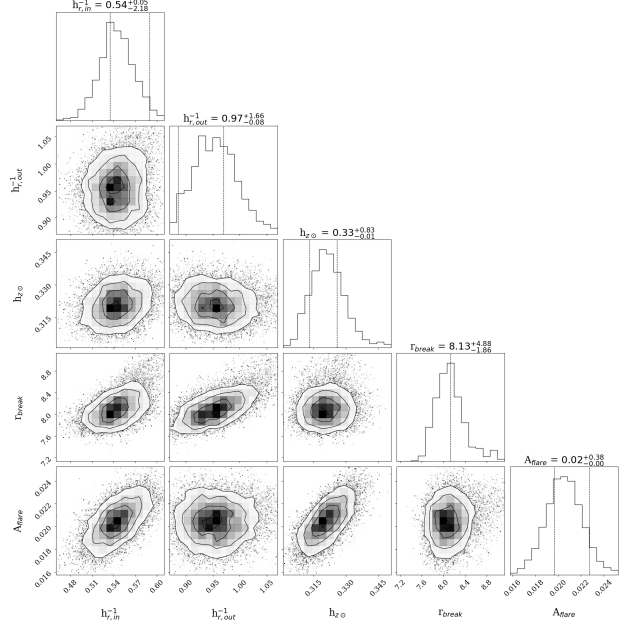


Figure 6. Example corner plot showing the MCMC results for the low- α stellar population bin centered at $[\text{M}/\text{H}] = 0.15$ dex and $\log(\text{age}) = 9.6$.

tions 9) using the derived number density outlined in equation 10.

The effective selection function (\mathfrak{S} ; equation 6) is pre-calculated along a grid of heliocentric distances prior to the likelihood fitting for computational efficiency. For each stellar age and metallicity bin, the effective selection function is computed for each APOGEE field for a distance range $0 \leq d \leq 25$ kpc and saved. This allows for a quicker computation of the effective survey volume (Equation 4) for any given set of model parameters, greatly reducing the computation time of the likelihood calculation.

The best-fitting set of parameters and associated uncertainties for each population of stars is presented in Section 4, defined as the median value and standard deviation (σ) of the last 10% of each MCMC chain. An example corner plot showing the best-fit parameters and spread in the MCMC chain for one of the stellar population bins is shown in Figure 6.

All code required for reproducing the APOGEE selection function, the density profile MCMC fits, and the figures used in this study is provided at https://github.com/astrojimig/mw_density_imig2025.

4. RESULTS

For each stellar population separated by age, metallicity, and α -element abundances (Figure 3), we independently fit the density profile described in Section 3.3 to derive the six best-fit parameters (Table 2) for each population. A full table listing our results for each stellar population bin is available in Appendix Table A1. This section presents these results, organized by the radial parameters in 4.1, the vertical parameters in 4.2, and the overall mass contribution in 4.3. Our results are compared to previous studies in Section 6.1, and the subsequent implications for the formation of the Milky Way are reserved for discussion in Section 6.2.

4.1. Radial Density Profile

The derived best-fit parameters for the broken exponential radial profile (Equation 11), including the inner-disk scale length ($h_{r,\text{in}}$), outer-disk scale length ($h_{r,\text{out}}$), and the radius of the break (r_{break}) are shown in Figure 7 as a function of the different stellar populations.

Inner Scale Length: The inner-disk scale length increases with age and metallicity in the low- α disk (Figure 7, top row). At young ages and low metallicities, the derived scale length is negative, corresponding to a sharply-peaked “donut” shaped profile in the broken exponential in Equation 11 and Figure 5, with a peak density at the break radius of r_{break} instead of a monotonically-declining disk profile. As age and metallicity increase, the density profile of the inner disk eventually flattens ($h_{r,\text{in}}^{-1} = 0$ being perfectly horizontal), and reverses, until the density consistently decreases with radius everywhere.

Outer Scale Length: The outer-disk scale length increases with age and decreases with metallicity in the low- α disk (Figure 7, middle row), with trends perpendicular to the gradient seen with the inner disk-scale length (the inner scale length increases from bottom left

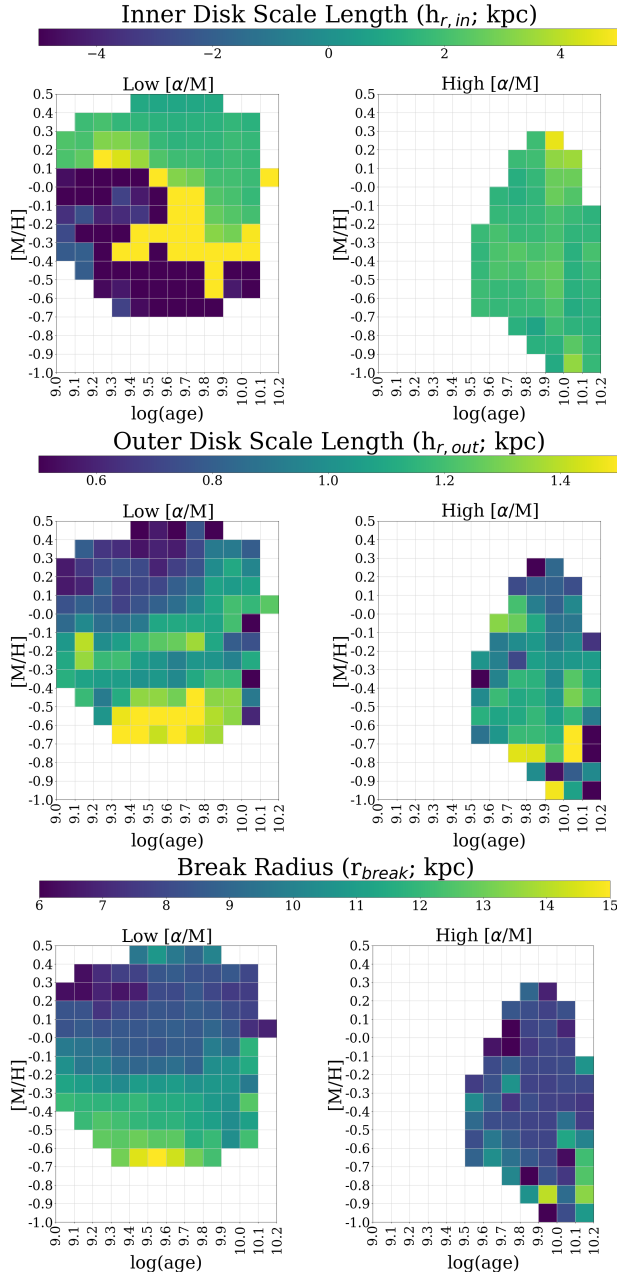


Figure 7. Radial profile parameters best-fit results, including inner scale length ($h_{r,in}$; top), outer scale length ($h_{r,out}$; middle), and break radius (r_{break} ; bottom). Each row is set up with the same grid layout as Figure 3 to show the trends across stellar populations: low- α (left) and high- α (right), split into corresponding bins of metallicity (rows) and stellar age (columns) in the grid. The color indicates the parameter, with the noted values on the color scale. A white color indicates that there were not enough stars in that population bin to perform a fit.

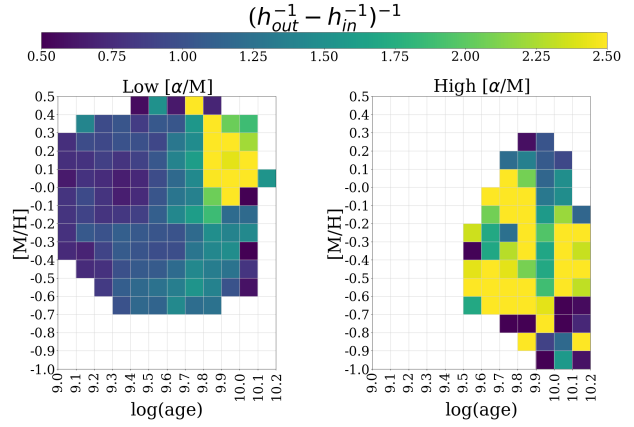


Figure 8. Quantifying the “broadening metric” with the same grid setup as Figure 7. The broadening metric quantifies the difference between the inner scale length $h_{r,in}$ and outer scale length $h_{r,out}$. A small broadening metric (blue colors) corresponds to a sharply-peaked “donut”-shaped profile, where a large broadening metric (yellow colors) approaches a single exponential profile.

to top right, the outer scale length gradient increases from top left to bottom right).

Break Radius: The break radius r_{break} seems independent of age but correlates with metallicity in the low- α populations. The metal-poor populations have a larger break radius ($r_{break} \sim 12$ kpc) than those of the metal-rich populations ($r_{break} \sim 6$ kpc).

For the high- α group, $h_{r,in}$ and $h_{r,out}$ tend to be of similar magnitude (note the different scales on the color bars). This means that shape of the density profile of these populations approximates a single-exponential profile rather than the broken exponential profile of the low- α stars, and r_{break} has little meaning. The high- α populations have a shorter scale length than the low- α stars of comparable age and metallicity, in both $h_{r,in}$ and $h_{r,out}$.

Profile Broadening: Quantifying the difference between $h_{r,in}$ and $h_{r,out}$ is a useful test to measure how sharply peaked or broadened the radial profile is. Figure 8 highlights the “broadening metric”, defined as $(h_{r,out}^{-1} - h_{r,in}^{-1})^{-1}$, which quantifies how broad each profile is. A high value of the broadening metric indicates that there is little difference between $h_{r,in}$ and $h_{r,out}$, and that particular population could be well modeled by a single-exponential profile. A small value of $(h_{r,out}^{-1} - h_{r,in}^{-1})^{-1}$ represents a strongly peaked profile, or a donut-shaped locus of stars around the Milky Way. The broadening metric has little correlation with metallicity or α -element abundances, but is strongly correlated with age for all populations: old populations tend to be very broad, and young populations tend to be sharply peaked.

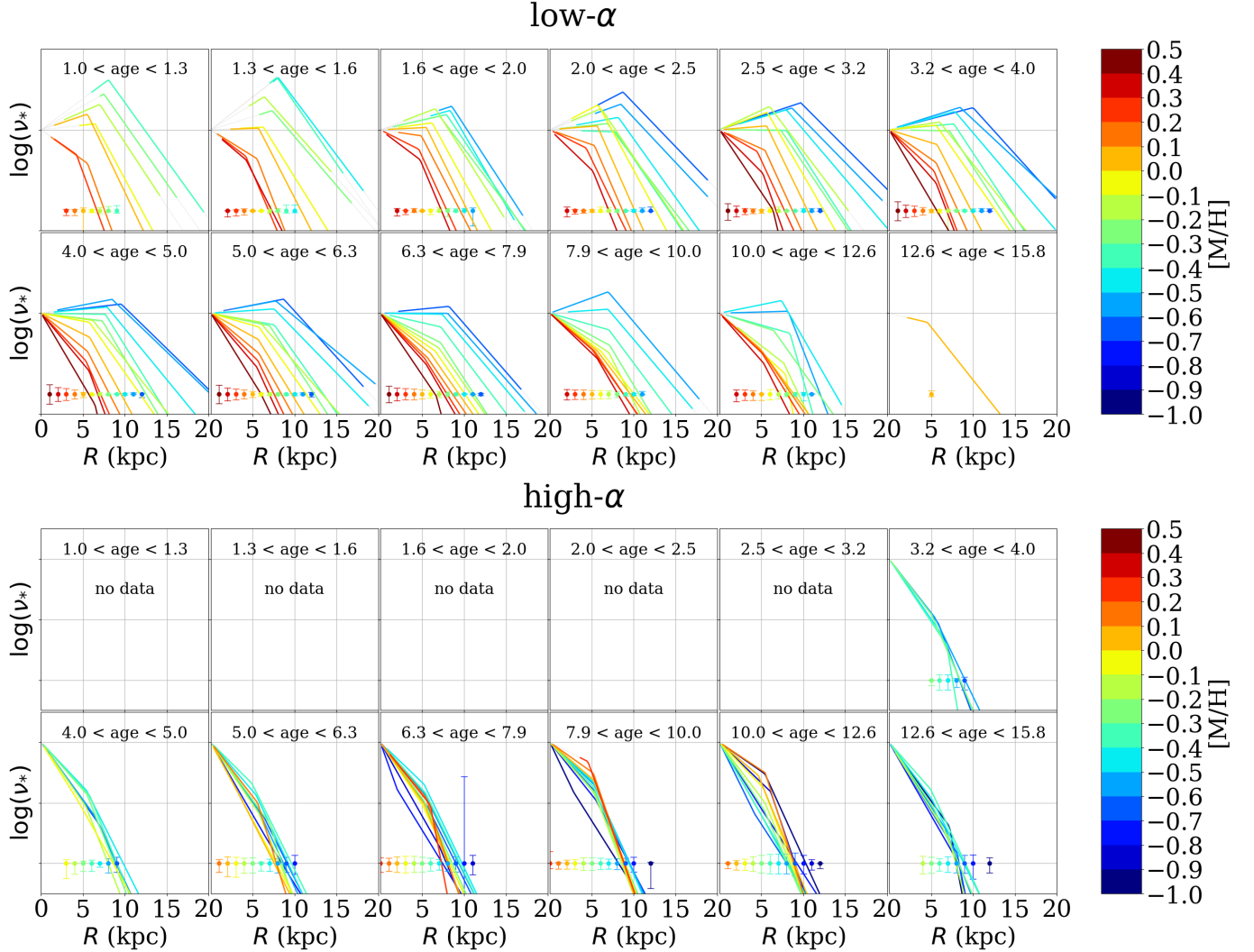


Figure 9. Radial density profiles of the stellar populations in the Milky Way disk, split by low- α (top) and high- α (bottom), stellar ages (panels, increasing left to right), and metallicity (line color). All profiles have been normalized to $\nu_* = 1$ at $R = 0$ for easier comparison between shapes. The uncertainties on each profile are shown in the error bars along the bottom of the plot.

Radial Profiles: The full radial profiles for each population are plotted in Figure 9 as radius vs stellar number density ν_* . The top set of panels show the profiles of the low- α populations, and the bottom set of panels shows the profiles of the high- α populations, with each panel therein corresponding to a different age and line color denoting metallicity. These profiles reflect the trends seen in the parameter results described above, including the sharply-peaked profiles of the young, low- α stars and the trend of break radius decreasing with metallicity.

The time-dependent evolution of the total radial density profile will be shown later in Section 5.6.

4.2. Vertical Density Profile

The derived best-fit parameters relating to the vertical mass density profile (Equation 12) are shown in Figure 10, which include the scale height at the solar neighborhood ($h_{z\odot}$; top panel) and the flaring parameter (A_{flare} ; bottom panel).

Scale Height: The scale height ($h_{z\odot}$) is significantly higher for the high- α population ($h_{z\odot} \sim 0.75$ kpc) compared to the low- α group ($h_{z\odot} \sim 0.25$ kpc). This is consistent with the known chemical bimodality in the disks, where the geometric thick disk is made primarily of older high- α and the thin disk is made of younger low- α populations (e.g., Gilmore & Reid 1983; Fuhrmann 1998; Bensby et al. 2005; Jurić et al. 2008).

In both the low- α population and high- α populations, the scale height ($h_{z\odot}$) increases with age and decreases with metallicity. Older and metal poor stars have a

higher scale height, although the low- α population is still thinner than the high- α populations everywhere.

Disk Flaring: The flaring term, (A_{flare}), determines the slope of the scale height as a function of radius $h_z(R)$. Like the scale height, the flaring parameter increases with both age and metallicity. The oldest, metal-poor populations are the most strongly flared whereas the young, metal-rich populations have a slope close to horizontal ($A_{flare} = 0$).

Vertical Profiles: A demonstration of the vertical density profile is shown in Figure 11 as the scale height as a function of galactic radius $h_z(R)$, a combination of the two vertical parameters $h_{z,\odot}$ and (A_{flare}) analogous to an edge-on view of the disk. The older, metal-poor populations have the largest scale height at R_\odot and the most vertical flaring. The high- α populations show stronger flaring than the low- α populations.

4.3. Surface Mass Density & Total Mass

The sixth and final parameter in our density model, ν_\odot , is the scaled amplitude of the profile or the stellar number density at R_\odot . This parameter is not fit as a free parameter in the MCMC chain, but rather calculated from the observed star counts as described in Equation 10 (Section 3.3). This is primarily used as the overall normalization factor in each profile (Equation 9), but can be converted into the surface mass density $\Sigma(R_\odot)$ and subsequently the total mass of each stellar population M_* by integrating over volume. Figure 12 presents these three quantities.

Stellar Number Density: The best-fit result of ν_\odot for each stellar population is shown in the top panels Figure 12. The stellar populations with the highest density are slightly higher than solar metallicity $[M/H] = 0.1$ dex, low- α , and young. This is consistent with other studies, that find stars near the Solar neighborhood tend to be slightly more metal-rich and younger than the Sun (e.g., Haywood et al. 2013; Mackreath et al. 2017; Miglio et al. 2021; Lian et al. 2022; Imig et al. 2023), and the low- α disk represents the majority of the mass at this radius. We find that the low- α thin disk comprises around 65% of the total stellar density at the solar location.

Surface Mass Density: The number density of the RGB sample (ν_*) can be converted into a surface mass density with a few additional steps. First, the number counts of the RGB stars are converted into mass of the total population using corrections from our isochrones (the PARSEC isochrones; Bressan et al. 2012; Chen et al. 2014) and assuming a Kroupa IMF (Kroupa 2002). In a younger population, a smaller number of massive stars populate the giant branch; In older populations, a

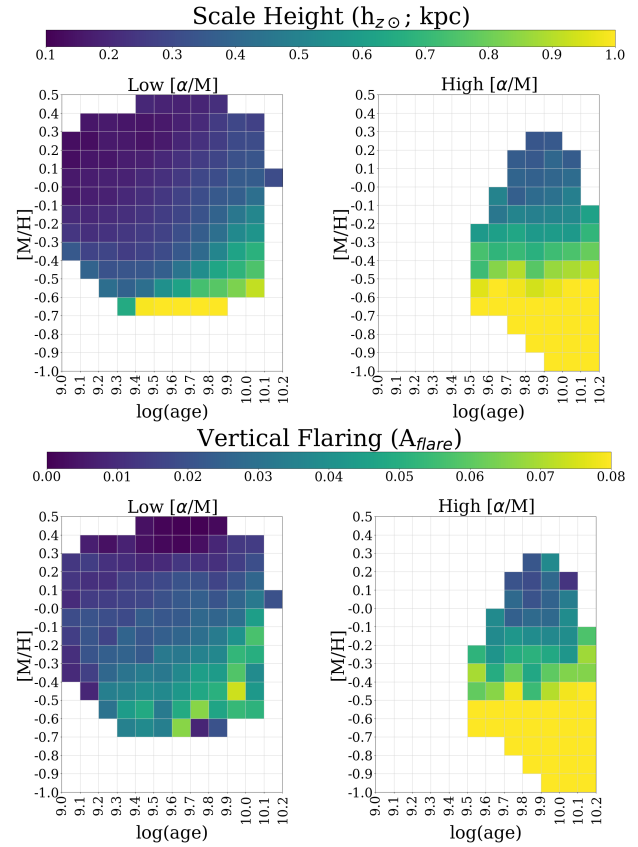


Figure 10. Vertical parameters best-fit results for our density profile, the scale height at the Solar radius $h_{z,\odot}$ and the flaring parameter A_{flare} , or the slope of h_z as a function of R . Each row is set up with the same grid layout as Figure 3 to show the trends across stellar populations: low- α (left) and high- α (right), split into corresponding bins of metallicity (rows) and stellar age (columns) in the grid. The color indicates the parameter value, with the noted values on the color scale. A white color indicates that there were not enough stars in that population bin to perform a fit.

higher number count of lower mass stars populates the giant branch. If two stellar populations have the same number density of RGB stars, they could have a significantly different mass density due to a difference in population age, thus the need for this correction. Then, the mass density ($M_\odot \text{ pc}^{-3}$) is converted into a surface mass density ($M_\odot \text{ pc}^{-2}$) by integrating all of our best-fit density profiles over height Z for a range of $|Z| \leq 5$ kpc. The resulting surface mass density estimations are shown in the middle panel of Figure 12. We measure a total surface mass density at the Solar radius of the low- α disk to be $18.7 M_\odot \text{ pc}^{-2}$ and the high- α disk as $22 M_\odot \text{ pc}^{-2}$, for a total local surface density of $40.6 M_\odot \text{ pc}^{-2}$. While the low- α disk contributes around 65% of the number density at the solar neighborhood, we find that it only contributes 46% of the local surface mass

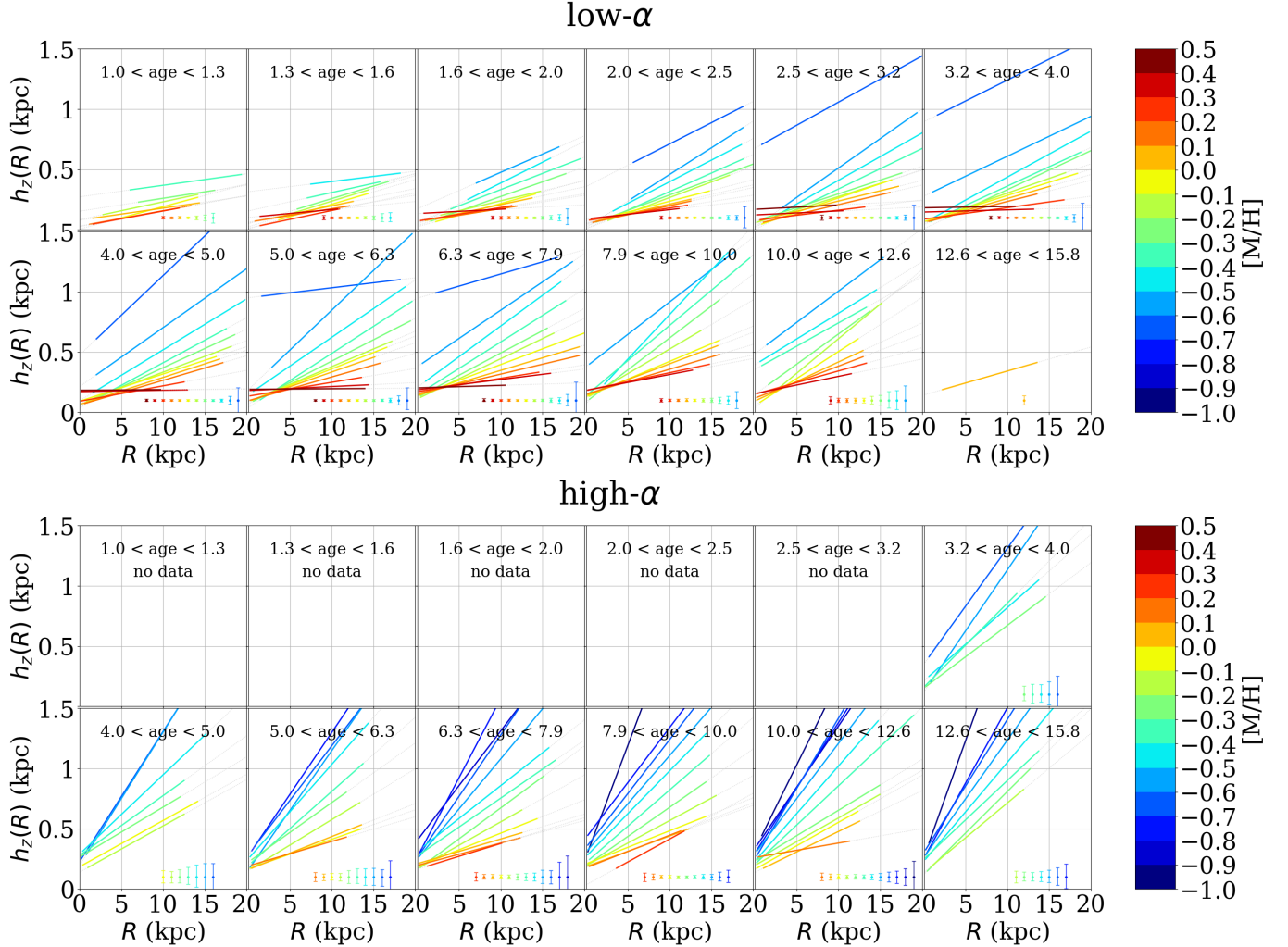


Figure 11. Vertical density profiles showing scale height h_z as a function of radius of the stellar populations in the Milky Way disk, split by low- α (top) and high- α (bottom), stellar ages (panels, increasing left to right), and metallicity (line color). The uncertainties on each profile are shown in the error bars along the bottom of the plot.

density due primarily to the increased scale height of the high- α disk.

Our estimate of $40.6 M_{\odot}$ is generally consistent with other studies. Bovy & Rix (2013) report a value of $38 \pm 4 M_{\odot} \text{ pc}^{-2}$. Mackereth et al. (2017) found a significantly smaller value of $20.1^{+2.4}_{-2.9} M_{\odot} \text{ pc}^{-2}$ and Lian et al. (2022) report $21.31 \pm 0.32 M_{\odot} \text{ pc}^{-2}$. The fractional contribution across the entire Galaxy between the surface mass density of the high- α and low- α disk varies between studies. Mackereth et al. (2017) report a value of $f_{\Sigma} = 18\%$, Lian et al. (2022) report a value of $f_{\Sigma} = 36\%$ and this work derives a comparatively larger ratio of 53%. This is likely due to our more complete sampling of the inner disk ($R \leq 3 \text{ kpc}$), where the high- α populations contribute the majority of the mass.

Total Mass: The total mass of each stellar population is calculated by integrating all of our density profiles over radius ($0 \leq R \leq 20 \text{ kpc}$) and height ($|Z| \leq 5$

kpc) with the mass correction from isochrones used previously. The mass contribution of each stellar population is shown in the bottom panel of Figure 12 and varies with age and metallicity. The trend with age is consistent with a declining star formation history, and the trend with metallicity can be explained by chemical enrichment; at younger ages, there is less pristine gas with which to form metal-poor stars, resulting in a larger fraction of each population being metal-rich at fixed age.

We measure the total mass of the disk to be $2.63 \times 10^{10} M_{\odot}$, with the low- α thin disk composing of 38% of that total. The thin disk contributes most of the mass near the solar neighborhood, but the high- α population contributes more at smaller radii due to its characteristically smaller scale lengths. Our total value of $2.63 \times 10^{10} M_{\odot}$ is lower than other estimates in literature, for ex-

ample $4.6 \times 10^{10} M_{\odot}$ (Bovy & Rix 2013), $3.8 \times 10^{10} M_{\odot}$ (Licquia & Newman 2016).

5. INTEGRATED PROPERTIES

Our view of the Milky Way is more detailed near the Solar vicinity due to obvious observational limitations, whereas the exponential density profile suggests that the majority of the mass in the Milky Way lies closer the Galactic center. Therefore a complete picture of our Galaxy has long been out of reach and obscured by dust, but our selection-function corrected density fits can offer insight on the integrated properties of the Milky Way.

In this section, we apply our results from Section 4 and sum the best fit density profiles together across all of the stellar population bins to portray the Milky Way in its entirety. This allows us to study the Milky Way in broader galactic context, comparing its density profile, scale length, star formation history, integrated spectrum, and photometric colors to other galaxies more directly for the first time. See Zasowski et al. (*in prep*) for some complementary analyses, including comparisons to simulated galaxies.

5.1. Total Mass Profile & Disk Scale Length

The characteristic scale length of the Milky Way disk is still uncertain, with estimates commonly ranging between 1.8 and 6 kpc (e.g., the review in Bland-Hawthorn & Gerhard 2016). Despite the large range of radius estimates for the MW, several studies suggest that the Milky Way is too small for its mass (e.g., Bovy & Rix 2013; Licquia & Newman 2016; Boardman et al. 2020), with a characteristic scale length shorter than the 2σ range of most of its galactic siblings, which generally fall in the $R_d = 3.2 - 5.7$ kpc range.

We obtain a total scale length measurement for the MW disk by summing the radial mass density profiles of every stellar population (Figure 9) together, integrating vertically over $|Z| \leq 5$ kpc and fitting for a single scale length of the total. The summed radial density profile is shown in the top panel of Figure 13. Although the individual stellar populations are best modeled by broken exponential profiles with a continuous range of r_{break} , the total profile mostly resembles a single exponential with a scale length of $R = 2.37$ kpc. The locations of the Milky Way's most prominent spiral arms from Reid et al. (2019) are also annotated on this figure, the inner Sag-Car arm (at $R \sim 6.04$ kpc) and the Norma-Outer arm (at $R \sim 12.24$ kpc), possibly explaining the excess in the profile at these locations. The density profile used (equations 9–12) is axisymmetric and independent of azimuthal angle θ , but because the APOGEE footprint (Figure 1) covers only a limited azimuthal range in the

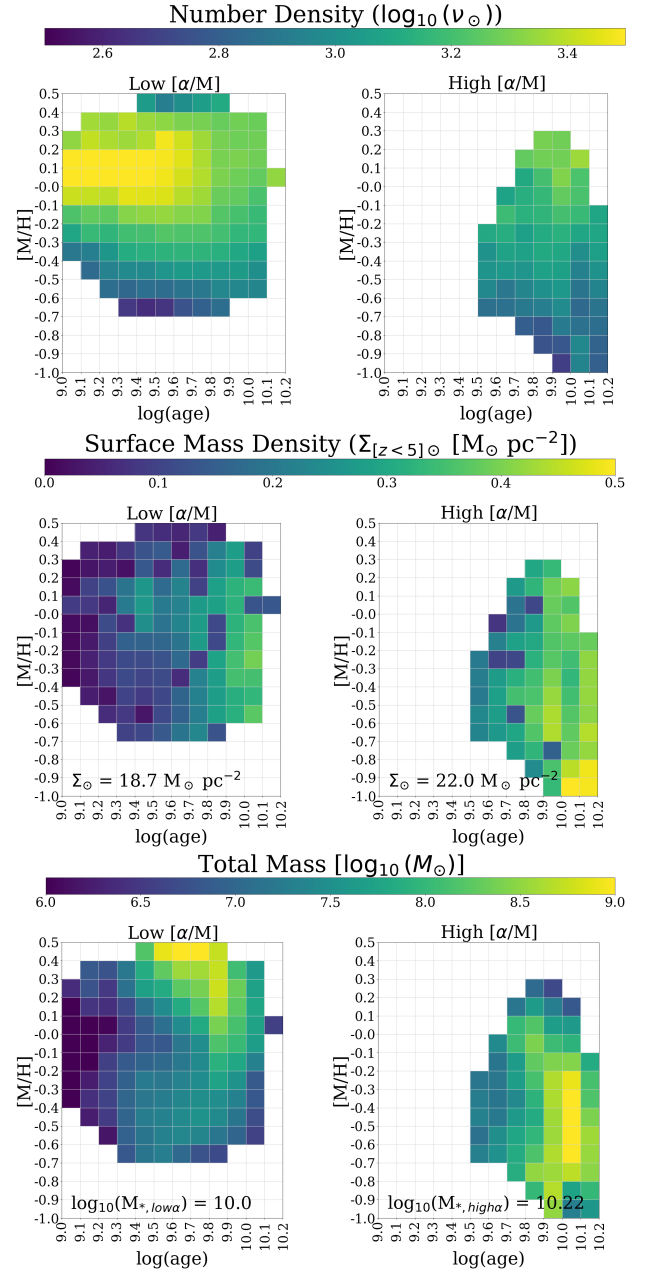


Figure 12. The mass parameter from our density profile, the number density at the Solar Neighborhood (v_{\odot} ; top), and the subsequent calculation of surface mass density (Σ_{odot} , middle) total mass contribution (M_* ; bottom) of each stellar population calculated by integrating the best-fit density profiles over space. Each row is set up with the same grid layout as Figure 3 to show the trends across stellar populations: low- α (left) and high- α (right), split into corresponding bins of metallicity (rows) and stellar age (columns) in the grid. The color indicates the parameter value, with the noted values on the color scale. A white color indicates that there were not enough stars in that population bin to perform a fit.

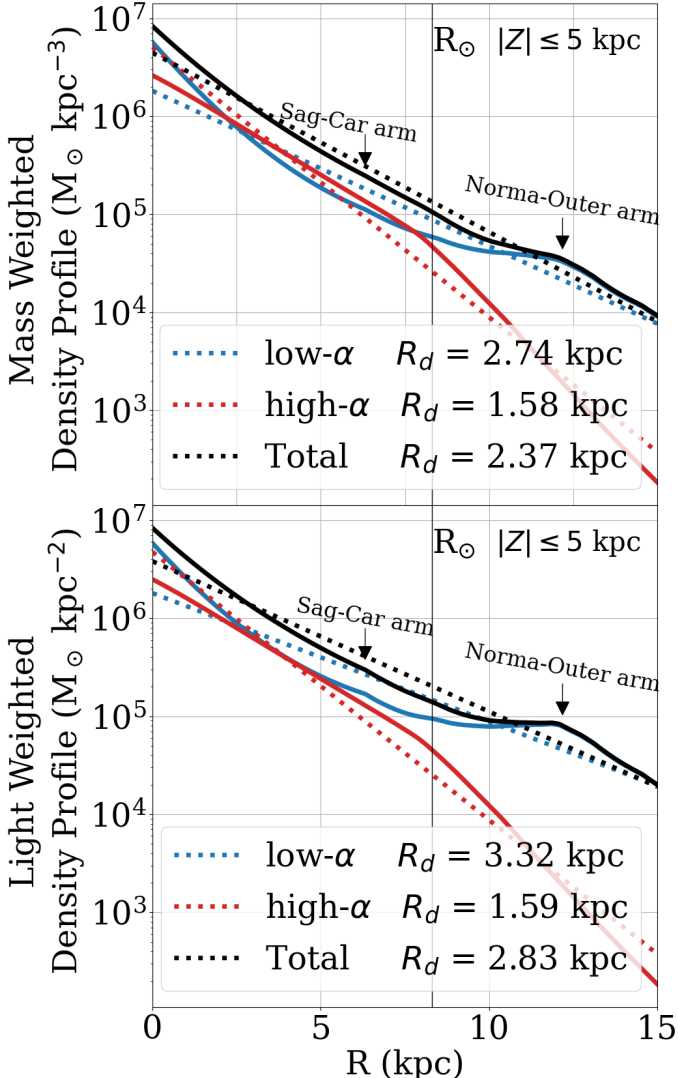


Figure 13. Total surface mass density profile of the Milky Way disk, in a mass-weighted (top) and light-weighted (bottom) profile. The high- α populations (red line), low- α populations (blue line), and total profile (black line) are plotted for each. For each, the solid line denotes the empirical profile from the sum of all mono-age, mono-abundance populations, and the dotted line is a straight-line fit for a single “total” scale length value for each α group, the value of which is noted in the legend.

Galaxy the spiral arms possibly emerge as “ring”-shapes structures extrapolated in our integrated fit.

The total high- α profile resembles a slightly broken exponential profile; we interpret this as the truncation of the thick disk near the Solar neighborhood ($R \sim 8$ kpc), consistent with the dearth of high- α stars observed beyond the Solar radius (e.g., Hayden et al. 2015). This is also close to the expected Outer Lindblad Resonance (OLR) of the Galactic Bar at $R \sim 9.4$ kpc (Halle et al. 2015; Michtchenko et al. 2016; Dias et al. 2019; Khopers-

kov et al. 2020b, e.g.), which may act as a boundary for radial migration past which no stars can migrate (e.g., Halle et al. 2015; Khoperskov et al. 2020a).

The total mass-weighted scale length of the disk measured this way is $R_d = 2.38 \pm 0.2$ kpc. This is fairly consistent with other literature measurements for the scale length of the total disk, which vary from $R_d = 2.15 \pm 0.14$ kpc (Bovy & Rix 2013), $R_d = 2.71 \pm 0.21$ kpc (Licquia & Newman 2016), $R_d = 2.48 \pm 0.14$ kpc (Fielder et al. 2021), and $R_d = 1.977 \pm 0.01$ kpc (Lian et al. 2022). Our estimate may be larger than some previous estimates due to our increased sampling of the outer disk ($R \geq 15$ kpc) with the final data release of APOGEE.

However, for comparison with external galaxies, one should consider the bolometric (in the SDSS bandpass) “light-weighted” integrated mass profile which we present in the bottom panel of Figure 13, with each stellar population weighted by its relative light contribution calculated from the MaStar SSP models (Maraston et al. 2020) over wavelength range $3622 - 10,354$ Å, such that the bright and young blue populations contribute more to the profile than the fainter, older, and redder stars. Notably, the total scale lengths measured from the light-weighted profile are larger than those from the mass-weighted profile, bringing the total scale length to $R_d = 2.83 \pm 0.2$ kpc. This increase suggests that part of the Milky Way’s apparent compactness may be explained by differences in the techniques used to measure the scale length of the Milky Way (typically through mass) and other galaxies (weighted by light), although it is still slightly smaller than the typical analog range of $R_d = 3.2 - 5.7$ kpc. The spiral arms of the Milky Way are also more apparent in this light-weighted profile.

The steep decrease in the total light-weighted surface mass density profile at $R \geq 13$ kpc could be interpreted as a truncation of the disk, like the sudden decrease in surface brightness observed in other disk galaxies (Freeman 1970; van der Kruit 1979). MW-like disk galaxies often have typical truncation radii of ~ 14 kpc (e.g., Martín-Navarro et al. 2012; Martínez-Lombilla et al. 2018; Díaz-García et al. 2022), thought to be linked with a critical gas density threshold for star formation.

5.2. Integrated Spectrum

The properties of other galaxies are often inferred through their integrated spectra, with large population statistics accessible through galaxy surveys including MaNGA (Bundy et al. 2015), CALIFA (Sánchez et al. 2016), and SAMI (Croom et al. 2021). Here, we estimate the integrated spectrum of the Milky Way and qualitatively compare it to analog galaxies.

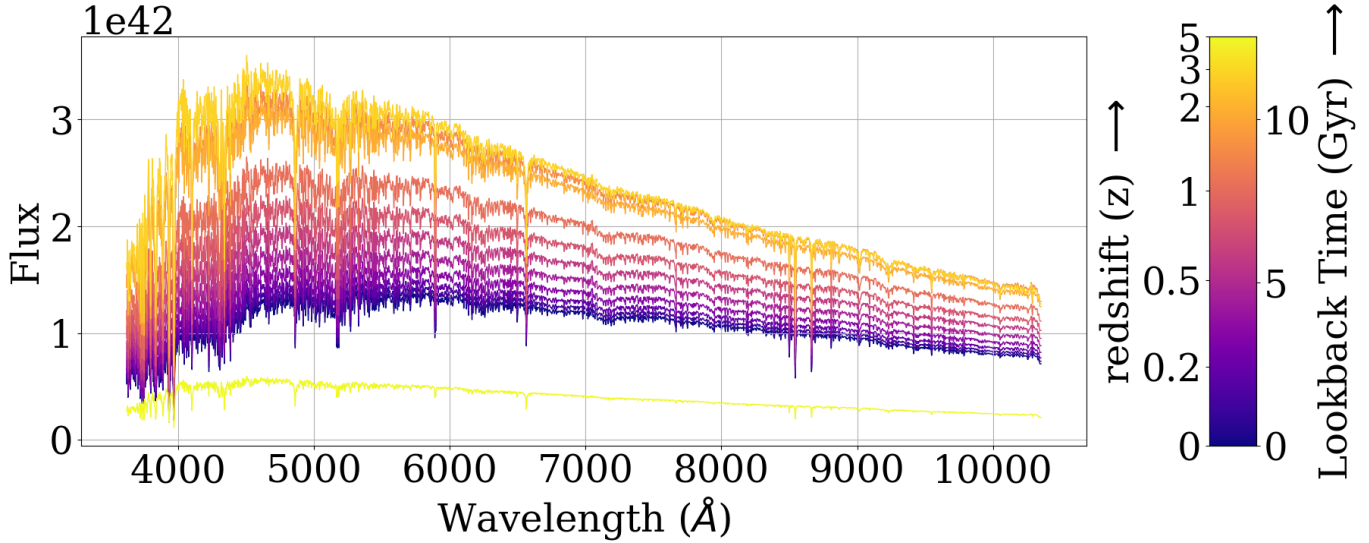


Figure 14. The integrated spectrum of the stellar populations of the Milky Way and its subsequent evolution over time, calculated from our mass estimates paired with the MaStar Simple Stellar Population spectra (Maraston et al. 2020).

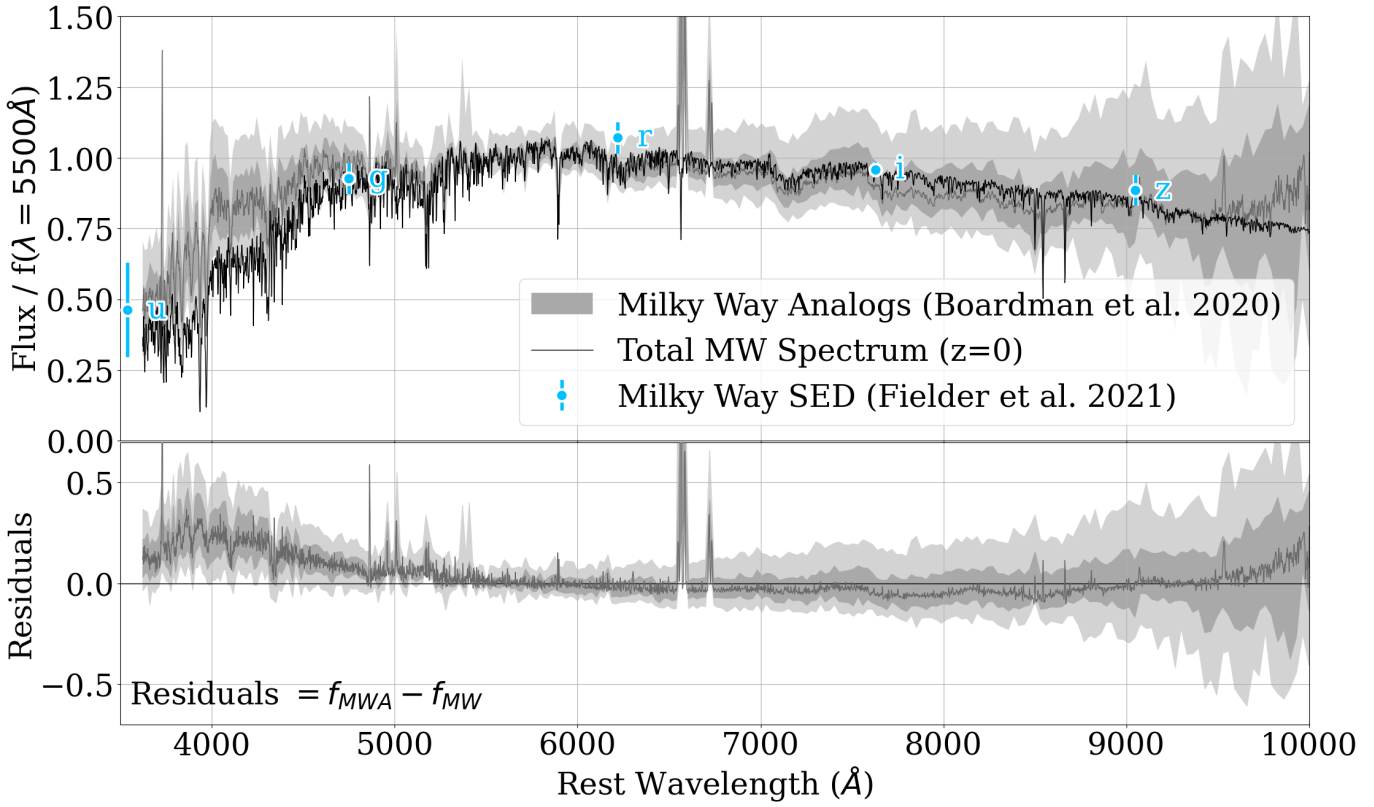


Figure 15. Top: Comparison between the present-day integrated spectrum of the Milky Way (black line), the median spectrum from the MW analog sample in MaNGA (Boardman et al. 2020, dark gray line, with shaded regions denoting $\pm 1\sigma$ and $\pm 2\sigma$ spread among the spectra) and estimates of the MW's SED from Gaussian process regression (Fielder et al. 2021, blue points). Bottom: Residuals comparing the median MWA spectrum to the spectrum of the MW.

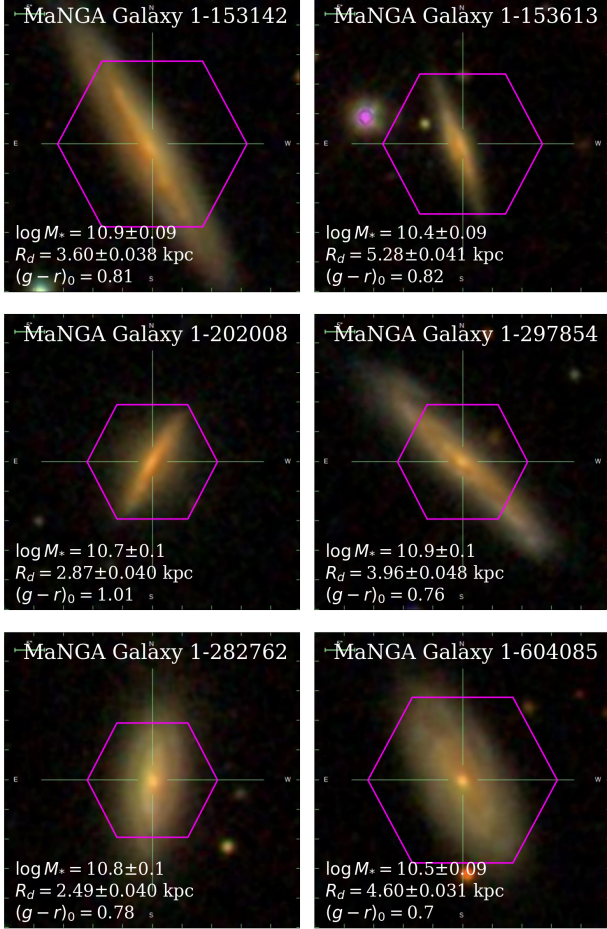


Figure 16. The six best Milky Way Analog galaxies in MaNGA determined by the similarity of their integrated spectra compared to the Milky Way spectrum in Figure 15. Selected properties for each galaxy, including stellar mass ($\log M_*$), disk scale length (R_d), and $(g-r)$ color are listed from the NASA-Sloan Atlas (Blanton et al. 2011).

Figure 14 shows the integrated stellar spectrum of the Milky Way and its evolution over time. The present-day ($z = 0$) spectrum was calculated using the empirical Simple Stellar Population (SSP) models from Maraston et al. (2020), and summing the corresponding SSP spectrum of each stellar population in our sample weighted by the total mass contribution for each population (Figure 12). The MaStar SSP spectra cover a wavelength range of $3,622 - 10,354 \text{ \AA}$, with resolution $R \sim 1800$, calculated using empirical spectra from the MaStar stellar library (Yan et al. 2019).

Tracking the Milky Way’s spectrum backwards through time involves the additional step of adjusting the snapshot age of our stellar populations to select the appropriate SSP model (i.e., the stellar population that is 6 Gyr old at present day would have been 1 Gyr old at a lookback time of 5 Gyr), and removing from the sum

all populations younger than the snapshot time, which had not been born yet.

The Milky Way’s stellar continuum reached peak brightness during our second oldest age bin ($8.6 \leq \text{age} \leq 10.7 \text{ Gyr}; z \approx 2$), and has been steadily declining over time while shifting redder in color: the flux in blue wavelengths decline more quickly than the redder wavelengths. Note that this represents only the pure stellar continuum for the Milky Way; no dust attenuation or gas emission is present in this spectrum.

For a more realistic comparison, we adjust the Milky Way’s spectrum for reddening using the extinction curve from Fitzpatrick et al. (2019) and a simple dust screen model. Specifically, we adopt the curve corresponding to $R(V) = 3.1$, which they report as the typical value for the diffuse Milky Way environment. We adjust half of the light for reddening with $A_V = 1$, and keep the other half of the light in its original state in an oversimplified approximation of a face-on disk with a screen layer of dust in the mid plane.

Figure 15 compares the reddened spectrum at present day ($z = 0$) to the estimated Milky Way SED constraints from Fielder et al. (2021) (blue points) and a selection of 62 Milky Way Analog (MWA) galaxies in MaNGA from Boardman et al. (2020). Every spectrum has been normalized such that the flux at 5500\AA is equal to 1, for direct comparison on the same scale.

The Milky Way SED from Fielder et al. (2021) was derived using Gaussian process regression on a large galaxy sample spanning GALEX, SDSS, 2MASS, and WISE coverage to predict the photometric properties of the Milky Way. We adopt the values for the optical Sloan $ugriz$ flux values (Fielder et al. 2021, Table 1), plotted as the blue points with corresponding error bars on Figure 15. This predicted SED matches our present-day Milky Way spectrum well, falling within the 1σ range for all 5 passbands.

The MaNGA MW Analog (MWA) sample from Boardman et al. (2020) consists of 62 galaxies selected by stellar mass ($4.6 \leq M_* \leq 7.2 \times 10^{10} M_\odot$) and bulge-to-total mass ratio ($0.13 \leq B/T \leq 0.19$), i.e., their “bulge analog” subsample. For each MaNGA MWA, we constructed a single stacked spectrum by stacking spaxel spectra within 1.5 half-light radii (R_e). MaNGA galaxies are typically observed out to at least $1.5 R_e$, though certain MWAs were observed out to less than this, as detailed in Boardman et al. (2020). We obtain spaxels’ galactocentric radii from the MaNGA data analysis pipeline (DAP; Belfiore et al. 2019; Westfall et al. 2019), which uses for R_e the elliptical Petrosian half-light radius in the SDSS r-band. Prior to performing stacking, we masked out spaxels with DAP quality flags NOCOV (no

coverage), LOWCOV (low coverage), DEADFIBER, FORESTAR (foreground star) or DONOTUSE.

The observed wavelengths for each MWA spectrum have been shifted to rest-frame using the redshift reported in the MaNGA `dr` catalog. The maximum redshift galaxy in this sample has $z = 0.079$. The median flux at each wavelength across all 62 galaxies (the “typical” spectrum for a MWA) is plotted as the dark gray line in Figure 15, with the $\pm 1\sigma$ and $\pm 2\sigma$ range in the sample as the medium gray and light gray ranges respectively. The bottom panel shows the residual differences between the MW spectrum and the MWA sample. Our Milky Way spectrum matches the MWA sample reasonably well, falling within the $\pm 2\sigma$ at all but the bluest wavelengths ($\lambda \leq 5000 \text{ \AA}$). There is more variation within the MWA sample at red wavelengths than blue. The MW spectrum deviates most from the MWA sample at blue wavelengths ($\lambda \leq 5000 \text{ \AA}$), which is consistent with the fact that most of the MWAs are less massive than the Milky Way, and possibly amplified by the simplified prescription for dust extinction included in our spectrum.

Out of the 62 galaxies in the MWA sample, the six closest matches to the Milky Way’s integrated spectrum (determined via a χ^2 calculation) are shown in Figure 16. Morphologically, they all resemble spiral galaxies with red colors, supporting the idea that the Milky Way belongs to the “red spiral” category of galaxies (e.g., Licquia et al. 2015; Fielder et al. 2021). Red spirals are characterized by their red optical colors generally comparable to early-type galaxies, and are often massive galaxies that feature a prominent bar (Masters et al. 2010).

The un-reddened MW spectrum at different lookback times (shown in Figure 14) is available for download as a fits table⁶. Each row in the table contains the wavelength and flux, the corresponding properties such as lookback time, redshift, and stellar mass, and the measured properties from each spectrum including ($g - r$) color and selected spectral indices (Section 5.3).

5.3. Spectral Line Indices

Spectral line indices can be a useful tool for measuring the strength of absorption lines in a galaxy’s spectrum, and are known to be correlated with stellar population properties such as age and metallicity (e.g., Burstein et al. 1984; Worthey 1994; Worthey & Ottaviani 1997; Trager et al. 1998). In Table 3, we report measurements of several absorption line indices for our present-

day Milky Way spectrum in Figure 14 measured using the publicly available MaNGA Data Analysis Pipeline (DAP⁷; Westfall et al. 2019). As index measurements are independent of stellar continuum, the un-reddened spectrum was used for these measurements. The indices were measured using the `AbsorptionLineIndices` class and the waveband definitions provided in the MaNGA DAP (Westfall et al. 2019, see their Table 4), which concatenates index definitions from a variety of literature (Trager et al. 1998; Worthey & Ottaviani 1997; Serven et al. 2005; Cenarro et al. 2001; Conroy & van Dokkum 2012; Spinello et al. 2012, 2014; La Barbera et al. 2013). The index measurement \mathcal{I} is defined as:

$$\mathcal{I} = \begin{cases} S(1 - f/C) & \text{for angstrom units} \\ -2.5 \log[\langle f/C \rangle] & \text{for magnitude units} \end{cases} \quad (13)$$

where f is the spectrum flux density, C is the linear continuum approximation defined using two side bands (“blue” and “red”), and S is a discrete sum over wavelength (Westfall et al. 2019, their equations 8, 11, 22).

Selected index measurements for the present-day MW spectrum are presented in Table 3, and the full table is available for download with the spectra as described at the end of Section 5.2.

One such application of the spectral index measurements is plotted in Figure 17, showing the relationship between an α -element index (MgB) and the average iron index ($\langle \text{Fe} \rangle = (\text{Fe}5270 + \text{Fe}5335)/2$). This relation can be used to investigate the overall α -enhancement of a galaxy, which is generally linked to star formation efficiency, and how it compares to other galaxies as a function of stellar mass (e.g., Thomas et al. 2005; Fraser-McKelvie et al. 2018). In Figure 17, our MW spectrum is plotted as the star point, the MW analog sample is plotted as the large circles, and the broader MaNGA sample as small circles. Index measurements for the MaNGA galaxies are retrieved from the `SPECINDEX_1RE` column of the MaNGA Data Analysis Pipeline catalog, which provides the median index measurement across all spaxels within one effective radius for each galaxy. Reference values from the SSP models of Thomas et al. (2011) are overplotted as the grid lines for a population of age 10 Gyr.

Based on these measurements, the Milky Way appears both more metal-rich and more α -enhanced than most of its peers. However, as with many of our results, the metallicity limit of $[\text{M}/\text{H}] \geq -0.7$ for low- α stars in our sample may bias these results.

⁶ https://github.com/astrojimig/mw_density_imig2025/mw_spectrum.fits

⁷ <https://sdss-mangadap.readthedocs.io/>

Index	λ Window (Å)	Units	Measurement
CN1	4143.3-4178.3	mag	0.02
CN2	4143.3-4178.3	mag	0.06
Ca4227	4223.4-4235.9	Å	1.43
G4300	4282.6-4317.6	Å	5.16
Fe4383	4370.4-4421.6	Å	4.7
Ca4455	4453.4-4475.9	Å	1.53
Fe4531	4515.5-4560.5	Å	3.56
C24668	4635.3-4721.6	Å	4.13
Hb	4849.2-4878.0	Å	2.07
Fe5015	4979.1-5055.4	Å	5.59
Mg1	5070.5-5135.6	mag	0.07
Mg2	5155.6-5198.1	mag	0.19
Mgb	5161.6-5194.1	Å	3.14
Fe5270	5247.1-5287.1	Å	2.88
Fe5335	5313.6-5353.6	Å	2.73
Fe5406	5389.0-5416.5	Å	1.81
Fe5709	5698.2-5722.0	Å	1.03
Fe5782	5778.2-5798.2	Å	0.84
NaD	5878.5-5911.0	Å	2.8
TiO1	5938.3-5995.8	mag	0.03
TiO2	6191.3-6273.9	mag	0.06
HDeltaA	4084.7-4123.4	Å	-1.49
HGammaA	4321.0-4364.7	Å	-4.29
HDeltaF	4092.2-4113.4	Å	0.68
HGammaF	4332.5-4353.5	Å	-0.66
CaHK	3900.6-4004.6	Å	18.29
CaII1	8486.3-8515.3	Å	1.34
CaII2	8524.3-8564.4	Å	3.48
CaII3	8644.4-8684.4	Å	2.87
Pa17	8463.3-8476.3	Å	0.28
Pa14	8579.4-8621.4	Å	0.36
Pa12	8732.4-8774.4	Å	0.42
MgICvD	5165.0-5220.0	Å	5.09
NaICvD	8177.0-8205.0	Å	0.47
MgIIR	8801.9-8816.9	Å	0.67
FeHCvD	9905.0-9935.0	Å	0.4
NaI	8170.7-8236.4	Å	1.0
bTiO	4759.8-4801.3	mag	0.02
aTiO	5446.5-5601.6	mag	0.01
CaH1	6359.3-6403.5	mag	0.0
CaH2	6776.9-6901.9	mag	0.02
NaISDSS	8182.2-8202.3	Å	0.61
TiO2SDSS	6191.3-6273.9	mag	0.06

Table 3. Selected spectral absorption line index measurements for the present-day Milky Way integrated spectrum in Figure 14. The full collection of index measurements is available for download with the spectra as described at the end of Section 5.2.

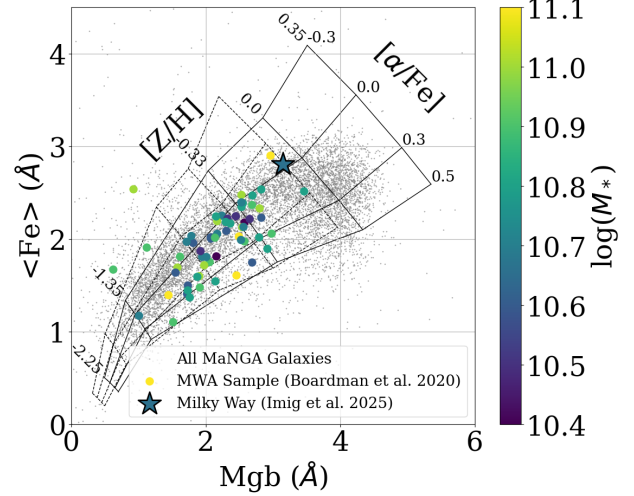


Figure 17. Spectral Line Indices Mgb and $<\text{Fe}> = (\text{Fe}5270 + \text{Fe}5335)/2$ for the present-day Milky Way spectrum (star point), the MWA sample (large circles; Boardman et al. 2020), and the entire MaNGA sample (gray dots; Westfall et al. 2019). Reference values from the SSP models of Thomas et al. (2011) are overplotted as the grid lines for a population of age 10 Gyr (solid lines) and 1 Gyr (dashed lines).

5.4. Galaxy Color-Mass Diagram

The photometric colors of the Milky Way are impossible to observe directly from our inside perspective, and have historically only been estimated using analog galaxies or machine learning models (Mutch et al. 2011; Licquia et al. 2015; Fielder et al. 2021). The general consensus from these studies is that the Milky Way falls in the relatively underpopulated “green valley” region of the optical Galaxy Color-Mass Diagram, thought to be short-lived transition state as a galaxy evolves from the Blue Cloud onto the Red Sequence (Strateva et al. 2001; Baldry et al. 2004).

Using the integrated spectra of the Milky Way in Figure 14, reddened with the extinction law from Fitzpatrick et al. (2019), we can measure the evolution of the observed $(g - r)$ color of the Milky Way over time. The $(g - r)$ color is computed from the spectrum using:

$$g = -2.5 \log_{10} \left(\frac{\int \lambda f_\lambda R_g d\lambda}{\int \lambda f_{AB} R_g d\lambda} \right) \quad (14)$$

$$r = -2.5 \log_{10} \left(\frac{\int \lambda f_\lambda R_r d\lambda}{\int \lambda f_{AB} R_r d\lambda} \right) \quad (15)$$

where f_λ is the flux of our MW integrated spectrum for each wavelength λ , and the filter response curves R_g and R_r are retrieved from Doi et al. (2010) for the g and r SDSS photometric filters, respectively. The reference value f_{AB} is defined in the AB photometric system as

a constant source $f_\nu = 3631$ Jy such that $f_{AB} \propto f_\nu/\lambda$ (e.g., Oke & Gunn 1983; Blanton & Roweis 2007).

In Figure 18, we use this calculation to plot the evolution of the Milky Way on the galaxy color-mass diagram. The highlighted “green valley” region is adopted from the definition set in Mendel et al. (2013), corresponding to boundary lines of $(g - r)_0 = 0.6 + 0.06(\log(M_*) - 10)$ and $(g - r)_0 = 0.6 + 0.06(\log(M_*) - 10) + 0.1$. The gray background points are the full sample of MaNGA galaxies; the colors and masses for the MaNGA galaxies are adopted from the NASA-Sloan Atlas catalog (NSA; Blanton et al. 2011), taken from the columns `NSA_SERSIC_ABSMAG` and `NSA_SERSIC_MASS` from the MaNGA `drpall` catalog.

Previous estimates of the Milky Way’s present-day color (Licquia et al. 2015; Fielder et al. 2021) are plotted for comparison as square points. Fielder et al. (2021) estimated the color of the present-day Milky Way to be $(g - r) = 0.668 \pm 0.05$ (green square point), and Licquia et al. (2015) reported a value of $(g - r) = 0.682 \pm 0.061$ (cyan square point). We measure a present-day color of $(g - r) = 0.69^{+0.01}_{-0.03}$, consistent with the prior estimates.

The MaNGA sample of Milky Way Analogs from Boardman et al. (2020) are highlighted as the larger black points in the background. The MWA sample contains a wide variety of colors from $0.46 \leq (g - r) \leq 1.0$, and 33 out of 62 galaxies (55%) fall within the green valley.

Unique to our method, the time evolution of the Milky Way’s observed colors can be traced backwards in time using the ages of our different stellar populations and corresponding snapshot spectrum in Section 5.2. The galaxy color-mass bimodality has been observed up to a redshift of $z = 1.1$ (Bell et al. 2004; Weiner et al. 2005), although the sequence has been observed to evolve with redshift. Approaching present-day, the density peak of each population transitions to redder colors, consistent with the aging of stellar populations, and the relative number fraction of red sequence to blue cloud galaxies increases, suggesting that galaxies evolve from one state to the other over time through different possible quenching processes, passing through the green valley in the interim (Salim et al. 2007; Schawinski et al. 2014; Smethurst et al. 2015).

The time evolution of the MW’s $(g - r)$ color is shown in Figure 18 as the star points, transitioning from present day (purple) to our oldest stellar age bin (yellow). As before, each snapshot follows our stellar age bins, meaning they are logarithmically spaced in bins of $\Delta \log(\text{Age}) = 0.1$. The mass evolution with time is taken from our parameter results presented in Section 4.3. Our oldest snapshot (yellow point) lies in the blue cloud, and

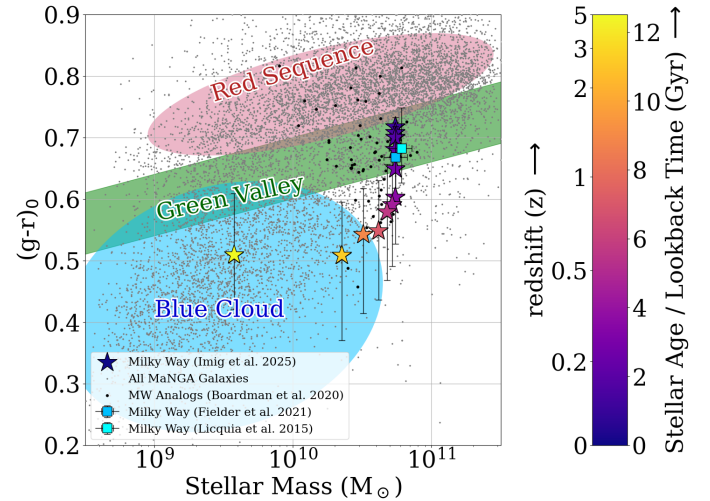


Figure 18. Galaxy color-mass diagram. The Milky Way’s $(g - r)$ color and stellar mass M_* are plotted as the star-shaped points, with their evolution over time (point color). Previous studies that have estimated the Milky Way’s optical colors through observing Milky Way Analog galaxies, including Fielder et al. (2021) (green square) and Licquia et al. (2015) (cyan square) are plotted for reference. The boundaries of the highlighted “green valley” zone are adopted from Mendel et al. (2013). The full MaNGA galaxy sample (gray points; Bundy et al. 2015) and the Milky Way Analog sample (black points; Boardman et al. 2020) are plotted with their reported mass and color estimates from the NASA-Sloan Atlas (Blanton et al. 2011).

as time increases (decreasing redshift), the Galaxy gains stellar mass and shifts redder in color. This is consistent with the evolution of this diagram observed at different redshifts (Bell et al. 2004; Weiner et al. 2005). In our results, the MW has only been in the green valley for the last ≈ 3 Gyr. A comparable figure is shown in Zasowski et al. (*in prep*), using isochrone-based integrated magnitudes, and leads to very similar conclusions.

We note that the simple reddening approximation described previously does not evolve with time when used here. The dust content in a galaxy does vary significantly over time (e.g., Galliano et al. 2021), so our color estimates for older snapshots should be regarded as an upper limit.

Table 4 presents the Milky Way’s stellar mass and color as a function of time used in Figure 18.

5.5. Total Star Formation History

Earlier in Section 4.3, we present the derived mass contribution from each stellar population in our sample as a function of age, metallicity, and α -element abundances summed over the whole Galactic disk. This can easily be displayed as a star formation history by sum-

log(age)	redshift (z)	$(g - r)$	$M_*(\times 10^{10} M_\odot)$
9.0	0.0	$0.72^{+0.02}_{-0.01}$	5.48 ± 0.9
9.2	0.12	$0.71^{+0.02}_{-0.0}$	5.48 ± 0.9
9.2	0.15	$0.7^{+0.02}_{-0.0}$	5.48 ± 0.9
9.4	0.18	$0.68^{+0.03}_{-0.02}$	5.48 ± 0.9
9.4	0.24	$0.65^{+0.04}_{-0.04}$	5.48 ± 0.9
9.5	0.33	$0.6^{+0.08}_{-0.08}$	5.48 ± 0.9
9.6	0.43	$0.59^{+0.09}_{-0.1}$	5.21 ± 0.86
9.7	0.6	$0.58^{+0.08}_{-0.11}$	4.77 ± 0.78
9.8	0.87	$0.55^{+0.08}_{-0.11}$	4.15 ± 0.68
9.9	1.43	$0.54^{+0.07}_{-0.13}$	3.22 ± 0.53
10.0	2.73	$0.51^{+0.09}_{-0.14}$	2.26 ± 0.37
10.1	5.0	$0.51^{+0.08}_{-0.09}$	0.38 ± 0.06

Table 4. Evolution of the Milky Way’s $(g - r)$ color and total stellar mass over time from Figure 18.

ming over the bins in metallicity, resulting in the mass contribution as a function of only stellar age.

The star formation history of the Milky Way is shown in Figure 19, split into the high- α population (red line), the low- α population (blue line) and the total population (black line) as mass contribution over time (see Zasowski et al. (*in prep*) for a similar figure split by Galactic radius). By the end of our oldest age bin (age ≥ 10.7 Gyr), the Milky Way had only assembled a small fraction of its mass of $3.06 \pm 0.25 \times 10^7 M_\odot$. Within the first 3 Gyr of the Universe, it had assembled round 20% of its current-dat mass, the majority of this being high- α stars. The total star formation rate declines over time.

The high- α stars were formed early on during an efficient burst and quickly declining star formation rate, whereas the low- α population formed more steadily over time peaking ~ 6 Gyr ago. This has been observed before in the Milky Way (e.g., Haywood et al. 2013; Fantin et al. 2019), and is similar to the characteristic star formation history of simulated EAGLE galaxies that show chemical bimodality at present day, generally ignited by an infall of gas from a merger event kick starting the formation of the low- α population (Mackereth et al. 2018). These galaxies represent only 5% of the total population at Milky Way comparable masses, implying that the chemical bimodality may be a rare phenomenon.

We observe significant age overlap between the low- α and high- α star formation history, which has been documented before (e.g., Haywood et al. 2013; Hayden et al. 2017; Aguirre et al. 2018; Gent et al. 2022; Imig et al. 2023). This scenario implies that the the low- α disk started forming stars while the high- α disk was still developing in different places in the Galaxy, although the age uncertainties contribute to this overlap.

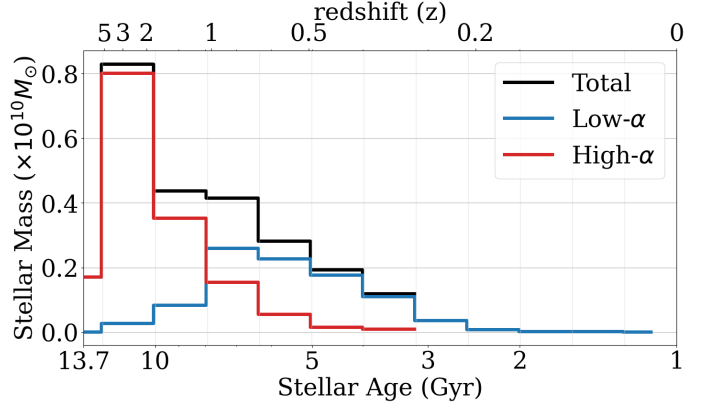


Figure 19. The star formation history of the Milky Way, for the high- α population (red line), low- α population (blue line) and total population (black line) calculated from our total mass results and summed over all stellar metallicities.

There is no meaningful way to discriminate between stars formed *in situ* and accreted populations in this figure, as it is all based on the present-day data and we made no orbital selection cuts to our sample. The fraction of *ex situ* stars in the disk is expected to be minimal; while accreted populations represent up to 30% of the mass in the Galactic halo (e.g., Bonaca et al. 2017; Mackereth & Bovy 2020), the fraction drops to less than 5% in the disk (e.g., Hawkins et al. 2015; Boecker et al. 2022; Conroy et al. 2022).

Our star formation history is generally skewed to more recent epochs than previous results. Using globular clusters, (Kruijssen et al. 2019) estimated that the Milky Way assembled 25% of its mass by $z = 3$ and 50% by $z = 1.5$, which is consistent with our estimates of 12% and 23% respectively. Bernard et al. (2018) used HST photometry and a CMD-fitting technique to measure the star formation rate of the central Milky Way, and report that 80% of the stars formed prior to 8 Gyr ago. This is larger than our estimate of 63% of its total mass before 8 Gyr, but consistent given the fact that their analysis only focused on the central Galaxy while ours is integrated over the entire disk. They find only 10% of stars are younger than 5 Gyr, compared to 21% from our results.

Comparison to extragalactic populations may help explain some of these discrepancies. The presence of a strong bar, like that which is seen in the Milky Way, is often linked to a lower star formation rate and early quenching of star formation in nearby spiral galaxies (Fraser-McKelvie et al. 2019, 2020) Following this trend, the Milky Way would be expected to have a lower star formation rate than its peers of similar mass.

5.6. Evolution with time

Figure 20. An animation showing the time evolution of the density structure of the Milky Way disk. The density structure is represented by the colors in the left panel as a face-on view ($X - Y$ plane; top) and edge on view ($R - Z$ plane, bottom) of the disk. The location of the Sun is marked by the solar symbol (\odot) and the center of the Galaxy is marked by the plus sign (+). Strictly for visual interest, Robert Hurt’s (SSC/Caltech) artistic rendition of the present-day Milky Way is overplotted to visualize the Milky Way’s bar and spiral arms. The star formation history is shown in the top-right panel as a timeline for the animation. The integrated spectrum of the high- α population (red line), low- α population (blue line), and total disk (black line) is shown on the bottom-right. Note: If this animated figure is not displaying properly in your pdf reader, this figure is also available online at: https://github.com/astrojimig/mw_density_imig2025/figures/mw_model.gif.

The total evolution of the Milky Way’s density profile, combined with the star formation history, is shown in an animation in Figure 20.

The inside-out growth of the Galactic disk is obvious, as the scale length starts small and grows over time. In the edge-on view, the juxtaposition of the thin and thick disk shows how the thick disk dominated the Milky Way’s mass at early times, but the thin disk grows as time progresses. At present-day, the thick disk only extends to $R \sim 9$ kpc, characterized by a smaller scale length than the thin disk.

The integrated spectrum reaches peak brightness in the second snapshot, $t = 4.3$ Gyr after the Big Bang. For most of the Galaxy’s history, the high- α population dominates the Milky Way’s light, until the most recent ~ 3 Gyrs when the low- α stars begin to contribute more of the light as the high- α stars evolve and die.

Although this visualization aims to represent the Milky Way’s evolution over time, we emphasize that this is still only a reflection of the present-day disk. This visualization does not account for the movement and

redistribution of stars, through processes like radial migration or dynamical heating, that may shape the disk over time.

6. DISCUSSION

6.1. Comparison with previous studies

Our derived structural parameters from Section 4 are generally consistent with previous studies, although the larger sample size and improved spatial sampling of the disk in our data is expected to improve the precision of the structural parameter estimates and better constrain the profile particularly in the inner Galaxy ($R \leq 3$ kpc) and outer Galaxy ($R \geq 15$ kpc) regions.

Consistent with our findings, Bovy et al. (2016b); Mackereth et al. (2017); Yu et al. (2021); Lian et al. (2022) all find that the high- α thick disk stars are generally well fit by a single exponential, while the low- α stars tend to have a broken exponential profile. The peak radius of the break is a function of metallicity, with metal-rich populations peaking earlier at ~ 7 kpc and metal-poor populations peaking later at ~ 12 kpc, re-

flecting the inside-out growth of the disk and subsequent metallicity gradient. The scale height of the high- α population is larger than the low- α populations.

We find that the vertical flaring parameter, A_{flare} is strongest in the old high- α stars. This is firstly consistent with the model predictions made by Minchev et al. (2015), who showed that flaring of mono-age populations is unavoidable in the cosmological context and increases for older ages. Observationally, this is consistent with the recent results of Yu et al. (2021) and Lian et al. (2022), and the older models of Minchev et al. (2015), but in conflict with older studies who report the strongest flaring in the low- α disk and little to no flaring in the high- α populations (e.g., Bovy et al. 2016b; Mackereth et al. 2017). This apparent tension is plausibly caused by the difference in spatial sampling between the different data sets. The sixteenth data release of APOGEE in 2019 (Jönsson et al. 2020) included the first data from the southern hemisphere APOGEE-S survey, which significantly increased the spatial sampling towards the Galactic center. The older APOGEE samples from Bovy et al. (2016b) ranges $4 \leq R \leq 15$ kpc and Mackereth et al. (2017) ranges $3 \leq R \leq 15$ kpc, both missing the crucial parts of the inner galaxy where the high- α disk dominates the mass. Our estimates of scale height h_Z agree with both of these studies within that radial range, but the trends in the flaring parameter A_{flare} differ. Bovy et al. (2016b) notably do not include stellar ages in their analysis, while Mackereth et al. (2017) includes ages but had a significantly smaller stellar sample overall. This work and Lian et al. (2022) include APOGEE-S data in the analysis. Yu et al. (2021) uses a red clump sample from the LAMOST survey, which although is also limited in radial distribution in the inner disk ($5 \leq R \leq 20$ kpc) has an overall larger sample size than Bovy et al. (2016b) and Mackereth et al. (2017). The flaring trends seen in this work, Yu et al. (2021), Lian et al. (2022), where the high- α mono-age populations flare most strongly, are all consistent with the models presented in Minchev et al. (2015), attributing the disk flaring in mono-age populations to the natural inside-out growth of the Galaxy.

We note that Bovy et al. (2016b), Yu et al. (2021) and Lian et al. (2022) do not use stellar ages in their analysis, and only groups stars by metallicity and α -element abundances; our analysis is most similar to Mackereth et al. (2017) in that aspect. While age is known to be correlated with α -element abundances and high- α stars are generally older, the age- α relation varies significantly over galactic position (e.g., Aguirre et al. 2018; Feuillet et al. 2018; Vázquez et al. 2022) and for most populations mono- α does not correspond to mono-age due to

the radial dependence on chemical evolution in the disk (Minchev et al. 2017).

Our trends with age are similar to that of Mackereth et al. (2017). The scale height increases with age for both populations. The break radius, R_{break} only depends on metallicity and is largely independent of stellar age. The difference between the inner disk scale length and outer disk scale length, a measure of how sharp the break is, correlates well with stellar age and little to no correlation with metallicity, with the most sharply peaked being the youngest populations.

In Section 4.3, our total surface mass density measured at the Solar neighborhood is $40.6 \pm 6.4 M_\odot \text{ pc}^{-2}$, and is generally consistent with other studies. Bovy & Rix (2013) report a value of $38 \pm 4 M_\odot \text{ pc}^{-2}$. Mackereth et al. (2017) found a significantly smaller value of $20.1^{+2.4}_{-2.9} M_\odot \text{ pc}^{-2}$ and Lian et al. (2022) report $21.31 \pm 0.32 M_\odot \text{ pc}^{-2}$. The fractional contribution across the entire Galaxy between the surface mass density of the high- α and low- α disk varies between studies. Mackereth et al. (2017) report a value of $f_\Sigma = 18\%$, Lian et al. (2022) report a value of $f_\Sigma = 36\%$ and this work derives a comparatively larger ratio of 53%. This is likely due to our more complete sampling of the inner disk ($R \leq 3$ kpc), where the high- α populations contribute the majority of the mass.

The present-day ($g - r$) color of the Milky Way is $(g - r) = 0.72^{+0.02}_{-0.01}$ by our methods in Section 5.4 (Figure 18). Using a sample of Milky Way analogs from SDSS defined by mass and star formation rates, Licquia et al. (2015) estimate a color of $(g - r) = 0.682 \pm 0.061$. Fielder et al. (2021) employed machine learning techniques on a large galaxy sample spanning GALEX, SDSS, 2MASS, and WISE catalogs to predict a value of $(g - r) = 0.668 \pm 0.05$ for the Milky Way. The color measurements in this study are unique in that they are driven by the stellar populations of the Milky Way itself, rather than using analog galaxies; despite the different approaches, all of these values are consistent.

6.2. Implications for the formation of the MW

By binning stars by metallicity ([M/H]), α -element abundances ([α /M]), and stellar age, we have split the Milky Way disk into its component stellar populations and explored how its structural parameters and integrated properties vary over time and by chemical abundance.

The implications for how the Milky Way disk formed and evolved are revealed within these trends. For any of the parameter results, trends with stellar age, metallicity, and α -element abundances can have different implications for the formation and evolution of the Milky

Way. A trend in stellar age suggests an underlying process that evolves with time, such as a dynamical heating, stellar migration, gas inflows or outflows, or ongoing chemical enrichment. A correlation with chemical abundances, on the other hand, could imply a more intrinsic property of the disk and that the population was “born that way” - although chemistry is certainly not independent of time as different parts of the disk have different enrichment histories (e.g., changes in the age-metallicity relation across the disk observed in Aguirre et al. 2018; Feuillet et al. 2018; Vázquez et al. 2022; Imig et al. 2023). Exploring differences among the α -element groups is key for determining the origins of the thick disk, and whether the two groups have different physical origins (e.g., Chiappini et al. 1997; Spitoni et al. 2019; Xiang & Rix 2022; Robin et al. 2022) or if they are part of one continuous structure (e.g., Bensby et al. 2007; Bovy et al. 2012a; Kawata & Chiappini 2016; Hayden et al. 2017; Anders et al. 2018).

The two measures of scale length, $h_{r,in}$ and $h_{r,out}$ vary with both time and metallicity (Figure 7). The break radius, r_{break} appears independent of time and varies only with metallicity, with metal-poor populations characterized by a larger break radius (Figure 7; bottom). These trends depict that young, metal-poor populations are more radially extended than old, metal-rich population, which can only be a result of radially-dependent chemical evolution in the disk and supports an inside-out formation process (e.g., Larson 1976; Matteucci & Francois 1989; Bird et al. 2013). The inner galaxy assembled first and enriched quickly due to the higher concentration of gas, a trend which expanded outwards to present day where large radii are forming stars from metal-poor still relatively pristine gas. This results in a negative age and chemical gradient in the disk, which is reflected in our results and in many other observations.

The radial profile broadening metric, $h_{r,in}$ and $h_{r,out}$ varies only with time (Figure 8). This implies that while any population is born in a sharply peaked ring-like profile, the shape of the peak broadens with time. This has previously been attributed to stellar radial migration (Bovy et al. 2016b; Mackereth et al. 2017), explaining the trend through stars moving away from their birth radius through dynamical interactions with transient density perturbations in the disk like the spiral arms or the galactic bar (e.g., Schönrich & Binney 2009). The older stars have had more time to migrate, and therefore migrate farther on average, broadening the peak of the profile. The high- α populations, despite starting more centrally concentrated, experienced comparable amounts of migration as the low- α populations of the same age.

The vertical parameters, scale height ($h_{z,\odot}$) and disk flaring (A_{flare}) both increase with age and decrease with metallicity (Figure 10). This implies that some combination of time-dependent process, such as dynamical heating, and *in situ* structure determines the thickness of a disk. Consistent with the predictions of Minchev et al. (2015), we find the largest scale height and strongest flaring in the old, metal-poor populations. Interaction with a satellite galaxy or a merger event can lead to the heating of a disk (e.g., Quinn et al. 1993), and such merger events contribute significantly more to disk flaring than radial migration does (Minchev et al. 2012). Radial migration is actually believed to suppress disk flaring, as migrator stars end up cooling the outer disk when mergers are present (Minchev et al. 2014, 2018).

The trend with metallicity, on the other hand, reflects the vertical chemical gradient in the disk (e.g., Carrell et al. 2012; Hayden et al. 2014) and points towards a vertically “upside-down” disk assembly scenario where stars formed earlier are more subject to dynamical scattering, and as time goes on the disk stabilizes and becomes more rotationally supported, resulting in younger populations being thinner geometrically (e.g., Bird et al. 2013, 2021). Our results suggest a combination of effects; both dynamical heating and that older stars were “born thicker” being responsible for the scale height varying with age and metallicity.

We find the strongest flaring in the old, α -rich populations, contrary to some previous studies (e.g., Bovy et al. 2016b; Mackereth et al. 2017) but in good agreement with more recent observations (e.g., Yu et al. 2021; Lian et al. 2022) and the models of Minchev et al. (2015). Radial migration has the effect of suppressing disk flaring in older populations (Minchev et al. 2014, 2018), so these results are most consistent with the disk flaring produced by merger events (García de la Cruz et al. 2020, e.e.,g) or the natural inside-out growth of galactic disks Minchev et al. (2015, e.g.). Early star formation in efficient gas “clumps” have also been shown to result in flared low- α disks in simulations (Beraldo e Silva et al. 2020), which also reproduce the observed chemical bimodality in the disk (e.g., Clarke et al. 2019; Amarante et al. 2020).

The overall mass assembly and star formation history of the Milky Way are similar to that predicted by a merger event in simulated galaxies (e.g., Mackereth et al. 2018) where fresh gas is supplied to a galaxy by an infalling satellite. The age overlap between the low- α and high- α disk, however, implies that the disks evolved at least partially in parallel, which disfavors some “two-infall” sequential formation models (e.g., Chiappini et al. 1997; Spitoni et al. 2019),

but is expected in radially-dependent chemical evolution with stellar migration (e.g., Schönrich & Binney 2009; Minchev et al. 2013; Nidever et al. 2014), and one of the main predictions in the star formation clump scenario (Clarke et al. 2019; Beraldo e Silva et al. 2020). An age overlap could also arise under a two-infall scenario in which the accreted gas preferentially falls in at large radii (e.g., Chiappini 2008; Andrews et al. 2017; Sharma et al. 2021). Current stellar age estimates are not yet precise enough to disentangle this history further. See Zasowski et al. (*in prep*) for a complementary comparison of mass assembly history inferred from simulations.

7. CONCLUSIONS

Using the final data release of APOGEE (Majewski et al. 2017) and stellar age estimates from the `distmass` catalog (Stone-Martinez et al. 2024), we present new measurements of the structural parameters of the Milky Way disk and explore how they vary with metallicity ([M/H]), α -element abundances ($[\alpha/M]$) and stellar age. Our main conclusions are summarized as:

- **Radial and Vertical Density Profiles:** Most high- α populations reasonably approximate a single exponential radial profile, while the low- α populations are best fit by a “donut”-shaped broken exponential radial profile, with the peak radius moving outward with decreasing metallicity. These findings are consistent with previous studies (e.g., Bovy et al. 2016b; Mackereth et al. 2017; Yu et al. 2021; Lian et al. 2022). We measure the total mass-weighted scale length to be 2.74 ± 0.2 kpc for the low- α disk, 1.58 ± 0.2 kpc for the high- α disk and 2.37 ± 0.2 kpc for the sum population, although we emphasize that a single scale length fit oversimplifies the complex profiles of different stellar populations.
- **Profile Broadening:** The difference between the inner-disk scale length and outer-disk scale length quantifies the broadening of a density profile. We find that the broadening is independent of metallicity but strongly correlates with stellar age, indicating that a time-dependent process like radial migration is responsible for the evolution of the density structure for each stellar population with time (e.g., Mackereth et al. 2017; Lian et al. 2022).
- **Vertical Flaring:** We find the strongest vertical flaring in the old, high- α populations, which is in apparent conflict with some studies (e.g., Bovy et al. 2016b; Mackereth et al. 2017) but consistent with more recent results (e.g., Yu et al. 2021;

Lian et al. 2022) and the models of Minchev et al. (2015), likely due to the better spatial sampling of both the inner and outer galaxy in the newer data sets. Radial migration typically works to suppress flaring in the outer disk for the oldest populations (Minchev et al. 2014, 2018), so our results are more consistent with flaring produced by a merger event in the disk (e.g., Minchev et al. 2014; García de la Cruz et al. 2020).

- **Total Scale Length:** We measure the total scale length of $R_d = 2.2 \pm 0.2$ kpc. In a light-weighted profile, the scale length increases to $R_d = 2.83 \pm 0.2$ kpc as a result of the youngest (brightest) populations having longer scale lengths in general. This helps close the observational discrepancy suggesting that the Milky Way is too compact for its mass compared to other galaxies (e.g., Bovy & Rix 2013; Licquia & Newman 2016; Boardman et al. 2020), although this should still be regarded as a lower limit because the youngest stars are excluded from our sample.
- **Integrated Colors:** We measure a present day integrated color of the Milky Way of $(g - r)_0 = 0.72 \pm 0.02$. To our knowledge, this is the first estimate of the Milky Way disk’s integrated colors directly from its stellar populations. This value is consistent with studies using Milky Way analogs or machine learning models as proxies (e.g., Mutch et al. 2011; Licquia et al. 2015; Fielder et al. 2021) and places the Milky Way in the “green valley” zone of the Galaxy color-mass diagram. Our results support that the present-day Milky Way is best classified as a red spiral galaxy (e.g., Masters et al. 2010). Our estimate of the MW’s colors become bluer with increasing lookback time, to a value of $(g - r)_0 = 0.52 \pm 0.12$ at our oldest age bin more consistent with blue cloud galaxies. This is expected with the observed evolution of this relationship at higher redshifts (Bell et al. 2004; Weiner et al. 2005), and suggests that the Milky Way has only been in the green valley for the last ≈ 3 Gyr.
- **Total Star Formation History:** The star formation history of the Milky Way disk increases over early times, peaks around ≥ 7 Gyr ($z \geq 0.9$) ago and gradually declines over time. The high- α population formed quickly early on, peaking in our second-oldest age bin and declining quickly over time. The star formation history of the low- α population peaks around 7 Gyr and decreases

more slowly over time. This is similar to the behavior seen in simulations (Mackereth et al. 2018; Gebek & Matthee 2022), where chemical bimodality arises from a gas-rich merger event. We also find significant age overlap between the low- α and high- α disks, consistent with other studies (e.g., Haywood et al. 2013; Hayden et al. 2017; Aguirre et al. 2018; Gent et al. 2022; Imig et al. 2023) suggesting the co-evolution of the two disks, although the age uncertainties may contribute to this overlap.

In summary, our findings suggest that the present-day Milky Way is a red spiral galaxy characterized by a relatively small scale length. The low- α and high- α components of the disks, while overlapping in age, show different trends among their density profile parameters, reflecting the complex evolution history of our Galaxy.

ACKNOWLEDGEMENTS

We would like to thank in advance the anonymous referee for their time and expertise reviewing our manuscript.

J.I. and J.A.H. gratefully acknowledge support from NSF grant AST-1909897.

T.C.B acknowledges partial support from grant PHY 14-30152; Physics Frontier Center/JINA Center for the Evolution of the Elements (JINA-CEE), and from OISE-1927130: The International Research Network for Nuclear Astrophysics (IReNA), awarded by the US National Science Foundation.

Funding for the Sloan Digital Sky Survey IV has been provided by the Alfred P. Sloan Foundation, the U.S. Department of Energy Office of Science, and the Participating Institutions. SDSS acknowledges support and resources from the Center for High-Performance Computing at the University of Utah. The SDSS web site is www.sdss.org.

SDSS is managed by the Astrophysical Research Consortium for the Participating Institutions of the

SDSS Collaboration including the Brazilian Participation Group, the Carnegie Institution for Science, Carnegie Mellon University, Center for Astrophysics — Harvard & Smithsonian (CfA), the Chilean Participation Group, the French Participation Group, Instituto de Astrofísica de Canarias, The Johns Hopkins University, Kavli Institute for the Physics and Mathematics of the Universe (IPMU) / University of Tokyo, the Korean Participation Group, Lawrence Berkeley National Laboratory, Leibniz Institut für Astrophysik Potsdam (AIP), Max-Planck-Institut für Astronomie (MPIA Heidelberg), Max-Planck-Institut für Astrophysik (MPA Garching), Max-Planck-Institut für Extraterrestrische Physik (MPE), National Astronomical Observatories of China, New Mexico State University, New York University, University of Notre Dame, Observatório Nacional / MCTI, The Ohio State University, Pennsylvania State University, Shanghai Astronomical Observatory, United Kingdom Participation Group, Universidad Nacional Autónoma de México, University of Arizona, University of Colorado Boulder, University of Oxford, University of Portsmouth, University of Utah, University of Virginia, University of Washington, University of Wisconsin, Vanderbilt University, and Yale University.

DATA AVAILABILITY

The SDSS DR17 data is publicly available, and more information including data access instructions can be found at <https://www.sdss4.org/dr17/>. The `distmass` value-added catalog is available for download through the SDSS Science Archive Server (<https://data.sdss.org/sas/dr17/apogee/vac/apogee-distmass/>). All code required for reproducing the APOGEE selection function, the number density MCMC fits, and the figures in this study is provided at https://github.com/astrojimig/mw_density_imig2025.

REFERENCES

- Abdurro'uf, Accetta, K., Aerts, C., et al. 2022, ApJS, 259, 35, doi: [10.3847/1538-4365/ac4414](https://doi.org/10.3847/1538-4365/ac4414)
- Aguirre, V. S., Bojsen-Hansen, M., Slumstrup, D., et al. 2018, Monthly Notices of the Royal Astronomical Society, doi: [10.1093/mnras/sty150](https://doi.org/10.1093/mnras/sty150)
- Allende Prieto, C., Beers, T. C., Wilhelm, R., et al. 2006, ApJ, 636, 804, doi: [10.1086/498131](https://doi.org/10.1086/498131)
- Amarante, J. A. S., Beraldo e Silva, L., Debattista, V. P., & Smith, M. C. 2020, ApJL, 891, L30, doi: [10.3847/2041-8213/ab78a4](https://doi.org/10.3847/2041-8213/ab78a4)
- Anders, F., Chiappini, C., Santiago, B. X., et al. 2018, A&A, 619, A125, doi: [10.1051/0004-6361/201833099](https://doi.org/10.1051/0004-6361/201833099)
- Andrews, B. H., Weinberg, D. H., Schönrich, R., & Johnson, J. A. 2017, ApJ, 835, 224, doi: [10.3847/1538-4357/835/2/224](https://doi.org/10.3847/1538-4357/835/2/224)

- Baldry, I. K., Glazebrook, K., Brinkmann, J., et al. 2004, *ApJ*, 600, 681, doi: [10.1086/380092](https://doi.org/10.1086/380092)
- Beaton, R. L., Oelkers, R. J., Hayes, C. R., et al. 2021, *The Astronomical Journal*, 162, 302, doi: [10.3847/1538-3881/ac260c](https://doi.org/10.3847/1538-3881/ac260c)
- Belfiore, F., Westfall, K. B., Schaefer, A., et al. 2019, *AJ*, 158, 160, doi: [10.3847/1538-3881/ab3e4e](https://doi.org/10.3847/1538-3881/ab3e4e)
- Bell, E. F., Wolf, C., Meisenheimer, K., et al. 2004, *ApJ*, 608, 752, doi: [10.1086/420778](https://doi.org/10.1086/420778)
- Bensby, T., Feltzing, S., Lundström, I., & Ilyin, I. 2005, *A&A*, 433, 185, doi: [10.1051/0004-6361:20040332](https://doi.org/10.1051/0004-6361:20040332)
- Bensby, T., Zenn, A. R., Oey, M. S., & Feltzing, S. 2007, *The Astrophysical Journal*, 663, L13, doi: [10.1086/519792](https://doi.org/10.1086/519792)
- Beraldo e Silva, L., Debattista, V. P., Khachaturyants, T., & Nidever, D. 2020, *MNRAS*, 492, 4716, doi: [10.1093/mnras/staa065](https://doi.org/10.1093/mnras/staa065)
- Bernard, E. J., Schultheis, M., Matteo, P. D., et al. 2018, *Monthly Notices of the Royal Astronomical Society*, 477, 3507, doi: [10.1093/mnras/sty902](https://doi.org/10.1093/mnras/sty902)
- Bird, J. C., Kazantzidis, S., Weinberg, D. H., et al. 2013, *The Astrophysical Journal*, 773, 43, doi: [10.1088/0004-637x/773/1/43](https://doi.org/10.1088/0004-637x/773/1/43)
- Bird, J. C., Loebman, S. R., Weinberg, D. H., et al. 2021, *Monthly Notices of the Royal Astronomical Society*, 503, 1815, doi: [10.1093/mnras/stab289](https://doi.org/10.1093/mnras/stab289)
- Bland-Hawthorn, J., & Gerhard, O. 2016, *ARA&A*, 54, 529, doi: [10.1146/annurev-astro-081915-023441](https://doi.org/10.1146/annurev-astro-081915-023441)
- Blanton, M. R., Kazin, E., Muna, D., Weaver, B. A., & Price-Whelan, A. 2011, *AJ*, 142, 31, doi: [10.1088/0004-6256/142/1/31](https://doi.org/10.1088/0004-6256/142/1/31)
- Blanton, M. R., & Roweis, S. 2007, *The Astronomical Journal*, 133, 734, doi: [10.1086/510127](https://doi.org/10.1086/510127)
- Blanton, M. R., Bershady, M. A., Abolfathi, B., et al. 2017, *AJ*, 154, 28, doi: [10.3847/1538-3881/aa7567](https://doi.org/10.3847/1538-3881/aa7567)
- Boardman, N., Zasowski, G., Newman, J. A., et al. 2020, *Monthly Notices of the Royal Astronomical Society*, 498, 4943, doi: [10.1093/mnras/staa2731](https://doi.org/10.1093/mnras/staa2731)
- Boecker, A., Neumayer, N., Pillepich, A., et al. 2022, *Monthly Notices of the Royal Astronomical Society*, 519, 5202, doi: [10.1093/mnras/stac3759](https://doi.org/10.1093/mnras/stac3759)
- Bonaca, A., Conroy, C., Wetzel, A., Hopkins, P. F., & Kereš, D. 2017, *ApJ*, 845, 101, doi: [10.3847/1538-4357/aa7d0c](https://doi.org/10.3847/1538-4357/aa7d0c)
- Bovy, J., & Rix, H.-W. 2013, *The Astrophysical Journal*, 779, 115, doi: [10.1088/0004-637x/779/2/115](https://doi.org/10.1088/0004-637x/779/2/115)
- Bovy, J., Rix, H.-W., Green, G. M., Schlafly, E. F., & Finkbeiner, D. P. 2016a, *The Astrophysical Journal*, 818, 130, doi: [10.3847/0004-637x/818/2/130](https://doi.org/10.3847/0004-637x/818/2/130)
- Bovy, J., Rix, H.-W., & Hogg, D. W. 2012a, *The Astrophysical Journal*, 751, 131, doi: [10.1088/0004-637x/751/2/131](https://doi.org/10.1088/0004-637x/751/2/131)
- Bovy, J., Rix, H.-W., Liu, C., et al. 2012b, *The Astrophysical Journal*, 753, 148, doi: [10.1088/0004-637x/753/2/148](https://doi.org/10.1088/0004-637x/753/2/148)
- Bovy, J., Rix, H.-W., Schlafly, E. F., et al. 2016b, *The Astrophysical Journal*, 823, 30, doi: [10.3847/0004-637x/823/1/30](https://doi.org/10.3847/0004-637x/823/1/30)
- Bowen, I. S., & Vaughan, A. H. J. 1973, *ApOpt*, 12, 1430, doi: [10.1364/AO.12.001430](https://doi.org/10.1364/AO.12.001430)
- Bressan, A., Marigo, P., Girardi, L., et al. 2012, *Monthly Notices of the Royal Astronomical Society*, 427, 127–145, doi: [10.1111/j.1365-2966.2012.21948.x](https://doi.org/10.1111/j.1365-2966.2012.21948.x)
- Buder, S., Asplund, M., Duong, L., et al. 2018, *Monthly Notices of the Royal Astronomical Society*, 478, 4513–4552, doi: [10.1093/mnras/sty1281](https://doi.org/10.1093/mnras/sty1281)
- Bundy, K., Bershady, M. A., Law, D. R., et al. 2015, *ApJ*, 798, 7, doi: [10.1088/0004-637X/798/1/7](https://doi.org/10.1088/0004-637X/798/1/7)
- Burstein, D., Faber, S. M., Gaskell, C. M., & Krumm, N. 1984, *ApJ*, 287, 586, doi: [10.1086/162718](https://doi.org/10.1086/162718)
- Carrell, K., Chen, Y., & Zhao, G. 2012, *The Astronomical Journal*, 144, 185, doi: [10.1088/0004-6256/144/6/185](https://doi.org/10.1088/0004-6256/144/6/185)
- Cenarro, A. J., Cardiel, N., Gorgas, J., et al. 2001, *MNRAS*, 326, 959, doi: [10.1046/j.1365-8711.2001.04688.x](https://doi.org/10.1046/j.1365-8711.2001.04688.x)
- Chapman, S., Girardi, L., Bressan, A., et al. 2014, *MNRAS*, 444, 2525, doi: [10.1093/mnras/stu1605](https://doi.org/10.1093/mnras/stu1605)
- Chiappini, C. 2008, *Proceedings of the International Astronomical Union*, 4, 191–196, doi: [10.1017/S1743921308027580](https://doi.org/10.1017/S1743921308027580)
- Chiappini, C., Matteucci, F., & Gratton, R. 1997, *The Astrophysical Journal*, 477, 765–780, doi: [10.1086/303726](https://doi.org/10.1086/303726)
- Choi, J., Dotter, A., Conroy, C., et al. 2016, *The Astrophysical Journal*, 823, 102, doi: [10.3847/0004-637x/823/2/102](https://doi.org/10.3847/0004-637x/823/2/102)
- Clarke, A. J., Debattista, V. P., Nidever, D. L., et al. 2019, *MNRAS*, 484, 3476, doi: [10.1093/mnras/stz104](https://doi.org/10.1093/mnras/stz104)
- Conroy, C., & van Dokkum, P. 2012, *ApJ*, 747, 69, doi: [10.1088/0004-637X/747/1/69](https://doi.org/10.1088/0004-637X/747/1/69)
- Conroy, C., Weinberg, D. H., Naidu, R. P., et al. 2022, *Birth of the Galactic Disk Revealed by the H3 Survey*, arXiv, doi: [10.48550/ARXIV.2204.02989](https://doi.org/10.48550/ARXIV.2204.02989)
- Croom, S. M., Owers, M. S., Scott, N., et al. 2021, *Monthly Notices of the Royal Astronomical Society*, doi: [10.1093/mnras/stab229](https://doi.org/10.1093/mnras/stab229)
- Dias, W. S., Monteiro, H., Lépine, J. R. D., & Barros, D. A. 2019, *Monthly Notices of the Royal Astronomical Society*, 486, 5726, doi: [10.1093/mnras/stz1196](https://doi.org/10.1093/mnras/stz1196)

- Díaz-García, S., Comerón, S., Courteau, S., et al. 2022, *Astronomy & Astrophysics*, 667, A109, doi: [10.1051/0004-6361/202142447](https://doi.org/10.1051/0004-6361/202142447)
- Doi, M., Tanaka, M., Fukugita, M., et al. 2010, *The Astronomical Journal*, 139, 1628, doi: [10.1088/0004-6256/139/4/1628](https://doi.org/10.1088/0004-6256/139/4/1628)
- Drimmel, R., Cabrera-Lavers, A., & López-Corredoira, M. 2003, *A&A*, 409, 205, doi: [10.1051/0004-6361:20031070](https://doi.org/10.1051/0004-6361:20031070)
- Eilers, A.-C., Hogg, D. W., Rix, H.-W., et al. 2022, *ApJ*, 928, 23, doi: [10.3847/1538-4357/ac54ad](https://doi.org/10.3847/1538-4357/ac54ad)
- Fantin, N. J., Cô té, P., McConnachie, A. W., et al. 2019, *The Astrophysical Journal*, 887, 148, doi: [10.3847/1538-4357/ab5521](https://doi.org/10.3847/1538-4357/ab5521)
- Fathi, K., Allen, M., Boch, T., Hatziminaoglou, E., & Peletier, R. F. 2010, *Monthly Notices of the Royal Astronomical Society*, no, doi: [10.1111/j.1365-2966.2010.16812.x](https://doi.org/10.1111/j.1365-2966.2010.16812.x)
- Feuillet, D. K., Bovy, J., Holtzman, J., et al. 2018, *MNRAS*, 477, 2326, doi: [10.1093/mnras/sty779](https://doi.org/10.1093/mnras/sty779)
- Fielder, C. E., Newman, J. A., Andrews, B. H., et al. 2021, *Monthly Notices of the Royal Astronomical Society*, 508, 4459, doi: [10.1093/mnras/stab2618](https://doi.org/10.1093/mnras/stab2618)
- Fitzpatrick, E. L., Massa, D., Gordon, K. D., Bohlin, R., & Clayton, G. C. 2019, *ApJ*, 886, 108, doi: [10.3847/1538-4357/ab4c3a](https://doi.org/10.3847/1538-4357/ab4c3a)
- Fraser-Mckelvie, A., Aragó n-Salamanca, A., Merrifield, M., et al. 2018, *Monthly Notices of the Royal Astronomical Society*, 481, 5580, doi: [10.1093/mnras/sty2563](https://doi.org/10.1093/mnras/sty2563)
- Fraser-Mckelvie, A., Merrifield, M., & Aragó n-Salamanca, A. 2019, *Monthly Notices of the Royal Astronomical Society*, 489, 5030, doi: [10.1093/mnras/stz2493](https://doi.org/10.1093/mnras/stz2493)
- Fraser-Mckelvie, A., Merrifield, M., Aragó n-Salamanca, A., et al. 2020, *Monthly Notices of the Royal Astronomical Society*, 499, 1116, doi: [10.1093/mnras/staa2866](https://doi.org/10.1093/mnras/staa2866)
- Freeman, K. C. 1970, *ApJ*, 160, 811, doi: [10.1086/150474](https://doi.org/10.1086/150474)
- Fuhrmann, K. 1998, *A&A*, 338, 161
- Gaia Collaboration, Brown, A. G. A., Vallenari, A., et al. 2018, *A&A*, 616, A1, doi: [10.1051/0004-6361/201833051](https://doi.org/10.1051/0004-6361/201833051)
- . 2021, *A&A*, 650, C3, doi: [10.1051/0004-6361/202039657e](https://doi.org/10.1051/0004-6361/202039657e)
- Galliano, F., Nervesian, A., Bianchi, S., et al. 2021, *Astronomy & Astrophysics*, 649, A18, doi: [10.1051/0004-6361/202039701](https://doi.org/10.1051/0004-6361/202039701)
- García Pérez, A. E., Prieto, C. A., Holtzman, J. A., et al. 2016, *The Astronomical Journal*, 151, 144, doi: [10.3847/0004-6256/151/6/144](https://doi.org/10.3847/0004-6256/151/6/144)
- García de la Cruz, J., Martig, M., Minchev, I., & James, P. 2020, *Monthly Notices of the Royal Astronomical Society*, 501, 5105–5120, doi: [10.1093/mnras/staa3906](https://doi.org/10.1093/mnras/staa3906)
- Gebek, A., & Matthee, J. 2022, *The Astrophysical Journal*, 924, 73, doi: [10.3847/1538-4357/ac350b](https://doi.org/10.3847/1538-4357/ac350b)
- Gent, M. R., Eitner, P., Laporte, C. F. P., et al. 2022, *The Prince and The Pauper: Co-evolution of the thin and thick disc in the Milky Way*, arXiv, doi: [10.48550/ARXIV.2206.10949](https://doi.org/10.48550/ARXIV.2206.10949)
- Gilmore, G., & Reid, N. 1983, *MNRAS*, 202, 1025, doi: [10.1093/mnras/202.4.1025](https://doi.org/10.1093/mnras/202.4.1025)
- Gilmore, G., Randich, S., Worley, C. C., et al. 2022, *A&A*, 666, A120, doi: [10.1051/0004-6361/202243134](https://doi.org/10.1051/0004-6361/202243134)
- Green, G. M., Schlafly, E., Zucker, C., Speagle, J. S., & Finkbeiner, D. 2019, *ApJ*, 887, 93, doi: [10.3847/1538-4357/ab5362](https://doi.org/10.3847/1538-4357/ab5362)
- Gunn, J. E., Siegmund, W. A., Mannery, E. J., et al. 2006, *AJ*, 131, 2332, doi: [10.1086/500975](https://doi.org/10.1086/500975)
- Halle, A., Matteo, P. D., Haywood, M., & Combes, F. 2015, *Astronomy & Astrophysics*, 578, A58, doi: [10.1051/0004-6361/201525612](https://doi.org/10.1051/0004-6361/201525612)
- Hawkins, K., Jofré , P., Masseron, T., & Gilmore, G. 2015, *Monthly Notices of the Royal Astronomical Society*, 453, 758, doi: [10.1093/mnras/stv1586](https://doi.org/10.1093/mnras/stv1586)
- Hayden, M. R., Recio-Blanco, A., de Laverny, P., Mikolaitis, S., & Worley, C. C. 2017, *Astronomy & Astrophysics*, 608, L1, doi: [10.1051/0004-6361/201731494](https://doi.org/10.1051/0004-6361/201731494)
- Hayden, M. R., Holtzman, J. A., Bovy, J., et al. 2014, *AJ*, 147, 116, doi: [10.1088/0004-6256/147/5/116](https://doi.org/10.1088/0004-6256/147/5/116)
- Hayden, M. R., Bovy, J., Holtzman, J. A., et al. 2015, *The Astrophysical Journal*, 808, 132, doi: [10.1088/0004-637x/808/2/132](https://doi.org/10.1088/0004-637x/808/2/132)
- Haywood, M., Matteo, P. D., Lehnert, M. D., Katz, D., & Gó mez, A. 2013, *Astronomy & Astrophysics*, 560, A109, doi: [10.1051/0004-6361/201321397](https://doi.org/10.1051/0004-6361/201321397)
- Holtzman, J. A., Shetrone, M., Johnson, J. A., et al. 2015, *AJ*, 150, 148, doi: [10.1088/0004-6256/150/5/148](https://doi.org/10.1088/0004-6256/150/5/148)
- Holtzman, J. A., Hasselquist, S., Shetrone, M., et al. 2018, *The Astronomical Journal*, 156, 125, doi: [10.3847/1538-3881/aad4f9](https://doi.org/10.3847/1538-3881/aad4f9)
- Horta, D., Mackereth, J. T., Schiavon, R. P., et al. 2020, *Monthly Notices of the Royal Astronomical Society*, 500, 5462, doi: [10.1093/mnras/staa3598](https://doi.org/10.1093/mnras/staa3598)
- Iben, Icko, J. 1965, *ApJ*, 142, 1447, doi: [10.1086/148429](https://doi.org/10.1086/148429)
- Imig, J., Price, C., Holtzman, J. A., et al. 2023, *The Astrophysical Journal*, 954, 124, doi: [10.3847/1538-4357/ace9b8](https://doi.org/10.3847/1538-4357/ace9b8)
- Jurić, M., Ivezić, Ž., Brooks, A., et al. 2008, *ApJ*, 673, 864, doi: [10.1086/523619](https://doi.org/10.1086/523619)

- Jönsson, H., Prieto, C. A., Holtzman, J. A., et al. 2018, *The Astronomical Journal*, 156, 126, doi: [10.3847/1538-3881/aad4f5](https://doi.org/10.3847/1538-3881/aad4f5)
- Jönsson, H., Holtzman, J. A., Prieto, C. A., et al. 2020, *The Astronomical Journal*, 160, 120, doi: [10.3847/1538-3881/aba592](https://doi.org/10.3847/1538-3881/aba592)
- Katz, D., Gómez, A., Haywood, M., Snaith, O., & Matteo, P. D. 2021, *Astronomy & Astrophysics*, 655, A111, doi: [10.1051/0004-6361/202140453](https://doi.org/10.1051/0004-6361/202140453)
- Kawata, D., & Chiappini, C. 2016, *Astronomische Nachrichten*, 337, 976, doi: [10.1002/asna.201612421](https://doi.org/10.1002/asna.201612421)
- Khoperskov, S., Gerhard, O., Matteo, P. D., et al. 2020a, *Astronomy & Astrophysics*, 634, L8, doi: [10.1051/0004-6361/201936645](https://doi.org/10.1051/0004-6361/201936645)
- Khoperskov, S., Matteo, P. D., Haywood, M., Gómez, A., & Snaith, O. N. 2020b, *Astronomy & Astrophysics*, 638, A144, doi: [10.1051/0004-6361/201937188](https://doi.org/10.1051/0004-6361/201937188)
- Kobayashi, C., Umeda, H., Nomoto, K., Tominaga, N., & Ohkubo, T. 2006, *ApJ*, 653, 1145, doi: [10.1086/508914](https://doi.org/10.1086/508914)
- Kordopatis, G., Gilmore, G., Wyse, R. F. G., et al. 2013, *MNRAS*, 436, 3231, doi: [10.1093/mnras/stt1804](https://doi.org/10.1093/mnras/stt1804)
- Kroupa, P. 2002, *Science*, 295, 82, doi: [10.1126/science.1067524](https://doi.org/10.1126/science.1067524)
- Kruijssen, J. M. D., Pfeffer, J. L., Reina-Campos, M., Crain, R. A., & Bastian, N. 2019, *MNRAS*, 486, 3180, doi: [10.1093/mnras/sty1609](https://doi.org/10.1093/mnras/sty1609)
- La Barbera, F., Ferreras, I., Vazdekis, A., et al. 2013, *MNRAS*, 433, 3017, doi: [10.1093/mnras/stt943](https://doi.org/10.1093/mnras/stt943)
- Lange, R., Driver, S. P., Robotham, A. S. G., et al. 2015, *Monthly Notices of the Royal Astronomical Society*, 447, 2603, doi: [10.1093/mnras/stu2467](https://doi.org/10.1093/mnras/stu2467)
- Larson, R. B. 1976, *MNRAS*, 176, 31, doi: [10.1093/mnras/176.1.31](https://doi.org/10.1093/mnras/176.1.31)
- Lee, Y. S., Beers, T. C., An, D., et al. 2011, *ApJ*, 738, 187, doi: [10.1088/0004-637X/738/2/187](https://doi.org/10.1088/0004-637X/738/2/187)
- Leung, H. W., & Bovy, J. 2018, *Monthly Notices of the Royal Astronomical Society*, doi: [10.1093/mnras/sty3217](https://doi.org/10.1093/mnras/sty3217)
- Lian, J., Zasowski, G., Mackereth, T., et al. 2022, *MNRAS*
- Licquia, T. C., & Newman, J. A. 2016, *ApJ*, 831, 71, doi: [10.3847/0004-637X/831/1/71](https://doi.org/10.3847/0004-637X/831/1/71)
- Licquia, T. C., Newman, J. A., & Brinchmann, J. 2015, *The Astrophysical Journal*, 809, 96, doi: [10.1088/0004-637x/809/1/96](https://doi.org/10.1088/0004-637x/809/1/96)
- Luo, A.-L., Zhao, Y.-H., Zhao, G., et al. 2015, *Research in Astronomy and Astrophysics*, 15, 1095–1124, doi: [10.1088/1674-4527/15/8/002](https://doi.org/10.1088/1674-4527/15/8/002)
- Mackereth, J. T., & Bovy, J. 2020, *MNRAS*, 492, 3631, doi: [10.1093/mnras/staa047](https://doi.org/10.1093/mnras/staa047)
- Mackereth, J. T., Crain, R. A., Schiavon, R. P., et al. 2018, *Monthly Notices of the Royal Astronomical Society*, 477, 5072, doi: [10.1093/mnras/sty972](https://doi.org/10.1093/mnras/sty972)
- Mackereth, J. T., Bovy, J., Schiavon, R. P., et al. 2017, *MNRAS*, 471, 3057, doi: [10.1093/mnras/stx1774](https://doi.org/10.1093/mnras/stx1774)
- Mackereth, J. T., Bovy, J., Leung, H. W., et al. 2019, *Monthly Notices of the Royal Astronomical Society*, 489, 176, doi: [10.1093/mnras/stz1521](https://doi.org/10.1093/mnras/stz1521)
- Majewski, S. R., Schiavon, R. P., Frinchaboy, P. M., et al. 2017, *AJ*, 154, 94, doi: [10.3847/1538-3881/aa784d](https://doi.org/10.3847/1538-3881/aa784d)
- Maraston, C., Hill, L., Thomas, D., et al. 2020, *Monthly Notices of the Royal Astronomical Society*, 496, 2962, doi: [10.1093/mnras/staa1489](https://doi.org/10.1093/mnras/staa1489)
- Marshall, D. J., Robin, A. C., Reylé, C., Schultheis, M., & Picaud, S. 2006, *A&A*, 453, 635, doi: [10.1051/0004-6361:20053842](https://doi.org/10.1051/0004-6361:20053842)
- Martín-Navarro, I., Bakos, J., Trujillo, I., et al. 2012, *Monthly Notices of the Royal Astronomical Society*, 427, 1102, doi: [10.1111/j.1365-2966.2012.21929.x](https://doi.org/10.1111/j.1365-2966.2012.21929.x)
- Martínez-Lombilla, C., Trujillo, I., & Knapen, J. H. 2018, *Monthly Notices of the Royal Astronomical Society*, 483, 664, doi: [10.1093/mnras/sty2886](https://doi.org/10.1093/mnras/sty2886)
- Masters, K. L., Mosleh, M., Romer, A. K., et al. 2010, *Monthly Notices of the Royal Astronomical Society*, doi: [10.1111/j.1365-2966.2010.16503.x](https://doi.org/10.1111/j.1365-2966.2010.16503.x)
- Matteucci, F., & Francois, P. 1989, *MNRAS*, 239, 885, doi: [10.1093/mnras/239.3.885](https://doi.org/10.1093/mnras/239.3.885)
- Mendel, J. T., Simard, L., Ellison, S. L., & Patton, D. R. 2013, *Monthly Notices of the Royal Astronomical Society*, 429, 2212, doi: [10.1093/mnras/sts489](https://doi.org/10.1093/mnras/sts489)
- Mészáros, S., Allende Prieto, C., Edvardsson, B., et al. 2012, *AJ*, 144, 120, doi: [10.1088/0004-6256/144/4/120](https://doi.org/10.1088/0004-6256/144/4/120)
- Michtchenko, T. A., Vieira, R. S. S., Barros, D. A., & Lépine, J. R. D. 2016, *Astronomy & Astrophysics*, 597, A39, doi: [10.1051/0004-6361/201628895](https://doi.org/10.1051/0004-6361/201628895)
- Miglio, A., Chiappini, C., Mackereth, J. T., et al. 2021, *Astronomy & Astrophysics*, 645, A85, doi: [10.1051/0004-6361/202038307](https://doi.org/10.1051/0004-6361/202038307)
- Minchev, I., Chiappini, C., & Martig, M. 2013, *Astronomy & Astrophysics*, 558, A9, doi: [10.1051/0004-6361/201220189](https://doi.org/10.1051/0004-6361/201220189)
- Minchev, I., Chiappini, C., & Martig, M. 2014, *A&A*, 572, A92, doi: [10.1051/0004-6361/201423487](https://doi.org/10.1051/0004-6361/201423487)
- Minchev, I., Famaey, B., Quillen, A. C., et al. 2012, *A&A*, 548, A127, doi: [10.1051/0004-6361/201219714](https://doi.org/10.1051/0004-6361/201219714)
- Minchev, I., Martig, M., Streich, D., et al. 2015, *ApJL*, 804, L9, doi: [10.1088/2041-8205/804/1/L9](https://doi.org/10.1088/2041-8205/804/1/L9)
- Minchev, I., Steinmetz, M., Chiappini, C., et al. 2017, *ApJ*, 834, 27, doi: [10.3847/1538-4357/834/1/27](https://doi.org/10.3847/1538-4357/834/1/27)

- Minchev, I., Anders, F., Recio-Blanco, A., et al. 2018, MNRAS, 481, 1645, doi: [10.1093/mnras/sty2033](https://doi.org/10.1093/mnras/sty2033)
- Mutch, S. J., Croton, D. J., & Poole, G. B. 2011, ApJ, 736, 84, doi: [10.1088/0004-637X/736/2/84](https://doi.org/10.1088/0004-637X/736/2/84)
- Nidever, D. L., Bovy, J., Bird, J. C., et al. 2014, ApJ, 796, 38, doi: [10.1088/0004-637X/796/1/38](https://doi.org/10.1088/0004-637X/796/1/38)
- Nidever, D. L., Holtzman, J. A., Allende Prieto, C., et al. 2015, AJ, 150, 173, doi: [10.1088/0004-6256/150/6/173](https://doi.org/10.1088/0004-6256/150/6/173)
- Oke, J. B., & Gunn, J. E. 1983, ApJ, 266, 713, doi: [10.1086/160817](https://doi.org/10.1086/160817)
- Osorio, Y., Allende Prieto, C., Hubeny, I., Mészáros, S., & Shetrone, M. 2020, A&A, 637, A80, doi: [10.1051/0004-6361/201937054](https://doi.org/10.1051/0004-6361/201937054)
- Patil, A. A., Bovy, J., Jaimungal, S., Frankel, N., & Leung, H. W. 2023, MNRAS, 526, 1997, doi: [10.1093/mnras/stad2820](https://doi.org/10.1093/mnras/stad2820)
- Pinsonneault, M. H., Elsworth, Y. P., Tayar, J., et al. 2018, The Astrophysical Journal Supplement Series, 239, 32, doi: [10.3847/1538-4365/aaebfd](https://doi.org/10.3847/1538-4365/aaebfd)
- Pohlen, M., & Trujillo, I. 2006, A&A, 454, 759, doi: [10.1051/0004-6361:20064883](https://doi.org/10.1051/0004-6361:20064883)
- Quinn, P. J., Hernquist, L., & Fullagar, D. P. 1993, ApJ, 403, 74, doi: [10.1086/172184](https://doi.org/10.1086/172184)
- Reddy, B. E., Lambert, D. L., & Prieto, C. A. 2006, Monthly Notices of the Royal Astronomical Society, 367, 1329–1366, doi: [10.1111/j.1365-2966.2006.10148.x](https://doi.org/10.1111/j.1365-2966.2006.10148.x)
- Reid, M. J., Menten, K. M., Brunthaler, A., et al. 2019, The Astrophysical Journal, 885, 131, doi: [10.3847/1538-4357/ab4a11](https://doi.org/10.3847/1538-4357/ab4a11)
- Rix, H.-W., & Bovy, J. 2013, The Astronomy and Astrophysics Review, 21, doi: [10.1007/s00159-013-0061-8](https://doi.org/10.1007/s00159-013-0061-8)
- Roberts, J. D., Pinsonneault, M. H., Johnson, J. A., et al. 2024, MNRAS, 530, 149, doi: [10.1093/mnras/stae820](https://doi.org/10.1093/mnras/stae820)
- Robin, A. C., Bienaymé, O., Fernández-Trincado, J. G., & Reylé, C. 2017, Astronomy & Astrophysics, 605, A1, doi: [10.1051/0004-6361/201630217](https://doi.org/10.1051/0004-6361/201630217)
- Robin, A. C., Reylé, C., Derrière, S., & Picaud, S. 2003, A&A, 409, 523, doi: [10.1051/0004-6361:20031117](https://doi.org/10.1051/0004-6361:20031117)
- Robin, A. C., Bienaymé, O., Salomon, J. B., et al. 2022, Astronomy & Astrophysics, 667, A98, doi: [10.1051/0004-6361/202243686](https://doi.org/10.1051/0004-6361/202243686)
- Salaris, M., & Cassisi, S. 2005, Evolution of Stars and Stellar Populations (Wiley)
- Salim, S., Rich, R. M., Charlot, S., et al. 2007, The Astrophysical Journal Supplement Series, 173, 267, doi: [10.1086/519218](https://doi.org/10.1086/519218)
- Santana, F. A., Beaton, R. L., Covey, K. R., et al. 2021, The Astronomical Journal, 162, 303, doi: [10.3847/1538-3881/ac2cbc](https://doi.org/10.3847/1538-3881/ac2cbc)
- Schawinski, K., Urry, C. M., Simmons, B. D., et al. 2014, Monthly Notices of the Royal Astronomical Society, 440, 889, doi: [10.1093/mnras/stu327](https://doi.org/10.1093/mnras/stu327)
- Schönrich, R., & Binney, J. 2009, Monthly Notices of the Royal Astronomical Society, 399, 1145, doi: [10.1111/j.1365-2966.2009.15365.x](https://doi.org/10.1111/j.1365-2966.2009.15365.x)
- Ser藤, J., Worthey, G., & Briley, M. M. 2005, ApJ, 627, 754, doi: [10.1086/430400](https://doi.org/10.1086/430400)
- Sharma, S., Hayden, M. R., & Bland-Hawthorn, J. 2021, MNRAS, 507, 5882, doi: [10.1093/mnras/stab2015](https://doi.org/10.1093/mnras/stab2015)
- Shetrone, M., Bizyaev, D., Lawler, J. E., et al. 2015, ApJS, 221, 24, doi: [10.1088/0067-0049/221/2/24](https://doi.org/10.1088/0067-0049/221/2/24)
- Shetrone, M., Tayar, J., Johnson, J. A., et al. 2019, ApJ, 872, 137, doi: [10.3847/1538-4357/aaff66](https://doi.org/10.3847/1538-4357/aaff66)
- Skrutskie, M. F., Cutri, R. M., Stiening, R., et al. 2006, AJ, 131, 1163, doi: [10.1086/498708](https://doi.org/10.1086/498708)
- Smethurst, R. J., Lintott, C. J., Simmons, B. D., et al. 2015, Monthly Notices of the Royal Astronomical Society, 450, 435, doi: [10.1093/mnras/stv161](https://doi.org/10.1093/mnras/stv161)
- Smith, V. V., Bizyaev, D., Cunha, K., et al. 2021, AJ, 161, 254, doi: [10.3847/1538-3881/abefdc](https://doi.org/10.3847/1538-3881/abefdc)
- Soubiran, C., Bienaym , O., & Siebert, A. 2003, A&A, 398, 141, doi: [10.1051/0004-6361:20021615](https://doi.org/10.1051/0004-6361:20021615)
- Spinello, C., Trager, S., Koopmans, L. V. E., & Conroy, C. 2014, MNRAS, 438, 1483, doi: [10.1093/mnras/stt2282](https://doi.org/10.1093/mnras/stt2282)
- Spinello, C., Trager, S. C., Koopmans, L. V. E., & Chen, Y. P. 2012, ApJL, 753, L32, doi: [10.1088/2041-8205/753/2/L32](https://doi.org/10.1088/2041-8205/753/2/L32)
- Spitoni, E., Aguirre, V. S., Matteucci, F., Calura, F., & Grisoni, V. 2019, Astronomy & Astrophysics, 623, A60, doi: [10.1051/0004-6361/201834188](https://doi.org/10.1051/0004-6361/201834188)
- Steinmetz, M., Matijevi , G., Enke, H., et al. 2020, AJ, 160, 82, doi: [10.3847/1538-3881/ab9ab9](https://doi.org/10.3847/1538-3881/ab9ab9)
- Stone-Martinez, A., Holtzman, J. A., Imig, J., et al. 2024, AJ, 167, 73, doi: [10.3847/1538-3881/ad12a6](https://doi.org/10.3847/1538-3881/ad12a6)
- Strateva, I., Ivezi ,  ., Knapp, G. R., et al. 2001, AJ, 122, 1861, doi: [10.1086/323301](https://doi.org/10.1086/323301)
- S  nchez, S. F., Garc  a-Benito, R., Zibetti, S., et al. 2016, Astronomy & Astrophysics, 594, A36, doi: [10.1051/0004-6361/201628661](https://doi.org/10.1051/0004-6361/201628661)
- Thomas, D., Maraston, C., Bender, R., & Mendes de Oliveira, C. 2005, ApJ, 621, 673, doi: [10.1086/426932](https://doi.org/10.1086/426932)
- Thomas, D., Maraston, C., & Johansson, J. 2011, Monthly Notices of the Royal Astronomical Society, 412, 2183, doi: [10.1111/j.1365-2966.2010.18049.x](https://doi.org/10.1111/j.1365-2966.2010.18049.x)
- Trager, S. C., Worthey, G., Faber, S. M., Burstein, D., & Gonz  lez, J. J. 1998, ApJS, 116, 1, doi: [10.1086/313099](https://doi.org/10.1086/313099)
- van der Kruit, P. C. 1979, A&AS, 38, 15

- Vázquez, C. V., Magrini, L., Casali, G., et al. 2022, *Astronomy & Astrophysics*, 660, A135, doi: [10.1051/0004-6361/202142937](https://doi.org/10.1051/0004-6361/202142937)
- Vincenzo, F., Weinberg, D. H., Miglio, A., Lane, R. R., & Roman-Lopes, A. 2021, *Monthly Notices of the Royal Astronomical Society*, 508, 5903–5920, doi: [10.1093/mnras/stab2899](https://doi.org/10.1093/mnras/stab2899)
- Wang, H.-F., Liu, C., Xu, Y., Wan, J.-C., & Deng, L. 2018, *MNRAS*, 478, 3367, doi: [10.1093/mnras/sty1058](https://doi.org/10.1093/mnras/sty1058)
- Weiner, B. J., Phillips, A. C., Faber, S. M., et al. 2005, *ApJ*, 620, 595, doi: [10.1086/427256](https://doi.org/10.1086/427256)
- Westfall, K. B., Cappellari, M., Bershady, M. A., et al. 2019, *AJ*, 158, 231, doi: [10.3847/1538-3881/ab44a2](https://doi.org/10.3847/1538-3881/ab44a2)
- Wilson, J. C., Hearty, F. R., Skrutskie, M. F., et al. 2019, *PASP*, 131, 055001, doi: [10.1088/1538-3873/ab0075](https://doi.org/10.1088/1538-3873/ab0075)
- Worthey, G. 1994, *ApJS*, 95, 107, doi: [10.1086/192096](https://doi.org/10.1086/192096)
- Worthey, G., & Ottaviani, D. L. 1997, *ApJS*, 111, 377, doi: [10.1086/313021](https://doi.org/10.1086/313021)
- Xiang, M., & Rix, H.-W. 2022, *Nature*, 603, 599, doi: [10.1038/s41586-022-04496-5](https://doi.org/10.1038/s41586-022-04496-5)
- Yan, R., Chen, Y., Lazarz, D., et al. 2019, *ApJ*, 883, 175, doi: [10.3847/1538-4357/ab3ebc](https://doi.org/10.3847/1538-4357/ab3ebc)
- Yoshii, Y. 1982, *PASJ*, 34, 365
- Yu, Z., Li, J., Chen, B., et al. 2021, *The Astrophysical Journal*, 912, 106, doi: [10.3847/1538-4357/abf098](https://doi.org/10.3847/1538-4357/abf098)
- Zamora, O., García-Hernández, D. A., Allende Prieto, C., et al. 2015, *AJ*, 149, 181, doi: [10.1088/0004-6256/149/6/181](https://doi.org/10.1088/0004-6256/149/6/181)
- Zasowski, G., Johnson, J. A., Frinchaboy, P. M., et al. 2013, *AJ*, 146, 81, doi: [10.1088/0004-6256/146/4/81](https://doi.org/10.1088/0004-6256/146/4/81)
- Zasowski, G., Cohen, R. E., Chojnowski, S. D., et al. 2017, *AJ*, 154, 198, doi: [10.3847/1538-3881/aa8df9](https://doi.org/10.3847/1538-3881/aa8df9)

APPENDIX

Table A1. Best-fit structural parameters for each mono-age-abundance stellar population. Descriptions of each parameter are outlined in Table 2. This table is available as a downloadable fits file here: https://github.com/astrojimig/mw_density_imig2025.

Stellar population bin			Best-fit parameters					
α -group	[M/H]	$\log_{10}(\text{age})$	$h_{R,\text{in}}$	$h_{R,\text{out}}$	R_{break}	$h_{Z\odot}$	A_{flare}	$\log(\nu_\odot)$
low- α	-0.65	9.35	-3.03 ^{+0.82} _{-0.52}	1.51 ^{+0.18} _{-0.22}	0.65 ^{+0.08} _{-0.07}	13.08 ^{+0.28} _{-0.17}	0.04 ^{+0.02} _{-0.01}	2.66 ^{+3.2} _{-2.13}
low- α	-0.65	9.45	-4.72 ^{+1.34} _{-0.77}	1.57 ^{+0.19} _{-0.32}	0.99 ^{+0.08} _{-0.09}	14.55 ^{+0.33} _{-0.46}	0.04 ^{+0.02} _{-0.02}	2.63 ^{+3.16} _{-2.11}
low- α	-0.65	9.55	-5.95 ^{+1.45} _{-1.22}	1.42 ^{+0.24} _{-0.43}	1.18 ^{+0.1} _{-0.11}	15.03 ^{+0.4} _{-0.72}	0.03 ^{+0.02} _{-0.01}	2.65 ^{+3.18} _{-2.12}
low- α	-0.65	9.65	-13.73 ^{+26.93} _{-5.63}	1.61 ^{+0.26} _{-0.41}	1.02 ^{+0.09} _{-0.09}	14.34 ^{+0.51} _{-0.63}	0.07 ^{+0.02} _{-0.02}	2.76 ^{+3.31} _{-2.2}
low- α	-0.65	9.75	-8.15 ^{+5.38} _{-3.02}	1.43 ^{+0.28} _{-0.46}	1.02 ^{+0.09} _{-0.07}	13.08 ^{+0.45} _{-0.46}	0.01 ^{+0.02} _{-0.01}	2.81 ^{+3.37} _{-2.25}
low- α	-0.65	9.85	-15.77 ^{+133.6} _{-9.61}	1.36 ^{+0.35} _{-0.6}	1.11 ^{+0.12} _{-0.1}	12.29 ^{+0.64} _{-1.15}	0.02 ^{+0.03} _{-0.01}	2.86 ^{+3.43} _{-2.29}
low- α	-0.55	9.25	-4.75 ^{+3.9} _{-1.74}	1.02 ^{+0.28} _{-0.31}	0.42 ^{+0.06} _{-0.04}	12.8 ^{+0.53} _{-0.67}	0.03 ^{+0.01} _{-0.02}	2.86 ^{+3.43} _{-2.29}
low- α	-0.55	9.35	-4.34 ^{+1.14} _{-0.78}	1.47 ^{+0.13} _{-0.11}	0.38 ^{+0.02} _{-0.02}	12.71 ^{+0.25} _{-0.22}	0.04 ^{+0.0} _{-0.0}	2.83 ^{+3.4} _{-2.27}
low- α	-0.55	9.45	-5.21 ^{+0.91} _{-0.65}	1.53 ^{+0.08} _{-0.09}	0.43 ^{+0.02} _{-0.02}	12.97 ^{+0.11} _{-0.12}	0.05 ^{+0.0} _{-0.0}	2.87 ^{+3.44} _{-2.29}
low- α	-0.55	9.55	-4.95 ^{+1.17} _{-0.68}	1.68 ^{+0.11} _{-0.14}	0.55 ^{+0.02} _{-0.03}	12.69 ^{+0.18} _{-0.22}	0.03 ^{+0.01} _{-0.0}	2.86 ^{+3.43} _{-2.29}
low- α	-0.55	9.65	-8.04 ^{+2.06} _{-1.39}	1.63 ^{+0.09} _{-0.12}	0.62 ^{+0.03} _{-0.03}	12.73 ^{+0.11} _{-0.16}	0.05 ^{+0.01} _{-0.01}	2.88 ^{+3.46} _{-2.31}
low- α	-0.55	9.75	-8.34 ^{+3.63} _{-1.92}	1.88 ^{+0.12} _{-0.13}	0.74 ^{+0.03} _{-0.03}	11.67 ^{+0.2} _{-0.21}	0.07 ^{+0.01} _{-0.01}	2.9 ^{+3.48} _{-2.32}
low- α	-0.55	9.85	640.6 ^{+617.35} _{-670.21}	1.38 ^{+0.15} _{-0.25}	0.77 ^{+0.04} _{-0.04}	12.06 ^{+0.31} _{-0.47}	0.05 ^{+0.01} _{-0.01}	2.96 ^{+3.55} _{-2.37}
low- α	-0.55	9.95	-4.28 ^{+1.77} _{-1.02}	1.33 ^{+0.11} _{-0.15}	0.82 ^{+0.06} _{-0.05}	10.44 ^{+0.18} _{-0.24}	0.05 ^{+0.02} _{-0.02}	2.96 ^{+3.56} _{-2.37}
low- α	-0.55	10.05	-55.5 ^{+73.57} _{-44.39}	0.61 ^{+0.15} _{-0.23}	0.92 ^{+0.09} _{-0.08}	12.29 ^{+0.28} _{-0.2}	0.05 ^{+0.03} _{-0.03}	2.95 ^{+3.54} _{-2.36}
low- α	-0.45	9.15	-2.03 ^{+0.41} _{-0.3}	1.18 ^{+0.18} _{-0.2}	0.38 ^{+0.04} _{-0.03}	12.11 ^{+0.18} _{-0.18}	0.01 ^{+0.01} _{-0.01}	2.85 ^{+3.42} _{-2.28}
low- α	-0.45	9.25	-5.66 ^{+2.03} _{-1.35}	0.92 ^{+0.1} _{-0.11}	0.33 ^{+0.02} _{-0.02}	12.53 ^{+0.16} _{-0.2}	0.03 ^{+0.0} _{-0.01}	2.94 ^{+3.53} _{-2.35}
low- α	-0.45	9.35	-8.67 ^{+4.05} _{-2.31}	1.12 ^{+0.07} _{-0.09}	0.34 ^{+0.02} _{-0.01}	12.26 ^{+0.18} _{-0.17}	0.04 ^{+0.0} _{-0.0}	2.98 ^{+3.57} _{-2.38}
low- α	-0.45	9.45	-5.21 ^{+0.88} _{-0.62}	1.34 ^{+0.05} _{-0.06}	0.34 ^{+0.01} _{-0.01}	11.96 ^{+0.08} _{-0.11}	0.04 ^{+0.0} _{-0.0}	2.98 ^{+3.57} _{-2.38}
low- α	-0.45	9.55	-5.63 ^{+1.13} _{-0.86}	1.33 ^{+0.06} _{-0.06}	0.37 ^{+0.01} _{-0.01}	11.78 ^{+0.13} _{-0.09}	0.04 ^{+0.0} _{-0.0}	3.02 ^{+3.63} _{-2.42}
low- α	-0.45	9.65	-16.95 ^{+10.02} _{-4.57}	1.29 ^{+0.06} _{-0.06}	0.45 ^{+0.01} _{-0.01}	11.83 ^{+0.12} _{-0.13}	0.04 ^{+0.0} _{-0.0}	3.05 ^{+3.66} _{-2.44}
low- α	-0.45	9.75	-23.43 ^{+58.09} _{-12.07}	1.53 ^{+0.1} _{-0.12}	0.54 ^{+0.01} _{-0.01}	11.36 ^{+0.22} _{-0.34}	0.05 ^{+0.0} _{-0.0}	3.04 ^{+3.64} _{-2.43}
low- α	-0.45	9.85	97.27 ^{+69.89} _{-141.16}	1.33 ^{+0.08} _{-0.08}	0.63 ^{+0.02} _{-0.02}	11.07 ^{+0.17} _{-0.14}	0.05 ^{+0.01} _{-0.01}	3.04 ^{+3.65} _{-2.43}
low- α	-0.45	9.95	-22.9 ^{+1511.18} _{-12.37}	1.33 ^{+0.08} _{-0.1}	0.69 ^{+0.03} _{-0.02}	10.39 ^{+0.14} _{-0.23}	0.07 ^{+0.01} _{-0.01}	3.05 ^{+3.65} _{-2.44}
low- α	-0.45	10.05	-7.69 ^{+13.39} _{-2.46}	0.9 ^{+0.12} _{-0.18}	0.75 ^{+0.06} _{-0.06}	11.11 ^{+0.23} _{-0.23}	0.04 ^{+0.02} _{-0.02}	3.0 ^{+3.6} _{-2.4}
low- α	-0.35	9.05	-2.11 ^{+0.38} _{-0.34}	1.13 ^{+0.21} _{-0.28}	0.35 ^{+0.03} _{-0.04}	12.07 ^{+0.16} _{-0.19}	0.01 ^{+0.01} _{-0.01}	2.9 ^{+3.48} _{-2.32}
low- α	-0.35	9.15	-1.98 ^{+0.37} _{-0.29}	1.08 ^{+0.13} _{-0.14}	0.28 ^{+0.03} _{-0.02}	11.88 ^{+0.12} _{-0.17}	0.02 ^{+0.01} _{-0.01}	2.93 ^{+3.52} _{-2.34}
low- α	-0.35	9.25	-6.8 ^{+3.18} _{-1.82}	1.06 ^{+0.07} _{-0.09}	0.29 ^{+0.02} _{-0.01}	11.85 ^{+0.11} _{-0.12}	0.03 ^{+0.0} _{-0.01}	3.03 ^{+3.63} _{-2.42}
low- α	-0.35	9.35	50.06 ^{+26.89} _{-469.33}	1.05 ^{+0.06} _{-0.05}	0.26 ^{+0.01} _{-0.01}	11.79 ^{+0.14} _{-0.09}	0.03 ^{+0.0} _{-0.0}	3.12 ^{+3.74} _{-2.5}
low- α	-0.35	9.45	159.49 ^{+118.12} _{-249.09}	1.01 ^{+0.04} _{-0.06}	0.28 ^{+0.01} _{-0.01}	11.98 ^{+0.08} _{-0.13}	0.03 ^{+0.0} _{-0.0}	3.13 ^{+3.76} _{-2.51}
low- α	-0.35	9.55	-17.26 ^{+8.94} _{-4.95}	1.03 ^{+0.04} _{-0.05}	0.31 ^{+0.01} _{-0.01}	11.6 ^{+0.11} _{-0.09}	0.03 ^{+0.0} _{-0.0}	3.15 ^{+3.77} _{-2.52}
low- α	-0.35	9.65	86.45 ^{+54.87} _{-179.23}	0.97 ^{+0.06} _{-0.06}	0.35 ^{+0.01} _{-0.01}	11.53 ^{+0.14} _{-0.1}	0.04 ^{+0.0} _{-0.0}	3.15 ^{+3.78} _{-2.52}
low- α	-0.35	9.75	8.55 ^{+1.37} _{-1.75}	1.11 ^{+0.06} _{-0.06}	0.41 ^{+0.01} _{-0.01}	11.38 ^{+0.1} _{-0.13}	0.04 ^{+0.0} _{-0.0}	3.15 ^{+3.78} _{-2.52}
low- α	-0.35	9.85	6.92 ^{+1.04} _{-1.65}	1.18 ^{+0.08} _{-0.09}	0.51 ^{+0.01} _{-0.01}	10.84 ^{+0.22} _{-0.17}	0.04 ^{+0.0} _{-0.0}	3.14 ^{+3.76} _{-2.51}
low- α	-0.35	9.95	5.57 ^{+0.91} _{-1.5}	1.17 ^{+0.12} _{-0.12}	0.62 ^{+0.02} _{-0.02}	10.56 ^{+0.34} _{-0.33}	0.06 ^{+0.01} _{-0.01}	3.1 ^{+3.72} _{-2.48}
low- α	-0.35	10.05	5.52 ^{+1.58} _{-2.6}	0.44 ^{+0.17} _{-0.65}	0.68 ^{+0.06} _{-0.05}	12.62 ^{+0.32} _{-1.56}	0.04 ^{+0.02} _{-0.01}	3.07 ^{+3.68} _{-2.45}
low- α	-0.25	9.05	-2.75 ^{+0.7} _{-0.48}	1.1 ^{+0.14} _{-0.15}	0.24 ^{+0.02} _{-0.02}	11.26 ^{+0.22} _{-0.1}	0.01 ^{+0.01} _{-0.01}	3.09 ^{+3.71} _{-2.47}
low- α	-0.25	9.15	-5.04 ^{+2.25} _{-1.18}	1.35 ^{+0.14} _{-0.15}	0.22 ^{+0.01} _{-0.01}	11.03 ^{+0.23} _{-0.18}	0.02 ^{+0.0} _{-0.0}	3.17 ^{+3.81} _{-2.54}
low- α	-0.25	9.25	-6.76 ^{+17.53} _{-2.64}	1.18 ^{+0.13} _{-0.14}	0.23 ^{+0.01} _{-0.01}	10.63 ^{+0.36} _{-0.49}	0.02 ^{+0.0} _{-0.0}	3.15 ^{+3.78} _{-2.52}
low- α	-0.25	9.35	-14.53 ^{+37.4} _{-8.05}	1.2 ^{+0.2} _{-0.1}	0.24 ^{+0.01} _{-0.01}	10.3 ^{+0.7} _{-0.31}	0.03 ^{+0.0} _{-0.0}	3.2 ^{+3.84} _{-2.56}

low- α	-0.25	9.45	289.74 $^{+252.83}_{-336.23}$	1.06 $^{+0.06}_{-0.05}$	0.26 $^{+0.0}_{-0.0}$	10.98 $^{+0.15}_{-0.14}$	0.02 $^{+0.0}_{-0.0}$	3.21 $^{+3.85}_{-2.56}$
low- α	-0.25	9.55	93.75 $^{+64.34}_{-151.21}$	1.02 $^{+0.04}_{-0.05}$	0.28 $^{+0.0}_{-0.0}$	10.81 $^{+0.11}_{-0.13}$	0.03 $^{+0.0}_{-0.0}$	3.23 $^{+3.88}_{-2.59}$
low- α	-0.25	9.65	12.54 $^{+2.57}_{-3.85}$	0.94 $^{+0.04}_{-0.04}$	0.32 $^{+0.01}_{-0.01}$	10.96 $^{+0.08}_{-0.11}$	0.03 $^{+0.0}_{-0.0}$	3.23 $^{+3.87}_{-2.58}$
low- α	-0.25	9.75	7.39 $^{+1.08}_{-1.7}$	1.03 $^{+0.05}_{-0.07}$	0.36 $^{+0.01}_{-0.01}$	10.56 $^{+0.14}_{-0.15}$	0.04 $^{+0.0}_{-0.0}$	3.22 $^{+3.87}_{-2.58}$
low- α	-0.25	9.85	3.22 $^{+0.22}_{-0.26}$	1.02 $^{+0.11}_{-0.08}$	0.43 $^{+0.01}_{-0.01}$	10.77 $^{+0.41}_{-0.21}$	0.04 $^{+0.0}_{-0.0}$	3.2 $^{+3.84}_{-2.56}$
low- α	-0.25	9.95	2.92 $^{+0.21}_{-0.27}$	0.94 $^{+0.1}_{-0.11}$	0.53 $^{+0.02}_{-0.01}$	10.7 $^{+0.25}_{-0.27}$	0.05 $^{+0.0}_{-0.0}$	3.16 $^{+3.8}_{-2.53}$
low- α	-0.25	10.05	4.91 $^{+1.24}_{-3.29}$	1.11 $^{+0.16}_{-0.19}$	0.56 $^{+0.03}_{-0.03}$	9.72 $^{+0.49}_{-0.53}$	0.05 $^{+0.01}_{-0.01}$	3.16 $^{+3.79}_{-2.53}$
low- α	-0.15	9.05	-3.62 $^{+1.88}_{-0.92}$	1.03 $^{+0.16}_{-0.13}$	0.21 $^{+0.01}_{-0.01}$	10.5 $^{+0.36}_{-0.24}$	0.01 $^{+0.0}_{-0.0}$	3.22 $^{+3.86}_{-2.58}$
low- α	-0.15	9.15	-2.54 $^{+1.15}_{-0.64}$	1.4 $^{+0.13}_{-0.11}$	0.2 $^{+0.01}_{-0.01}$	9.61 $^{+0.34}_{-0.21}$	0.02 $^{+0.0}_{-0.0}$	3.26 $^{+3.91}_{-2.61}$
low- α	-0.15	9.25	-4.09 $^{+1.08}_{-0.84}$	0.99 $^{+0.04}_{-0.05}$	0.21 $^{+0.01}_{-0.01}$	9.88 $^{+0.09}_{-0.15}$	0.02 $^{+0.0}_{-0.0}$	3.25 $^{+3.9}_{-2.6}$
low- α	-0.15	9.35	-3.78 $^{+1.22}_{-1.11}$	1.06 $^{+0.04}_{-0.06}$	0.22 $^{+0.0}_{-0.0}$	9.17 $^{+0.13}_{-0.27}$	0.03 $^{+0.0}_{-0.0}$	3.32 $^{+3.98}_{-2.65}$
low- α	-0.15	9.45	-3.36 $^{+0.6}_{-0.68}$	1.19 $^{+0.03}_{-0.03}$	0.24 $^{+0.0}_{-0.0}$	8.97 $^{+0.08}_{-0.14}$	0.02 $^{+0.0}_{-0.0}$	3.33 $^{+4.0}_{-2.67}$
low- α	-0.15	9.55	-10.23 $^{+10.49}_{-3.87}$	1.24 $^{+0.05}_{-0.04}$	0.26 $^{+0.0}_{-0.0}$	9.06 $^{+0.18}_{-0.17}$	0.02 $^{+0.0}_{-0.0}$	3.34 $^{+4.01}_{-2.67}$
low- α	-0.15	9.65	11.29 $^{+3.78}_{-6.66}$	1.27 $^{+0.07}_{-0.05}$	0.29 $^{+0.0}_{-0.0}$	9.28 $^{+0.25}_{-0.15}$	0.03 $^{+0.0}_{-0.0}$	3.32 $^{+3.98}_{-2.65}$
low- α	-0.15	9.75	8.56 $^{+3.4}_{-4.98}$	1.36 $^{+0.08}_{-0.05}$	0.33 $^{+0.01}_{-0.01}$	8.82 $^{+0.37}_{-0.23}$	0.03 $^{+0.0}_{-0.0}$	3.31 $^{+3.97}_{-2.65}$
low- α	-0.15	9.85	2.65 $^{+0.13}_{-0.17}$	1.1 $^{+0.11}_{-0.09}$	0.39 $^{+0.01}_{-0.01}$	10.45 $^{+0.42}_{-0.3}$	0.03 $^{+0.0}_{-0.0}$	3.23 $^{+3.88}_{-2.59}$
low- α	-0.15	9.95	2.34 $^{+0.18}_{-0.16}$	0.79 $^{+0.12}_{-0.12}$	0.46 $^{+0.01}_{-0.01}$	10.56 $^{+0.39}_{-0.23}$	0.04 $^{+0.0}_{-0.0}$	3.21 $^{+3.85}_{-2.57}$
low- α	-0.15	10.05	2.02 $^{+0.15}_{-0.17}$	0.75 $^{+0.17}_{-0.19}$	0.51 $^{+0.03}_{-0.02}$	11.51 $^{+0.44}_{-0.42}$	0.06 $^{+0.01}_{-0.01}$	3.18 $^{+3.81}_{-2.54}$
low- α	-0.05	9.05	-14.13 $^{+98.36}_{-7.43}$	0.84 $^{+0.08}_{-0.09}$	0.16 $^{+0.01}_{-0.0}$	9.68 $^{+0.12}_{-0.25}$	0.02 $^{+0.0}_{-0.0}$	3.42 $^{+4.1}_{-2.73}$
low- α	-0.05	9.15	-31.2 $^{+73.55}_{-20.4}$	0.98 $^{+0.07}_{-0.07}$	0.18 $^{+0.01}_{-0.01}$	9.47 $^{+0.18}_{-0.14}$	0.02 $^{+0.0}_{-0.0}$	3.41 $^{+4.1}_{-2.73}$
low- α	-0.05	9.25	-11.73 $^{+22.65}_{-5.11}$	0.86 $^{+0.05}_{-0.05}$	0.18 $^{+0.01}_{-0.01}$	9.29 $^{+0.13}_{-0.16}$	0.02 $^{+0.0}_{-0.0}$	3.4 $^{+4.08}_{-2.72}$
low- α	-0.05	9.35	-3.02 $^{+0.63}_{-0.42}$	0.85 $^{+0.02}_{-0.02}$	0.21 $^{+0.0}_{-0.0}$	8.65 $^{+0.07}_{-0.06}$	0.02 $^{+0.0}_{-0.0}$	3.46 $^{+4.15}_{-2.77}$
low- α	-0.05	9.45	-4.27 $^{+1.03}_{-0.78}$	0.9 $^{+0.02}_{-0.02}$	0.22 $^{+0.0}_{-0.0}$	8.55 $^{+0.06}_{-0.08}$	0.02 $^{+0.0}_{-0.0}$	3.45 $^{+4.15}_{-2.76}$
low- α	-0.05	9.55	-15.74 $^{+35.17}_{-7.05}$	1.1 $^{+0.03}_{-0.03}$	0.25 $^{+0.0}_{-0.0}$	8.39 $^{+0.11}_{-0.09}$	0.02 $^{+0.0}_{-0.0}$	3.45 $^{+4.14}_{-2.76}$
low- α	-0.05	9.65	8.28 $^{+1.81}_{-2.84}$	1.11 $^{+0.04}_{-0.04}$	0.28 $^{+0.01}_{-0.0}$	8.65 $^{+0.12}_{-0.14}$	0.02 $^{+0.0}_{-0.0}$	3.39 $^{+4.07}_{-2.71}$
low- α	-0.05	9.75	5.49 $^{+0.75}_{-1.17}$	1.1 $^{+0.03}_{-0.03}$	0.31 $^{+0.01}_{-0.01}$	8.64 $^{+0.12}_{-0.15}$	0.03 $^{+0.0}_{-0.0}$	3.36 $^{+4.03}_{-2.69}$
low- α	-0.05	9.85	2.28 $^{+0.07}_{-0.09}$	1.08 $^{+0.05}_{-0.06}$	0.35 $^{+0.01}_{-0.0}$	9.83 $^{+0.18}_{-0.25}$	0.03 $^{+0.0}_{-0.0}$	3.27 $^{+3.92}_{-2.62}$
low- α	-0.05	9.95	2.1 $^{+0.12}_{-0.17}$	1.2 $^{+0.09}_{-0.1}$	0.37 $^{+0.01}_{-0.01}$	9.22 $^{+0.42}_{-0.78}$	0.03 $^{+0.0}_{-0.0}$	3.26 $^{+3.91}_{-2.61}$
low- α	-0.05	10.05	1.69 $^{+0.09}_{-0.1}$	0.31 $^{+0.08}_{-0.3}$	0.43 $^{+0.02}_{-0.02}$	11.81 $^{+0.25}_{-0.68}$	0.04 $^{+0.0}_{-0.0}$	3.21 $^{+3.85}_{-2.57}$
low- α	0.05	9.05	-4.64 $^{+5.7}_{-1.56}$	0.75 $^{+0.05}_{-0.05}$	0.16 $^{+0.01}_{-0.01}$	8.31 $^{+0.2}_{-0.18}$	0.01 $^{+0.0}_{-0.0}$	3.63 $^{+4.35}_{-2.9}$
low- α	0.05	9.15	-47.92 $^{+59.98}_{-40.36}$	0.81 $^{+0.07}_{-0.09}$	0.17 $^{+0.01}_{-0.01}$	8.59 $^{+0.21}_{-0.33}$	0.01 $^{+0.0}_{-0.0}$	3.55 $^{+4.26}_{-2.84}$
low- α	0.05	9.25	-30.98 $^{+53.42}_{-21.05}$	0.78 $^{+0.04}_{-0.04}$	0.18 $^{+0.01}_{-0.01}$	8.25 $^{+0.11}_{-0.14}$	0.01 $^{+0.0}_{-0.0}$	3.56 $^{+4.27}_{-2.85}$
low- α	0.05	9.35	-18.88 $^{+77.51}_{-9.19}$	0.69 $^{+0.02}_{-0.03}$	0.18 $^{+0.0}_{-0.0}$	8.48 $^{+0.07}_{-0.07}$	0.02 $^{+0.0}_{-0.0}$	3.55 $^{+4.25}_{-2.84}$
low- α	0.05	9.45	-18.73 $^{+38.81}_{-7.29}$	0.76 $^{+0.02}_{-0.02}$	0.21 $^{+0.0}_{-0.0}$	8.44 $^{+0.07}_{-0.07}$	0.02 $^{+0.0}_{-0.0}$	3.51 $^{+4.22}_{-2.81}$
low- α	0.05	9.55	5.1 $^{+0.77}_{-0.9}$	0.81 $^{+0.03}_{-0.03}$	0.22 $^{+0.0}_{-0.0}$	8.59 $^{+0.11}_{-0.11}$	0.02 $^{+0.0}_{-0.0}$	3.48 $^{+4.17}_{-2.78}$
low- α	0.05	9.65	3.16 $^{+0.3}_{-0.41}$	0.86 $^{+0.05}_{-0.04}$	0.25 $^{+0.0}_{-0.0}$	8.72 $^{+0.2}_{-0.18}$	0.02 $^{+0.0}_{-0.0}$	3.44 $^{+4.12}_{-2.75}$
low- α	0.05	9.75	2.84 $^{+0.16}_{-0.18}$	0.96 $^{+0.03}_{-0.03}$	0.29 $^{+0.01}_{-0.0}$	8.51 $^{+0.1}_{-0.12}$	0.02 $^{+0.0}_{-0.0}$	3.38 $^{+4.06}_{-2.71}$
low- α	0.05	9.85	1.96 $^{+0.06}_{-0.05}$	1.1 $^{+0.04}_{-0.04}$	0.31 $^{+0.01}_{-0.0}$	8.97 $^{+0.2}_{-0.18}$	0.02 $^{+0.0}_{-0.0}$	3.3 $^{+3.96}_{-2.64}$
low- α	0.05	9.95	1.97 $^{+0.12}_{-0.12}$	1.2 $^{+0.07}_{-0.07}$	0.36 $^{+0.01}_{-0.01}$	8.47 $^{+0.55}_{-0.53}$	0.03 $^{+0.0}_{-0.0}$	3.28 $^{+3.93}_{-2.62}$
low- α	0.05	10.05	1.8 $^{+0.32}_{-0.55}$	1.16 $^{+0.51}_{-0.1}$	0.36 $^{+0.02}_{-0.02}$	7.21 $^{+3.72}_{-0.75}$	0.03 $^{+0.0}_{-0.0}$	3.26 $^{+3.91}_{-2.61}$
low- α	0.05	10.15	6.54 $^{+4.55}_{-10.01}$	1.24 $^{+0.66}_{-0.21}$	0.31 $^{+0.03}_{-0.02}$	6.86 $^{+3.65}_{-1.16}$	0.02 $^{+0.01}_{-0.01}$	3.34 $^{+4.01}_{-2.67}$
low- α	0.15	9.05	2.16 $^{+0.25}_{-0.54}$	0.57 $^{+0.05}_{-0.08}$	0.14 $^{+0.01}_{-0.01}$	8.34 $^{+0.13}_{-0.34}$	0.01 $^{+0.0}_{-0.0}$	3.62 $^{+4.34}_{-2.9}$
low- α	0.15	9.15	2.51 $^{+0.35}_{-0.5}$	0.6 $^{+0.05}_{-0.06}$	0.15 $^{+0.01}_{-0.01}$	8.32 $^{+0.21}_{-0.19}$	0.01 $^{+0.0}_{-0.0}$	3.6 $^{+4.32}_{-2.88}$
low- α	0.15	9.25	10.73 $^{+5.05}_{-15510.04}$	0.81 $^{+0.06}_{-0.06}$	0.16 $^{+0.01}_{-0.01}$	7.36 $^{+0.3}_{-0.29}$	0.01 $^{+0.0}_{-0.0}$	3.51 $^{+4.21}_{-2.81}$
low- α	0.15	9.35	4.43 $^{+0.83}_{-1.25}$	0.68 $^{+0.03}_{-0.03}$	0.17 $^{+0.0}_{-0.01}$	7.99 $^{+0.13}_{-0.14}$	0.02 $^{+0.0}_{-0.0}$	3.55 $^{+4.26}_{-2.84}$
low- α	0.15	9.45	3.49 $^{+0.37}_{-0.42}$	0.71 $^{+0.03}_{-0.03}$	0.18 $^{+0.0}_{-0.0}$	8.15 $^{+0.11}_{-0.12}$	0.02 $^{+0.0}_{-0.0}$	3.54 $^{+4.25}_{-2.84}$
low- α	0.15	9.55	2.24 $^{+0.12}_{-0.15}$	0.71 $^{+0.03}_{-0.03}$	0.2 $^{+0.0}_{-0.0}$	8.4 $^{+0.1}_{-0.12}$	0.02 $^{+0.0}_{-0.0}$	3.49 $^{+4.18}_{-2.79}$
low- α	0.15	9.65	1.91 $^{+0.08}_{-0.08}$	0.8 $^{+0.03}_{-0.03}$	0.23 $^{+0.0}_{-0.0}$	8.34 $^{+0.11}_{-0.14}$	0.02 $^{+0.0}_{-0.0}$	3.45 $^{+4.14}_{-2.76}$
low- α	0.15	9.75	1.88 $^{+0.06}_{-0.08}$	0.87 $^{+0.03}_{-0.03}$	0.26 $^{+0.0}_{-0.0}$	8.64 $^{+0.11}_{-0.1}$	0.02 $^{+0.0}_{-0.0}$	3.38 $^{+4.05}_{-2.7}$
low- α	0.15	9.85	1.66 $^{+0.07}_{-0.04}$	1.08 $^{+0.04}_{-0.05}$	0.29 $^{+0.01}_{-0.0}$	8.48 $^{+0.24}_{-0.34}$	0.02 $^{+0.0}_{-0.0}$	3.3 $^{+3.96}_{-2.64}$

low- α	0.15	9.95	$1.85^{+0.09}_{-0.11}$	$1.05^{+0.05}_{-0.05}$	$0.32^{+0.01}_{-0.01}$	$8.08^{+0.3}_{-0.27}$	$0.02^{+0.0}_{-0.0}$	$3.3^{+3.96}_{-2.64}$
low- α	0.15	10.05	$1.72^{+0.22}_{-0.28}$	$1.08^{+0.18}_{-0.12}$	$0.34^{+0.01}_{-0.01}$	$7.81^{+1.72}_{-0.9}$	$0.03^{+0.0}_{-0.0}$	$3.28^{+3.94}_{-2.63}$
low- α	0.25	9.05	$2.24^{+0.36}_{-0.57}$	$0.57^{+0.03}_{-0.04}$	$0.13^{+0.01}_{-0.01}$	$6.34^{+0.18}_{-0.15}$	$0.01^{+0.0}_{-0.0}$	$3.34^{+4.0}_{-2.67}$
low- α	0.25	9.15	$2.08^{+0.35}_{-0.61}$	$0.66^{+0.04}_{-0.04}$	$0.13^{+0.01}_{-0.01}$	$6.29^{+0.24}_{-0.2}$	$0.01^{+0.0}_{-0.0}$	$3.41^{+4.09}_{-2.73}$
low- α	0.25	9.25	$3.1^{+0.55}_{-0.93}$	$0.72^{+0.05}_{-0.05}$	$0.16^{+0.01}_{-0.01}$	$6.91^{+0.31}_{-0.23}$	$0.01^{+0.0}_{-0.0}$	$3.38^{+4.05}_{-2.7}$
low- α	0.25	9.35	$3.11^{+0.49}_{-0.72}$	$0.76^{+0.03}_{-0.03}$	$0.16^{+0.01}_{-0.01}$	$6.49^{+0.18}_{-0.17}$	$0.01^{+0.0}_{-0.0}$	$3.35^{+4.02}_{-2.68}$
low- α	0.25	9.45	$2.72^{+0.28}_{-0.32}$	$0.73^{+0.03}_{-0.03}$	$0.15^{+0.01}_{-0.0}$	$6.75^{+0.13}_{-0.13}$	$0.01^{+0.0}_{-0.0}$	$3.38^{+4.06}_{-2.71}$
low- α	0.25	9.55	$1.71^{+0.08}_{-0.08}$	$0.6^{+0.03}_{-0.04}$	$0.17^{+0.0}_{-0.0}$	$8.06^{+0.12}_{-0.19}$	$0.01^{+0.0}_{-0.0}$	$3.48^{+4.18}_{-2.79}$
low- α	0.25	9.65	$1.47^{+0.05}_{-0.04}$	$0.69^{+0.03}_{-0.03}$	$0.2^{+0.0}_{-0.0}$	$8.04^{+0.14}_{-0.1}$	$0.01^{+0.0}_{-0.0}$	$3.43^{+4.11}_{-2.74}$
low- α	0.25	9.75	$1.56^{+0.05}_{-0.06}$	$0.76^{+0.05}_{-0.05}$	$0.23^{+0.0}_{-0.0}$	$8.48^{+0.28}_{-0.24}$	$0.01^{+0.0}_{-0.0}$	$3.36^{+4.03}_{-2.69}$
low- α	0.25	9.85	$1.54^{+0.03}_{-0.04}$	$0.99^{+0.03}_{-0.04}$	$0.26^{+0.01}_{-0.0}$	$7.92^{+0.18}_{-0.21}$	$0.01^{+0.0}_{-0.0}$	$3.3^{+3.95}_{-2.64}$
low- α	0.25	9.95	$1.82^{+0.08}_{-0.1}$	$1.1^{+0.04}_{-0.05}$	$0.3^{+0.01}_{-0.01}$	$7.57^{+0.26}_{-0.37}$	$0.01^{+0.0}_{-0.0}$	$3.28^{+3.93}_{-2.62}$
low- α	0.25	10.05	$1.67^{+0.18}_{-0.18}$	$0.95^{+0.1}_{-0.1}$	$0.31^{+0.02}_{-0.01}$	$7.65^{+0.6}_{-0.59}$	$0.02^{+0.0}_{-0.0}$	$3.28^{+3.94}_{-2.63}$
low- α	0.35	9.15	$1.84^{+0.36}_{-0.61}$	$0.8^{+0.08}_{-0.1}$	$0.16^{+0.01}_{-0.01}$	$6.34^{+0.4}_{-0.46}$	$0.01^{+0.0}_{-0.0}$	$3.36^{+4.03}_{-2.69}$
low- α	0.35	9.25	$2.09^{+0.26}_{-0.4}$	$0.66^{+0.11}_{-0.1}$	$0.16^{+0.01}_{-0.01}$	$7.13^{+0.48}_{-0.54}$	$0.0^{+0.0}_{-0.0}$	$3.34^{+4.01}_{-2.67}$
low- α	0.35	9.35	$1.63^{+0.16}_{-0.21}$	$0.63^{+0.1}_{-0.09}$	$0.15^{+0.01}_{-0.01}$	$7.7^{+0.48}_{-0.42}$	$0.01^{+0.0}_{-0.0}$	$3.39^{+4.07}_{-2.71}$
low- α	0.35	9.45	$1.56^{+0.09}_{-0.11}$	$0.55^{+0.09}_{-0.1}$	$0.15^{+0.01}_{-0.01}$	$7.77^{+0.38}_{-0.58}$	$0.0^{+0.0}_{-0.0}$	$3.35^{+4.02}_{-2.68}$
low- α	0.35	9.55	$1.39^{+0.04}_{-0.07}$	$0.6^{+0.06}_{-0.1}$	$0.16^{+0.01}_{-0.01}$	$8.39^{+0.21}_{-0.2}$	$0.0^{+0.0}_{-0.0}$	$3.33^{+4.0}_{-2.67}$
low- α	0.35	9.65	$1.31^{+0.03}_{-0.03}$	$0.58^{+0.06}_{-0.06}$	$0.18^{+0.0}_{-0.0}$	$8.6^{+0.2}_{-0.19}$	$0.0^{+0.0}_{-0.0}$	$3.3^{+3.96}_{-2.64}$
low- α	0.35	9.75	$1.34^{+0.04}_{-0.03}$	$0.72^{+0.06}_{-0.05}$	$0.21^{+0.01}_{-0.01}$	$8.25^{+0.26}_{-0.25}$	$0.0^{+0.0}_{-0.0}$	$3.3^{+3.96}_{-2.64}$
low- α	0.35	9.85	$1.41^{+0.05}_{-0.04}$	$0.91^{+0.07}_{-0.06}$	$0.26^{+0.01}_{-0.01}$	$8.24^{+0.58}_{-0.35}$	$0.01^{+0.0}_{-0.0}$	$3.27^{+3.92}_{-2.61}$
low- α	0.35	9.95	$1.64^{+0.08}_{-0.08}$	$0.91^{+0.09}_{-0.09}$	$0.29^{+0.01}_{-0.01}$	$8.47^{+0.45}_{-0.42}$	$0.01^{+0.0}_{-0.0}$	$3.29^{+3.95}_{-2.63}$
low- α	0.35	10.05	$1.38^{+0.17}_{-0.2}$	$0.8^{+0.29}_{-0.19}$	$0.27^{+0.03}_{-0.02}$	$7.92^{+3.67}_{-1.09}$	$0.01^{+0.01}_{-0.0}$	$3.28^{+3.93}_{-2.62}$
low- α	0.45	9.45	$1.05^{+0.06}_{-0.07}$	$0.37^{+0.14}_{-0.49}$	$0.2^{+0.02}_{-0.02}$	$9.58^{+3.89}_{-1.36}$	$0.0^{+0.0}_{-0.0}$	$3.05^{+3.66}_{-2.44}$
low- α	0.45	9.55	$0.93^{+0.03}_{-0.02}$	$0.57^{+0.3}_{-0.46}$	$0.19^{+0.01}_{-0.01}$	$10.78^{+0.86}_{-2.1}$	$0.0^{+0.0}_{-0.0}$	$2.93^{+3.51}_{-2.34}$
low- α	0.45	9.65	$0.92^{+0.02}_{-0.02}$	$0.38^{+0.14}_{-0.29}$	$0.19^{+0.01}_{-0.01}$	$9.65^{+5.25}_{-1.21}$	$0.0^{+0.0}_{-0.0}$	$3.0^{+3.6}_{-2.4}$
low- α	0.45	9.75	$0.98^{+0.02}_{-0.02}$	$0.76^{+0.17}_{-0.28}$	$0.19^{+0.01}_{-0.01}$	$8.97^{+2.08}_{-0.8}$	$0.0^{+0.0}_{-0.0}$	$3.06^{+3.67}_{-2.45}$
low- α	0.45	9.85	$1.06^{+0.03}_{-0.03}$	$0.42^{+0.17}_{-0.27}$	$0.22^{+0.01}_{-0.01}$	$10.01^{+2.75}_{-0.98}$	$0.0^{+0.0}_{-0.0}$	$3.11^{+3.73}_{-2.49}$
high- α	-0.95	9.95	$1.12^{+0.32}_{-0.35}$	$1.48^{+1.0}_{-0.18}$	$1.8^{+0.14}_{-0.14}$	$4.27^{+12.38}_{-2.12}$	$0.18^{+0.02}_{-0.03}$	$2.69^{+3.22}_{-2.15}$
high- α	-0.95	10.05	$3.39^{+0.59}_{-1.19}$	$1.07^{+0.1}_{-0.14}$	$1.49^{+0.11}_{-0.1}$	$8.13^{+0.3}_{-0.31}$	$0.14^{+0.03}_{-0.02}$	$2.95^{+3.54}_{-2.36}$
high- α	-0.95	10.15	$1.68^{+0.17}_{-0.21}$	$0.44^{+0.2}_{-0.55}$	$1.87^{+0.24}_{-0.19}$	$10.82^{+1.55}_{-1.99}$	$0.19^{+0.03}_{-0.03}$	$2.81^{+3.37}_{-2.24}$
high- α	-0.85	9.85	$1.33^{+0.09}_{-0.11}$	$0.99^{+0.58}_{-0.37}$	$1.16^{+0.15}_{-0.12}$	$10.59^{+1.18}_{-2.91}$	$0.09^{+0.02}_{-0.02}$	$2.75^{+3.31}_{-2.2}$
high- α	-0.85	9.95	$1.37^{+0.44}_{-0.05}$	$0.54^{+0.31}_{-0.95}$	$1.44^{+0.08}_{-0.07}$	$14.12^{+3.05}_{-10.51}$	$0.14^{+0.01}_{-0.01}$	$2.77^{+3.33}_{-2.22}$
high- α	-0.85	10.05	$2.44^{+0.2}_{-0.29}$	$0.8^{+0.15}_{-0.24}$	$1.18^{+0.06}_{-0.05}$	$9.17^{+0.44}_{-0.81}$	$0.1^{+0.01}_{-0.01}$	$2.97^{+3.56}_{-2.37}$
high- α	-0.85	10.15	$1.57^{+0.6}_{-0.13}$	$0.97^{+0.66}_{-0.76}$	$1.56^{+0.18}_{-0.14}$	$13.43^{+3.6}_{-10.3}$	$0.14^{+0.03}_{-0.03}$	$2.82^{+3.38}_{-2.25}$
high- α	-0.75	9.75	$1.36^{+0.08}_{-0.09}$	$1.45^{+0.34}_{-0.46}$	$1.13^{+0.12}_{-0.11}$	$10.13^{+1.32}_{-2.76}$	$0.1^{+0.02}_{-0.02}$	$2.8^{+3.36}_{-2.24}$
high- α	-0.75	9.85	$0.85^{+0.57}_{-0.65}$	$1.45^{+1.0}_{-0.14}$	$1.36^{+0.1}_{-0.1}$	$3.06^{+15.32}_{-2.18}$	$0.13^{+0.02}_{-0.02}$	$2.77^{+3.33}_{-2.22}$
high- α	-0.75	9.95	$1.87^{+0.17}_{-0.1}$	$1.23^{+0.08}_{-0.11}$	$1.18^{+0.05}_{-0.04}$	$8.27^{+0.33}_{-0.27}$	$0.09^{+0.01}_{-0.01}$	$2.91^{+3.49}_{-2.33}$
high- α	-0.75	10.05	$1.48^{+0.12}_{-0.07}$	$1.53^{+0.18}_{-0.1}$	$1.2^{+0.04}_{-0.04}$	$7.45^{+3.06}_{-1.38}$	$0.11^{+0.01}_{-0.01}$	$2.88^{+3.45}_{-2.3}$
high- α	-0.75	10.15	$1.35^{+0.56}_{-0.06}$	$0.47^{+0.23}_{-0.94}$	$1.29^{+0.09}_{-0.08}$	$12.56^{+3.48}_{-10.05}$	$0.12^{+0.01}_{-0.01}$	$2.86^{+3.43}_{-2.29}$
high- α	-0.65	9.55	$1.8^{+0.3}_{-0.39}$	$0.88^{+0.35}_{-0.45}$	$1.15^{+0.13}_{-0.13}$	$8.86^{+6.54}_{-1.2}$	$0.1^{+0.02}_{-0.03}$	$2.87^{+3.44}_{-2.3}$
high- α	-0.65	9.65	$1.67^{+0.12}_{-0.15}$	$1.03^{+0.41}_{-0.37}$	$1.12^{+0.1}_{-0.1}$	$10.46^{+1.16}_{-2.19}$	$0.11^{+0.02}_{-0.02}$	$2.87^{+3.45}_{-2.3}$
high- α	-0.65	9.75	$1.69^{+0.1}_{-0.14}$	$1.18^{+0.23}_{-0.18}$	$1.04^{+0.05}_{-0.06}$	$9.37^{+1.52}_{-0.94}$	$0.09^{+0.01}_{-0.01}$	$2.9^{+3.48}_{-2.32}$
high- α	-0.65	9.85	$1.72^{+0.1}_{-0.11}$	$1.18^{+0.12}_{-0.11}$	$1.1^{+0.05}_{-0.05}$	$8.49^{+0.69}_{-0.62}$	$0.1^{+0.01}_{-0.01}$	$2.93^{+3.51}_{-2.34}$
high- α	-0.65	9.95	$2.16^{+0.1}_{-0.12}$	$1.14^{+0.04}_{-0.06}$	$1.09^{+0.03}_{-0.03}$	$7.94^{+0.13}_{-0.19}$	$0.09^{+0.01}_{-0.01}$	$2.98^{+3.58}_{-2.39}$
high- α	-0.65	10.05	$1.16^{+0.03}_{-0.04}$	$1.52^{+0.05}_{-0.06}$	$1.22^{+0.04}_{-0.03}$	$6.3^{+0.54}_{-0.24}$	$0.12^{+0.01}_{-0.0}$	$2.84^{+3.41}_{-2.27}$
high- α	-0.65	10.15	$1.44^{+0.06}_{-0.06}$	$0.4^{+0.15}_{-0.98}$	$1.22^{+0.07}_{-0.06}$	$12.24^{+1.09}_{-1.62}$	$0.11^{+0.01}_{-0.01}$	$2.89^{+3.46}_{-2.31}$
high- α	-0.55	9.55	$1.84^{+0.32}_{-0.71}$	$1.14^{+0.71}_{-0.27}$	$0.96^{+0.09}_{-0.07}$	$8.17^{+9.26}_{-4.45}$	$0.1^{+0.01}_{-0.02}$	$2.97^{+3.56}_{-2.37}$
high- α	-0.55	9.65	$1.72^{+0.16}_{-0.25}$	$1.09^{+0.28}_{-0.26}$	$1.11^{+0.1}_{-0.09}$	$9.6^{+1.18}_{-2.13}$	$0.11^{+0.02}_{-0.02}$	$2.9^{+3.48}_{-2.32}$
high- α	-0.55	9.75	$1.65^{+0.15}_{-0.27}$	$1.11^{+0.68}_{-0.23}$	$0.98^{+0.06}_{-0.06}$	$8.64^{+6.99}_{-1.08}$	$0.1^{+0.01}_{-0.01}$	$2.96^{+3.55}_{-2.36}$

high- α	-0.55	9.85	$2.02^{+0.18}_{-0.22}$	$1.16^{+0.08}_{-0.12}$	$0.94^{+0.05}_{-0.04}$	$7.91^{+0.43}_{-0.38}$	$0.08^{+0.01}_{-0.01}$	$3.0^{+3.6}_{-2.4}$
high- α	-0.55	9.95	$2.46^{+0.11}_{-0.11}$	$1.07^{+0.03}_{-0.03}$	$0.97^{+0.02}_{-0.02}$	$7.9^{+0.09}_{-0.09}$	$0.08^{+0.0}_{-0.0}$	$3.03^{+3.64}_{-2.43}$
high- α	-0.55	10.05	$1.35^{+0.02}_{-0.02}$	$1.17^{+0.25}_{-0.24}$	$1.05^{+0.02}_{-0.03}$	$11.34^{+0.55}_{-2.48}$	$0.09^{+0.0}_{-0.0}$	$2.88^{+3.46}_{-2.31}$
high- α	-0.55	10.15	$1.54^{+0.06}_{-0.07}$	$0.92^{+0.35}_{-0.29}$	$1.07^{+0.05}_{-0.04}$	$10.02^{+1.62}_{-2.02}$	$0.1^{+0.01}_{-0.01}$	$2.95^{+3.54}_{-2.36}$
high- α	-0.45	9.55	$1.64^{+0.16}_{-0.24}$	$0.98^{+0.25}_{-0.26}$	$0.72^{+0.07}_{-0.05}$	$9.1^{+1.13}_{-1.41}$	$0.06^{+0.01}_{-0.01}$	$3.02^{+3.62}_{-2.41}$
high- α	-0.45	9.65	$2.22^{+0.51}_{-0.76}$	$1.18^{+0.27}_{-0.24}$	$0.83^{+0.08}_{-0.07}$	$8.12^{+7.18}_{-1.04}$	$0.07^{+0.02}_{-0.02}$	$3.03^{+3.64}_{-2.43}$
high- α	-0.45	9.75	$2.03^{+0.25}_{-0.3}$	$1.1^{+0.13}_{-0.13}$	$0.9^{+0.06}_{-0.05}$	$8.1^{+0.6}_{-0.53}$	$0.08^{+0.01}_{-0.01}$	$3.02^{+3.63}_{-2.42}$
high- α	-0.45	9.85	$2.46^{+0.22}_{-0.29}$	$1.13^{+0.07}_{-0.08}$	$0.76^{+0.03}_{-0.03}$	$7.84^{+0.29}_{-0.24}$	$0.05^{+0.01}_{-0.01}$	$3.07^{+3.69}_{-2.46}$
high- α	-0.45	9.95	$2.58^{+0.11}_{-0.15}$	$1.03^{+0.02}_{-0.03}$	$0.86^{+0.02}_{-0.01}$	$7.79^{+0.08}_{-0.09}$	$0.07^{+0.0}_{-0.0}$	$3.07^{+3.68}_{-2.45}$
high- α	-0.45	10.05	$1.35^{+0.02}_{-0.02}$	$1.3^{+0.11}_{-0.07}$	$0.89^{+0.02}_{-0.02}$	$9.33^{+2.23}_{-2.06}$	$0.08^{+0.0}_{-0.0}$	$2.94^{+3.53}_{-2.35}$
high- α	-0.45	10.15	$1.77^{+0.17}_{-0.09}$	$1.18^{+0.07}_{-0.06}$	$0.91^{+0.04}_{-0.03}$	$7.61^{+0.3}_{-0.36}$	$0.08^{+0.01}_{-0.01}$	$3.01^{+3.61}_{-2.41}$
high- α	-0.35	9.55	$1.57^{+0.16}_{-0.24}$	$0.39^{+0.14}_{-0.59}$	$0.74^{+0.08}_{-0.06}$	$10.32^{+0.86}_{-1.77}$	$0.07^{+0.01}_{-0.01}$	$3.01^{+3.62}_{-2.41}$
high- α	-0.35	9.65	$2.15^{+0.38}_{-0.4}$	$0.95^{+0.19}_{-0.33}$	$0.69^{+0.07}_{-0.05}$	$8.71^{+0.97}_{-0.88}$	$0.05^{+0.01}_{-0.01}$	$3.08^{+3.69}_{-2.46}$
high- α	-0.35	9.75	$2.36^{+0.48}_{-0.61}$	$1.16^{+0.15}_{-0.11}$	$0.71^{+0.05}_{-0.04}$	$7.39^{+1.03}_{-0.47}$	$0.06^{+0.01}_{-0.01}$	$3.07^{+3.69}_{-2.46}$
high- α	-0.35	9.85	$2.1^{+0.15}_{-0.16}$	$1.14^{+0.08}_{-0.09}$	$0.67^{+0.03}_{-0.02}$	$8.13^{+0.33}_{-0.44}$	$0.05^{+0.01}_{-0.01}$	$3.11^{+3.73}_{-2.48}$
high- α	-0.35	9.95	$2.31^{+0.09}_{-0.1}$	$0.97^{+0.03}_{-0.03}$	$0.72^{+0.01}_{-0.01}$	$7.76^{+0.07}_{-0.08}$	$0.06^{+0.0}_{-0.0}$	$3.1^{+3.72}_{-2.48}$
high- α	-0.35	10.05	$1.35^{+0.03}_{-0.03}$	$1.24^{+0.04}_{-0.04}$	$0.75^{+0.02}_{-0.02}$	$7.71^{+0.95}_{-0.62}$	$0.06^{+0.0}_{-0.0}$	$2.99^{+3.59}_{-2.39}$
high- α	-0.35	10.15	$2.08^{+0.15}_{-0.21}$	$1.1^{+0.06}_{-0.07}$	$0.79^{+0.03}_{-0.03}$	$7.46^{+0.27}_{-0.36}$	$0.07^{+0.01}_{-0.01}$	$3.06^{+3.68}_{-2.45}$
high- α	-0.25	9.55	$1.79^{+0.35}_{-0.6}$	$1.02^{+0.58}_{-0.22}$	$0.58^{+0.06}_{-0.04}$	$7.64^{+8.86}_{-0.92}$	$0.05^{+0.01}_{-0.01}$	$3.1^{+3.72}_{-2.48}$
high- α	-0.25	9.65	$2.07^{+0.29}_{-0.46}$	$0.94^{+0.24}_{-0.18}$	$0.61^{+0.05}_{-0.04}$	$8.22^{+1.36}_{-0.73}$	$0.04^{+0.01}_{-0.01}$	$3.12^{+3.75}_{-2.5}$
high- α	-0.25	9.75	$1.71^{+0.15}_{-0.2}$	$0.72^{+0.43}_{-0.47}$	$0.63^{+0.05}_{-0.04}$	$10.61^{+1.04}_{-2.7}$	$0.05^{+0.01}_{-0.01}$	$3.07^{+3.68}_{-2.45}$
high- α	-0.25	9.85	$1.76^{+0.09}_{-0.13}$	$1.06^{+0.06}_{-0.07}$	$0.59^{+0.02}_{-0.02}$	$7.82^{+0.22}_{-0.24}$	$0.05^{+0.0}_{-0.0}$	$3.11^{+3.74}_{-2.49}$
high- α	-0.25	9.95	$2.06^{+0.09}_{-0.07}$	$1.0^{+0.02}_{-0.03}$	$0.6^{+0.01}_{-0.01}$	$7.76^{+0.1}_{-0.1}$	$0.05^{+0.0}_{-0.0}$	$3.14^{+3.77}_{-2.51}$
high- α	-0.25	10.05	$1.55^{+0.06}_{-0.04}$	$1.03^{+0.04}_{-0.06}$	$0.58^{+0.02}_{-0.01}$	$7.98^{+0.19}_{-0.22}$	$0.04^{+0.0}_{-0.0}$	$3.09^{+3.71}_{-2.47}$
high- α	-0.25	10.15	$1.6^{+0.14}_{-0.16}$	$1.05^{+0.21}_{-0.1}$	$0.69^{+0.04}_{-0.03}$	$7.98^{+2.15}_{-0.54}$	$0.07^{+0.01}_{-0.0}$	$3.09^{+3.7}_{-2.47}$
high- α	-0.15	9.65	$1.64^{+0.3}_{-0.54}$	$0.92^{+0.58}_{-0.3}$	$0.46^{+0.04}_{-0.04}$	$8.07^{+5.07}_{-2.04}$	$0.04^{+0.01}_{-0.01}$	$3.19^{+3.82}_{-2.55}$
high- α	-0.15	9.75	$1.6^{+0.17}_{-0.24}$	$0.99^{+0.53}_{-0.18}$	$0.5^{+0.03}_{-0.02}$	$8.62^{+4.93}_{-0.97}$	$0.04^{+0.01}_{-0.01}$	$3.14^{+3.77}_{-2.51}$
high- α	-0.15	9.85	$1.66^{+0.1}_{-0.09}$	$1.03^{+0.06}_{-0.06}$	$0.49^{+0.01}_{-0.01}$	$7.94^{+0.32}_{-0.27}$	$0.04^{+0.0}_{-0.0}$	$3.15^{+3.79}_{-2.52}$
high- α	-0.15	9.95	$2.09^{+0.09}_{-0.1}$	$0.9^{+0.03}_{-0.03}$	$0.5^{+0.01}_{-0.01}$	$7.95^{+0.12}_{-0.09}$	$0.04^{+0.0}_{-0.0}$	$3.2^{+3.84}_{-2.56}$
high- α	-0.15	10.05	$1.77^{+0.06}_{-0.08}$	$0.98^{+0.04}_{-0.05}$	$0.52^{+0.01}_{-0.01}$	$8.11^{+0.18}_{-0.16}$	$0.04^{+0.0}_{-0.0}$	$3.17^{+3.81}_{-2.54}$
high- α	-0.15	10.15	$1.47^{+0.11}_{-0.12}$	$0.65^{+0.37}_{-0.44}$	$0.62^{+0.04}_{-0.04}$	$10.66^{+1.8}_{-2.54}$	$0.06^{+0.01}_{-0.01}$	$3.09^{+3.7}_{-2.47}$
high- α	-0.05	9.65	$1.49^{+0.79}_{-0.32}$	$1.32^{+0.27}_{-0.14}$	$0.5^{+0.04}_{-0.04}$	$6.47^{+2.7}_{-5.87}$	$0.04^{+0.01}_{-0.01}$	$3.08^{+3.69}_{-2.46}$
high- α	-0.05	9.75	$1.28^{+0.78}_{-0.21}$	$1.27^{+0.23}_{-0.06}$	$0.37^{+0.03}_{-0.02}$	$2.48^{+6.42}_{-2.16}$	$0.02^{+0.0}_{-0.0}$	$3.13^{+3.75}_{-2.5}$
high- α	-0.05	9.85	$1.59^{+0.08}_{-0.09}$	$1.1^{+0.06}_{-0.06}$	$0.42^{+0.02}_{-0.01}$	$7.48^{+0.39}_{-0.4}$	$0.03^{+0.0}_{-0.0}$	$3.16^{+3.8}_{-2.53}$
high- α	-0.05	9.95	$2.71^{+0.21}_{-0.23}$	$0.88^{+0.04}_{-0.04}$	$0.44^{+0.01}_{-0.01}$	$7.9^{+0.14}_{-0.12}$	$0.03^{+0.0}_{-0.0}$	$3.26^{+3.91}_{-2.61}$
high- α	-0.05	10.05	$2.27^{+0.18}_{-0.25}$	$0.9^{+0.05}_{-0.06}$	$0.49^{+0.02}_{-0.01}$	$7.82^{+0.19}_{-0.21}$	$0.04^{+0.0}_{-0.0}$	$3.21^{+3.85}_{-2.57}$
high- α	0.05	9.75	$1.29^{+0.81}_{-0.19}$	$1.2^{+0.27}_{-0.09}$	$0.39^{+0.02}_{-0.02}$	$4.4^{+5.03}_{-4.09}$	$0.03^{+0.0}_{-0.0}$	$3.11^{+3.73}_{-2.49}$
high- α	0.05	9.85	$1.68^{+0.11}_{-0.1}$	$0.93^{+0.07}_{-0.06}$	$0.38^{+0.02}_{-0.01}$	$7.89^{+0.27}_{-0.28}$	$0.02^{+0.0}_{-0.0}$	$3.2^{+3.85}_{-2.56}$
high- α	0.05	9.95	$2.73^{+0.23}_{-0.31}$	$0.81^{+0.04}_{-0.05}$	$0.4^{+0.01}_{-0.01}$	$8.05^{+0.12}_{-0.14}$	$0.03^{+0.0}_{-0.0}$	$3.31^{+3.97}_{-2.65}$
high- α	0.05	10.05	$2.76^{+0.61}_{-1.25}$	$0.97^{+0.09}_{-0.08}$	$0.42^{+0.02}_{-0.02}$	$6.95^{+0.66}_{-0.49}$	$0.03^{+0.01}_{-0.01}$	$3.22^{+3.86}_{-2.57}$
high- α	0.15	9.75	$1.83^{+0.21}_{-0.35}$	$0.73^{+0.14}_{-0.17}$	$0.36^{+0.03}_{-0.03}$	$8.41^{+0.57}_{-0.46}$	$0.02^{+0.01}_{-0.01}$	$3.26^{+3.91}_{-2.61}$
high- α	0.15	9.85	$1.94^{+0.15}_{-0.19}$	$0.8^{+0.07}_{-0.08}$	$0.35^{+0.02}_{-0.01}$	$8.17^{+0.23}_{-0.23}$	$0.02^{+0.0}_{-0.0}$	$3.29^{+3.94}_{-2.63}$
high- α	0.15	9.95	$3.32^{+0.63}_{-0.87}$	$0.81^{+0.06}_{-0.07}$	$0.4^{+0.02}_{-0.02}$	$7.79^{+0.21}_{-0.18}$	$0.03^{+0.01}_{-0.01}$	$3.29^{+3.95}_{-2.63}$
high- α	0.15	10.05	$3.53^{+0.78}_{-1.31}$	$0.74^{+0.12}_{-0.11}$	$0.36^{+0.03}_{-0.02}$	$8.18^{+0.41}_{-0.37}$	$0.01^{+0.01}_{-0.01}$	$3.35^{+4.02}_{-2.68}$
high- α	0.25	9.85	$1.88^{+0.3}_{-0.89}$	$0.44^{+0.18}_{-0.41}$	$0.34^{+0.03}_{-0.03}$	$8.99^{+0.47}_{-1.71}$	$0.02^{+0.01}_{-0.01}$	$3.29^{+3.95}_{-2.64}$
high- α	0.25	9.95	$4.66^{+2.54}_{-12.41}$	$0.84^{+0.09}_{-0.15}$	$0.35^{+0.03}_{-0.03}$	$6.82^{+0.34}_{-0.74}$	$0.04^{+0.01}_{-0.01}$	$3.29^{+3.94}_{-2.63}$